Wireless Resonant Magnetic MicroActuators

A THESIS
SUBMITTED TO THE FACULTY OF THE GRADUATE SCHOOL
OF THE UNIVERSITY OF MINNESOTA
BY

Karl Eric Vollmers

IN PARTIAL FULFILLMENT OF THE REQUIREMENTS
FOR THE DEGREE OF
DOCTOR OF PHILOSOPHY

Bradley J Nelson, Adviser

November, 2008

Dedication

This thesis is dedicated to my wife and family who have taught me so many important things in life.

Acknowledgments

A long list of people have contributed to this work. First and foremost I would like to acknowledge the support and encouragement of Professor Bradley J. Nelson and thank him for the opportunity work in the world of microfabrication and MEMS. I am grateful for the chance to have lived and worked in Switzerland and for all the things I have learned and experienced when there. I would like to extend special thanks to two great friends, teammates, and colleagues, Bradley Kratochvil and Dominic Frutiger. They deserve special mention for many reasons, including their part in the Magmite project, their wit and conversation, their friendship and perhaps most importantly, their belief that I would eventually finish this. Thanks go out to the current and former members of the IRIS group. Thanks for the great experience, the grilling, the friendships and all the help and support. Special thanks to Felix, Jake, Li, Ruedi and Simon for their individual contributions and support. I would like to thank the CLA cleanroom team and users for making it possible to make the devices. Also, the NFC team at the University of Minnesota for teaching me all about microfabrication. Craig McGray and NIST deserve special mention for the well timed Nanogram debut, which provided a wonderful platform to leverage the project. Perhaps most importantly, my eternal gratitude to my wife, Megan Cassidy, for believing in me and supporting me through it all.

Abstract

Rapid advances in miniaturization and robotics are presenting new opportunities for collaboration between the fields of robotics and medicine. Since their development in the late 1990s, minimally invasive robotic systems have become an accepted partner in the surgical suite. This trend has continued with the development of noninvasive camera pills for GI tract inspection. Further miniaturization and development of noninvasive microrobotic platforms and procedures will occur in the near future. This thesis contributes to the development of viable medical microrobots with the presentation of new wireless micromotors capable of providing power and propulsion to sub-millimeter wireless robotic platforms. The wireless resonant actuator can be individually actuated by frequency-dependent power, which is delivered by oscillating external magnetic fields. By relying on magnetic forces between neighboring soft magnetic bodies, a high-power, individually addressable, scalable wireless microactuator was created. Utilizing the energy amplification of impact, impact forces as high as 300 μN have been demonstrated. The actuator is used to provide power, propulsion and control to a 300×300×70 μm^3 microrobotic platform that can be driven with a full three degrees of freedom and can manipulate objects on a flat substrate in both air and liquid environments. An undergraduate student team using the microrobotic platform won the 2007 RoboCup Nanogram competition with velocities of over 1.25 cm/s (greater than 40 body lengths/s) and autonomous manipulation of microobjects.

Contents

List of Tables

List of Figures

1 Introduction

Science fiction writers have always fantasized about shrinking modern mechanical marvels to a size that could travel through our bodies. By making machines small enough, they could use the cardiovascular system as miniature highways to wipe out disease, repair cells or give us superhuman powers. Portrayed as submarines with a human cargo shrunken by exotic forms of energy or as miniature nanobots bent on our assimilation, they have captured our imagination for generations. Unfortunately (depending on your point of view), this is where they have been forced to remain, limited by the technological hurdles of reality.

While autonomous microrobots traveling through the body are still the work of science fiction, large robotic systems have arrived on the medical scene and are an accepted part of many surgical suites. They are commonly used in minimally invasive procedures that reduce patient discomfort and recovery time by reducing surgically induced trauma. Robotic systems are being used to simplify difficult procedures and enable completely new procedures that were previously impossible. Smaller systems such as Given Imaging's PillCam have given doctors new tools to peer inside the body. Using camera pills, parts of the body that were previously only accessible through major surgery can now be viewed on a monitor in a doctor's office. While the PillCam is quite small, it is still over 1 cm in diameter and nearly 3 cm long. The development of even smaller systems will undoubtedly enable more minimally invasive and non invasive procedures. As sure as they have captured our imaginations, wireless microrobots have the potential to revolutionize many aspects of medicine. Small devices will use natural ducts and cavities in the body to enable new procedures. The urinary tract, the cardiovascular system, the cerebrospinal fluid system in the brain and spine, and the vitreous humor in the eye are all possible pathways for microrobots to perform procedures, deliver drugs and monitor patient health. Unfortunately, these developments will not be as easy as simply injecting a small robot into the body. Microsystems are hampered by technological hurdles. Devices this small require new technology for sensing, localization, propulsion and actuation. Propulsion and actuation are the more challenging of these requirements and are the subject of this research.

Magnetics are the most popular method of producing forces over a distance and have a long history of being used to guide and manipulate objects in the body [20]. Magnetic propulsion of small robotic platforms is the subject of research in several groups [1,34,45]. Others are working on the development of wireless sensors suitable for deployment on such platforms [17]. While headway is being made on propulsion and sensing, there are no suitable power sources or actuators available to drive pumps, valves or other mechanical systems on wireless untethered microrobots. Few practical actuators exist at these scales that can generate sufficient force to perform useful tasks, and almost none of them can be operated in a wireless manner on sub-mm platforms. Many aspects of the problem must be addressed when considering solutions. Energy storage does not scale well and must be considered a primary design criterion [11]. Selective control of individual actuators, and force output must also be considered. Traditional methods of wireless communication or power transmission methods typically involve inductive coupling between antennas. Unfortunately, the efficiency of this method depends on the area of the coils, making it a less attractive method for transmitting power to sub-mm robots. In addition, such systems require circuitry and electronics that lead to further power consumption, increased complexity and space requirements.

One method of bypassing these problems is to transmit the energy directly to a mechanical structure that then transforms the energy to a useful form. Several researchers have published papers describing microrobots and actuators that are powered by vibrations [44,52]. Others have documented the use of externally applied electrical fields [8,14]. Still others have reported on the remote control and propulsion of microrobots with magnetic fields [2,36,37,45,53]. Unfortunately, the typical methods of propulsion using magnetic field gradients does not easily facilitate the development of individually controllable robots or actuators that can be powered by the same field. It was this lack of suitable wireless microactuators that motivated the research presented here. By combining the resonant response of the vibration-driven actuators with the ability of magnetic fields to remotely create strong localized interbody forces, a new class of actuators was developed. These actuators offer narrow frequency responses that enable individual control. In addition, they provide high forces through the use of impact and they can be operated without wires or teth-

ers. Figure 1 shows the "Magmite" microrobot that resulted from this research. It is powered by the integrated wireless resonant magnetic microactuator (WRMMA). The microrobot is pictured with a common fruit fly and measures less than 300×300 μm^2 and can move with velocities of over 1.25 cm/s.

This dissertation investigates propulsion and actuation technologies for microrobotic systems and presents a new class of actuators. Chapter 2 reviews the state-of-the-art propulsion and actuation methods. Chapter 3 presents a review of magnetics and investigates the interbody magnetic forces that power the new class of resonant magnetic microactuators. Chapter 4 describes the theory and operation of the actuators themselves and details their application in the Magmite platform. Chapter 5 discusses the fabrication of the Magmite microrobot and of the integration of permanent micromagnets in microfabricated systems. Chapter 6 presents the Magmite experimental setup and discusses experimental results. Conclusions and summary are given in Chapter 7 with additional details presented in the Appendices.

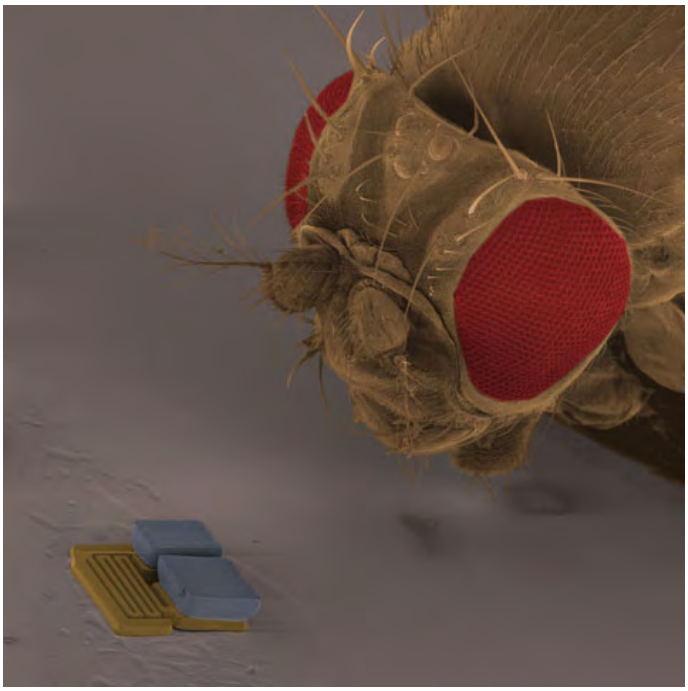

Figure 1: Colored scanning electron microscope image of Magmite microrobot (size 300×300×70 μm^3) containing the wireless resonant magnetic microactuator with a fruit fly for scale (image courtesy of Bradley Kratochvil).

2 Overview: Wireless Microactuation and Microrobots

Sub-millimeter microrobotic systems with critical dimensions in the μm range are an area of increasing interest and research with many possible applications, including medicine, exploration, sensor networks and micromanipulation. Although these applications may widely differ, they share many similarities, such as the need for miniaturized power supplies, efficient propulsion methods and miniaturized sensors and actuators [13]. Power-storage devices compatible with the size and weight of microfabricated robots are limited [11]. Chemical-energy storage systems such as batteries depend on the volume of electrolytic components and large internal surface areas to produce the long-lasting macro batteries we use daily. As these components are shrunk to the microscale, the total energy stored is dramatically reduced. Power-transmission methods such as inductive coupling also scale poorly as they depend on the cross-sectional area of the receiving antenna.

The issue of power is so limiting in sub-mm^2 devices that successful microrobots can not be designed without first solving the energy problem. With the exception of efforts to harness local sources of biological power like adenosine triphosphate (ATP) or glucose [38], most research efforts have relied on the delivery of power from external sources. These means usually include vibration, electrostatics, photons and magnetics. Each has different advantages and disadvantages, which are briefly discussed in the following sections in terms of their suitability for microrobotic actuators.

2.1 Vibrations

The use of vibrational or oscillatory motion to power, drive or regulate motors has a long history stretching back to the development of clocks in the 14th century. A. Pisano offers an insightful and historical review, examining their development and suitability for micromotors in his 1989 paper [42]. Vibration-driven microactuators commonly consist of resonating bodies excited by vibrations that are broadcast through the environment. Typically these vibrations are generated at select frequencies by piezo actuators hooked to the substrate on which the actuator rests or is

mounted. Because vibrational actuators rely on the natural resonant frequencies of mechanical systems, these systems can often be modeled as simple spring-mass oscillating systems as taught in introductory physics and engineering classes.

$$F(t) = kx + c\dot{x} + m\ddot{x} \tag{1}$$

where k, c and m are the spring constant, damping and mass, and $F(t)$ is the excitation signal. Resonant actuators typically take advantage of the the ability of the system to absorb large amounts of energy from the driving signal when the signal closely matches the natural resonant frequency ω_n, which is given as

$$\omega_n = \sqrt{\frac{k}{m}} \tag{2}$$

By designing two or more actuators with different resonant frequencies, they can be independently powered and controlled by one signal with multiple frequency components.

In addition to a resonating body, the design of a successful resonant actuator must also include a mechanical rectifier capable of rectifying the vibratory motion into either linear or rotary motion [7]. This is of primary importance and often the limiting factor to successful resonant actuators. Several examples have been presented at conferences or in academic journals and are discussed in the following sections.

The robot platform described by Yasuda et al. is shown in Figure 2 [52]. In this example, a microfabricated robot resting on the substrate is powered by vibrations in the substrate that excite two kicking legs with unique excitation frequencies.

The robot body was constructed of polysilicon with flexible polyimide joints and springs and measured 0.7 by 1.5 mm. Flexible joints in the support legs lifted the body off the substrate. Resonating masses on the kicking legs supported by springs of different length formed the resonant actuators that drove the robot forward. By adjusting the driving frequency up and down the robot can turn left or right, advance, or stop depending on the driving frequency. The authors report that changes in humidity had large effects on robot driving performance. High humidity wet the substrate and the resulting surface tension made it difficult for the robot to move.

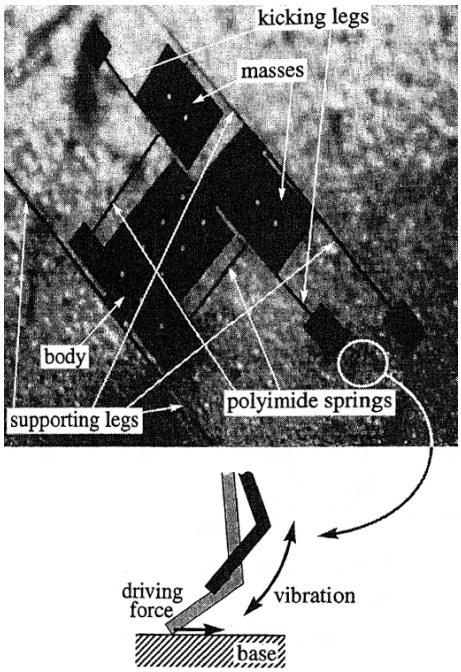

Figure 2: Vibrationally driven walking robot [52].

Low humidity caused static charging in the device and substrate, causing subsequent clamping, which also hindered motion. The authors report that the robot velocity was nearly identical on conductive surfaces such as aluminum and highly doped silicon surfaces, but greatly reduced on undoped semiconducting silicon with no motion in insulating silicon nitride surfaces where static charges can accumulate.

Another example of a wireless resonant actuator is given by Saitou et al [44]. The authors present a driving mechanism for a linear microvibromotor that relies on vibrational energy transferred through the substrate. The power transmission method was applied to a system similar to that reported by Daneman et al., where electrostatic actuators were used [12]. Pai and Tien also present a similar system driven by thermal actuators [40]. In the work by Saitou et al., shown in Figure 3 [44], two matching sets of impact actuators were designed with different resonant frequencies, enabling the linear actuator to be driven forward or backward as desired.

The vibrational energy was delivered with a piezoelectric actuator mounted to the substrate. The impact actuators transmitted their mechanical energy to the

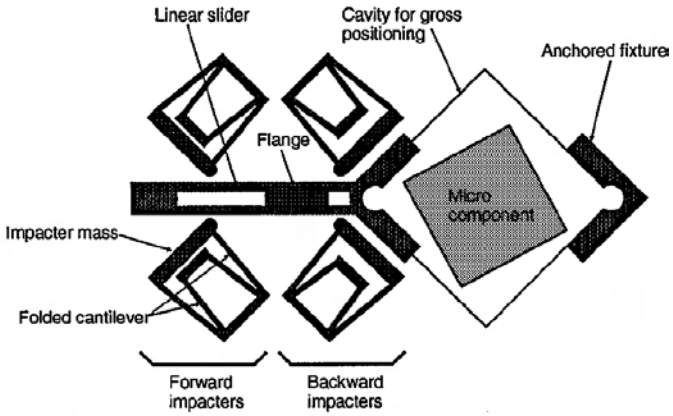

Figure 3: Resonant impact motor- driven linear vibromotor. Matching impactor pairs with different resonant frequencies are excited with substrate vibrations and used to drive a linear slider forward or backward depending on which pair of impactors are excited [44].

linear slider through simultaneous impact on both sides of the slider. The authors report that the slider could be driven forward and backward at will, but their efforts to position and clamp microparts in a jig-like structure were complicated by the vibration-induced motion of the micropart across the surface and out of the jig.

Theoretically, the use of vibrational broadcast energy could be applied to remote powering of wireless actuators where vibrational energy can be passed through a 3-D environment to power the actuators immersed in the environment. It is conceivable that this could be extended to ultrasound or lower frequency sound waves, which could be used to drive actuators on microrobots in medical applications, but no published results or investigations on this concept could be found.

2.2 Electrostatics

Electrostatic fields are a popular source of force generation for microactuators. Unfortunately, they typically require high voltages over narrow gaps between capacitor plates. Typical parameter ranges are voltages from 20 to 200 V with gaps from 1 to 10 μm and forces from nN to μN. Due to the the requirements of charging capacitive plates to high voltages, electrostatics are not often thought of as suitable candidates for wireless actuation. Those that do exist can be divided into two general approaches.

The first method relies on the use of externally generated electrical fields; the second uses transmitted energy to power logic circuits and traditional electrostatic motors on a wireless device.

2.2.1 Scratch Drive Actuators

The first example demonstrating the use of external fields for wireless actuation is a Scratch Drive Actuator (SDA) system as presented by Donald et al. [14], which is an adaption from the original SDA actuator reported by Akiyama and Shono [3]. The original SDA is powered by electrostatic attraction between a charged L-shaped deformable conductive polysilicon plate and a grounded substrate and is illustrated in Figure 4 (a) [14]. The application of a voltage potential between the upper body and the insulated substrate creates attractive forces between the two that cause the upper body to deflect and flatten against the substrate. This causes a rotation of the front leg that advances the lower edge. Reduction of the voltage allows the body to relax and causes the front leg to return to a vertical orientation and pull the body forward. Rapid repetition of the process causes the device to crawl across the substrate. Donald et al. developed a method of powering the SDA by embedding interdigitated electrodes in the substrate that induce charge separation in the conductive body of the SDA, as shown in Figure 4 (b). This remote powering method, along with the development of stress-curved cantilever arms that can be clamped to the substrate with a constant voltage offset in the driving signal, allow the device to be driven forward or to turn in one direction. Linderman et al. present a method for optimizing the design of SDAs based on the original power delivery method [30]. The group also made force measurements with spring-tethered devices and found that they could generate approximately 20 μN of force per single SDA device with a 1 kHz 200 V signal. Arrays of nearly 200 devices (1.4×1.4 mm) were able to push 2×2×0.5 mm chips across the substrate [30].

2.2.2 Diode-Based Micropumps

A recent example using external electrostatic fields is given by Chang et al. and is shown in Figure 5 [8]. The authors report on the use of diodes to pump fluids across

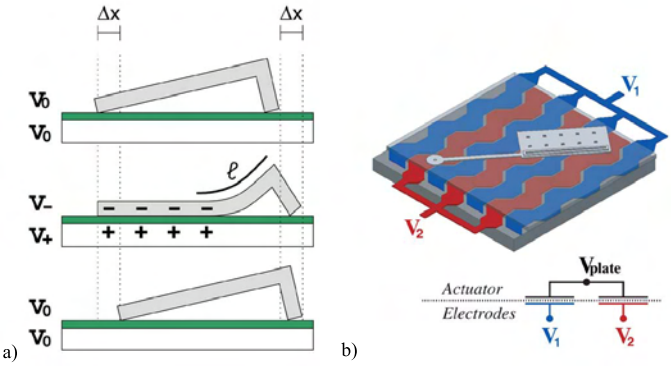

Figure 4: a) Charge separation in the microrobot body creates attractive forces that inform the plate body, pushing the front lip forward a short distance each cycle. b) A DC offset in conjunction with the AC signal holds the pivot arm against the surface, causing the robot to rotate around it [14].

their surfaces when exposed to external fields. They present examples of floating diodes that are propelled across the surface of a beaker of water when voltage signals of 10 Hz to 37 kHz generating field strengths of 30 to 150 V/cm are applied. The application of an external AC field causes the diodes to rectify the field and create a DC voltage between their electrodes, which leads to electro-osmotic flow [8]. The drive mechanism can also be used to pump fluids in microfluidic systems. The authors compare 1 and 3.7 mm diodes and find that the size has minimal effect on the final speed of the devices, with typical speeds of several mm/s. The authors report that the DC potential between the diode electrodes is also capable of producing small currents causing light-emitting diodes to light up. These currents could also be used to power built-in circuitry and electronics. This is an intriguing propulsion mechanism because it is driven directly by electrostatic fields and operates in fluidic environments. It is not clear how the need for field strengths of $\sim 100\ V/cm$ will influence its application.

2.2.3 Solar-Powered Microcrawler

Electrostatic actuators have proven quite popular for use in traditional MEMS systems. Parallel-plate and interdigitated-electrode arrangements are used in a wide variety of systems to create electrostatic actuators and sensors. They have also been adapted for use in wireless systems as demonstrated in this example. Hollar et al.

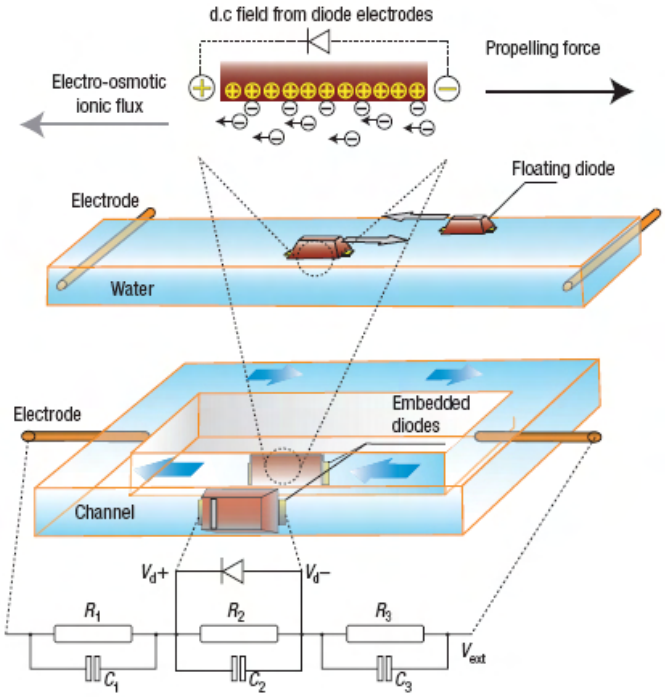

Figure 5: Externally applied AC electrostatic fields are rectified by diodes and create DC potentials between the electrodes, causing electro-osmotic flow across the surface. This flow can be used to drive floating diodes across the fluid surface or create a pumping action in channels with diodes embedded in the walls [8].

present an example of microrobot actuation and locomotion using solar cells [24]. By combining the cells with onboard circuitry to power and control electrostatic inch-worm motors, a robotic platform that can crawl across flat surfaces was created. The robot shown in Figure 6 was assembled from three separate chips due to process and material incompatibilities. The separate chips contain the motor and legs, the solar cells and the digital sequencer. Custom-built logic circuits were designed with the control sequence needed for a crawling action, and motion begins as soon as light levels are sufficient to generate the needed voltage.

This example of wireless power transmission and microrobot propulsion is included to demonstrate how important power transmission and conversion are for microrobots and wireless actuators. The entire crawling robot is nearly 9 *mm* long, significant parts of which are occupied by the solar cells and the digital sequencer. Even if an

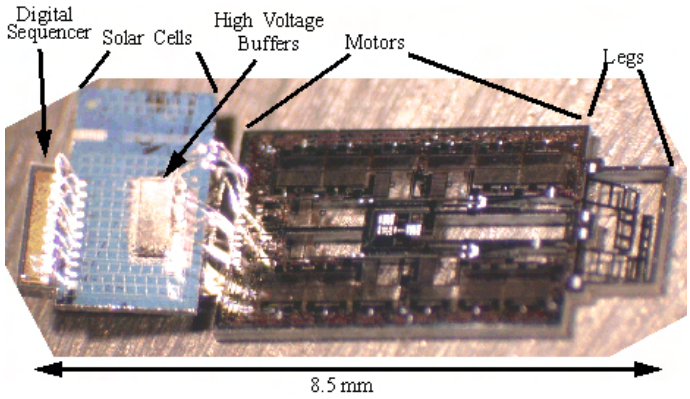

Figure 6: Electrostatic inchworm motors swing the legs down, causing the robot to crawl to the right. The digital sequencer feeds power from the solar cells to the high-voltage buffer where it is converted to 50 V to operate the motors [24].

integrated or stacked system could be developed, it would still be many square mm due to the size of the motors and required area for the solar cells. The advantage of this system is not its miniaturization, but rather its ability to operate remotely and gather its energy from light, much like the next example, which proposes a different way to harness photon energy.

2.3 Thermal Actuation

Thermal actuators are another common method of MEMS actuation that have been adapted to wireless systems. The use of thermal actuators in wired microsystems has proved popular where joule heating of thermally active arms and fingers with small currents is possible. Combined with the low heat capacity of microsystems, thermal actuation has proved to be an efficient, rapid, and easily controlled method of actuation in systems where large heat gradients and resulting thermal expansion can be harnessed. Early published examples of small MEMS-powered robotic platforms typically consisted of arrays of thermally actuated bimorph fingers that could be uncurled when passing current through them. Many researchers demonstrated motion with with inverted silicon chips connected to external power sources. When adapting thermal actuators to wireless systems, new sources of heat or energy must be found. Generation of high open-circuit voltages, such as those described by Hollar et al.

above, are achievable, but generating high currents to power microactuators is much more difficult. To address these challenges, several groups have proposed the use of concentrated light to generate heat and drive thermal actuators and are discussed in the following sections.

2.3.1 Self-Modulated Incident Light

Baglio et al. propose that small robotic platforms with thermally activated legs could carry their own incident light-modulation and focusing systems to concentrate light to heat and actuate legs for walking [4]. By focusing light through a microlens, the active part of a leg could be heated faster and to higher temperatures without heating the rest of the device. Combining this with a method for modulating the light transmission to individual legs, a robot platform with six legs was proposed that would walk or crawl, similar to an insect. The authors present the idea and investigation into subcomponents in several papers but no reports of working prototypes were found. If such a system could be developed, it has the potential to form the basis for an autonomous robotic platform capable of harvesting energy from incident light. Additionally, thermal actuators are generally considered to be more robust and contamination tolerant than high-voltage electrostatic actuators as used by Hollar et al. The need for microlenses, power for the light modulation and control circuitry led the authors to propose a 3 mm long prototype platform, but substantial reductions are conceivable. As the next example shows, thermal actuators can be made quite small.

2.3.2 Directed Laser Heating

In this case, a thermally actuated platform is reduced to smaller than 30 μm in diameter and presented by Sul et al. [46]. The actuator/platform is shown in Figure 7 and consists of a three-legged, metal bimorph device that rests on the sharp tips of its curled legs. Thermal heating of a leg by a laser-beam pulse fired through the observing optical system causes the activated leg to curl and pull the device across the substrate. Multiple devices could be controlled under one microscope with an appropriate laser scanning system. The authors report on the importance of fast

heating and actuation of the leg in creating an impact where the impact forces are enough to overcome stiction and other surface interaction forces. At first glance, a system such as this would be restricted to operation under a magnifying optical system to allow for the accurate addressing of individual legs. This restriction could conceivably be lifted by designing the legs with different materials that absorb at unique wavelengths and than applying blanket excitation with specific wavelengths to control individual legs, effectively creating an intelligent system that receives both power and control signals from the wavelength of the light.

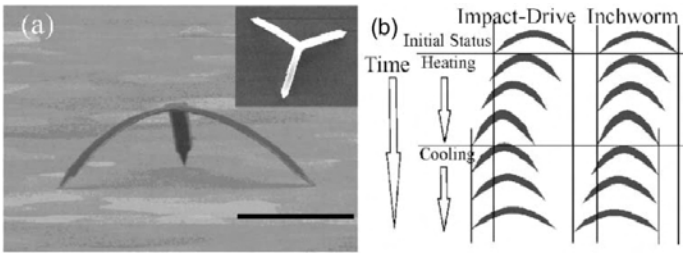

Figure 7: Thermally actuated untether impact-driven microdevices with (a) a scanning electron microscope (SEM) image of the device and (b) idealized drawing of locomotion methods [46].

2.4 Magnetic Actuation

Electromagnetic motors and actuators are omnipresent in the macro world. Historically, they have not been well received in the micro world due to issues of integration, fabrication and scaling. However, recent interest in expanding the use and functionality of MEMS actuators has brought about a revived interest in micromagnetics. Magnetic actuation can be divided into several general approaches, including using magnetic forces to pull magnetic bodies through a median, or applying magnetic forces or torques to a magnetic body in such a way that the body exerts forces on its surroundings to propel itself. Several groups have published results on the use of magnetics for wireless actuation for small remote microrobotic platforms; they are reviewed in the following sections.

2.4.1 Magnetic Torque-Based Actuators

Abbott et al. recently published a paper comparing the effectiveness of direct pull on microrobot platforms and magnetically rotated helical swimming platforms [2]. They showed that, for a similar configuration of coils and current limits, there is a specific body size, usually a few mm, below which helical swimmers using rotational torque and screw-like propulsion becomes more effective than pulling on magnetic material with a field gradient.

Sendoh et al. report on the use of screw-shaped magnets that can be moved through liquids or soft solids with the help of a rotating magnetic field [45]. The magnet is magnetized perpendicular to its long axis, and threads are machined in its surface, as shown in Figure 8. When placed in a rotating magnetic field, the magnet than rotates around the long axis and the screw shape propels it forward or backward. In this situation, the magnetic field is not used to directly propel the robot, rather it provides a torque. allowing the robot to be self-propelled. It was shown that high-strength NdFeB magnets provide enough torque that the robot can burrow through muscle tissue. By varying the dimensions, pitch and properties of the magnets and threads, they designed screw actuators with different step-out frequencies, allowing varying speed control of two actuators in the same driving field.

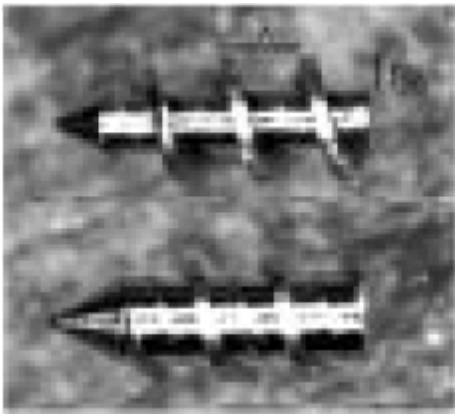

Figure 8: Screw-shaped magnetic actuators drive themselves through their environment powered by the rotation of external magnetic fields. The upper and lower magnetic screws measure 6 and 9 mm long respectively [45].

Bell et al. present a much smaller example of the screw-shaped magnetic actua-

tion in their work on flagella-like propulsion with helical coils [6]. Epitaxially grown bilayer beams with well-characterized internal stresses are grown and patterned on a suitable substrate at specific angles to the underlying crystallin orientation. Controlled underetching allows the beams to coil as they are released, as shown in Figure 9. The addition of a thin nickel dot to one end of the coil allows the coil to be rotated by an external magnetic field. The devices can move forward and backward, turn in place and swim against the field gradient.

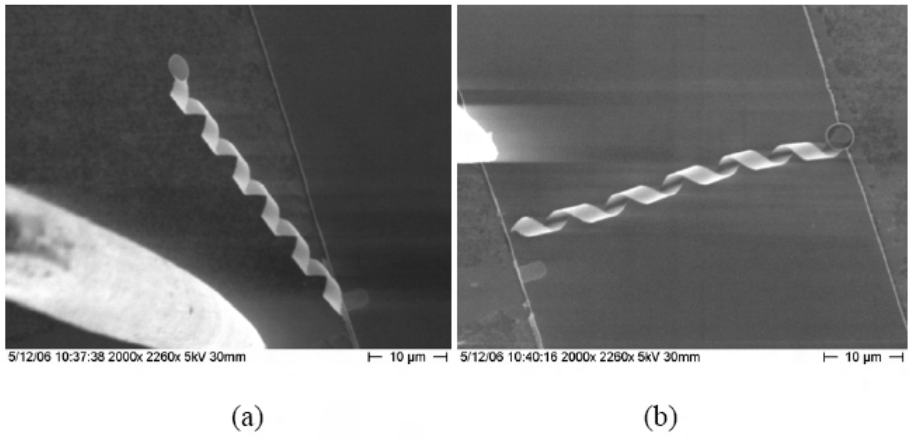

Figure 9: SEM images of 40 μm long microfabricated helical coils with nickel dots to capture rotational forces from external magnetic fields [6].

Another example of propulsion by means of a rotating or alternating magnetic field is given by Miki et al. and is shown in Figure 10 [37]. In this example, a small helicopter was built using magnetic materials for the rotors. It was able to hover successfully, although the system had to be constrained in two dimensions to prevent it from tipping or being pulled into regions of higher field strength due to the relatively low damping effects offered by air.

A further example shows a magnetic robot utilizing iron powder embedded in flexible silicon rubber to make fins that flap with the repeated application of a uniform magnetic field [36]. Figure 11 demonstrates the operating principle. Application of a magnetic field causes the iron-containing polymer fin to bend to align its long axis with the field. The fins return to their undeflected state when the field is removed. This flapping action drives the robot body forward.

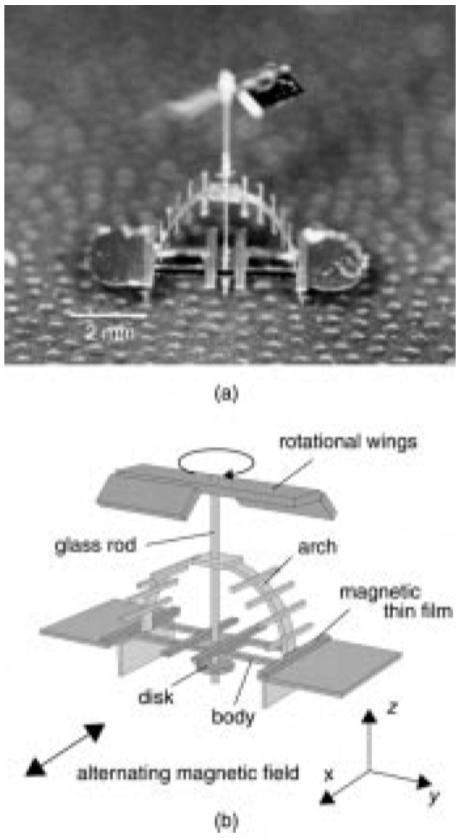

Figure 10: Small helicopter device driven by an oscillating field, which causes the rotor to rotate and produce lift. The device measures approximately 8 mm wide [37].

These examples use the energy of external fields to actuate parts of the robot body to push against the local media, providing propulsion. They differ from the following examples of magnetic microrobots that use magnetic field gradients to pull on magnetic bodies while the local media retards the movement with viscus damping, leading to force-dependent terminal velocities.

2.4.2 Magnetic Translational Force Actuators

Work reported by Martel et al. focuses on the use of an MRI to move and provide visual feedback of the location of a small steel sphere [18,34]. They demonstrate that an MRI is capable of moving a steel sphere with its normal imaging coils and that the

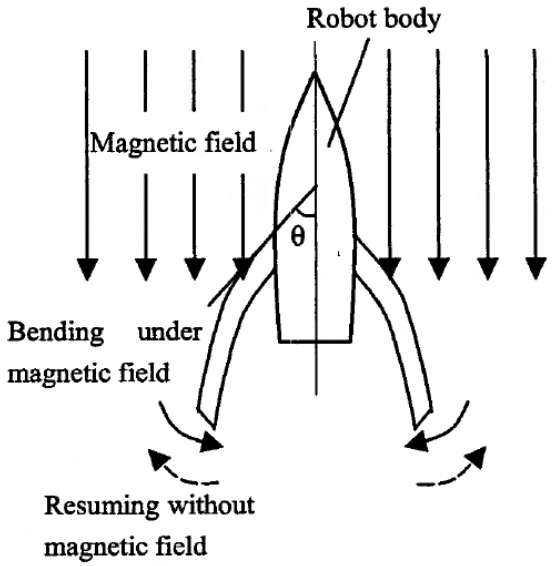

Figure 11: Microrobot platform propelled by flapping fins constructed of flexible polymer with embedded magnetic powder. Application of an external magnetic field bends the fins to align with the field and provides a propulsive force. The device measured 20 mm long and 14 mm wide [36].

magnetic artifacts of the steel leads to difficulties in precisely imaging the location of the sphere. Special tracking algorithms need to be developed to accurately track the robot. The focus of this published work is on localization and control in an MRI using a 3 mm steel sphere to simulate robots.

Floyd et al. present a laser-shaped permanent magnet that is used as a micro-robotic platform, shown in Figure 12 (a) [19]. The magnetic body is pulled across a flat surface with pulsating external magnetic fields generated by four coils. By including a fifth coil under the surface, the added z component of the magnetic field causes the robot to tip up on one end, as shown in Figure 12 (b), reducing stiction and allowing the robot to rotate around its center of mass and further reduce friction when the pulling field is pulsed. They report velocities on the order of 3 mm/s as well as the ability to operate in water and on unprepared flat surfaces.

The IRIS group at ETH Zurich is investigating magnetic microrobots for in vivo biomedical procedures [53]. The robotic platform is microassembled from individual parts composed of electroplated nickel, polymer or silicon. Figure 13 shows both parts

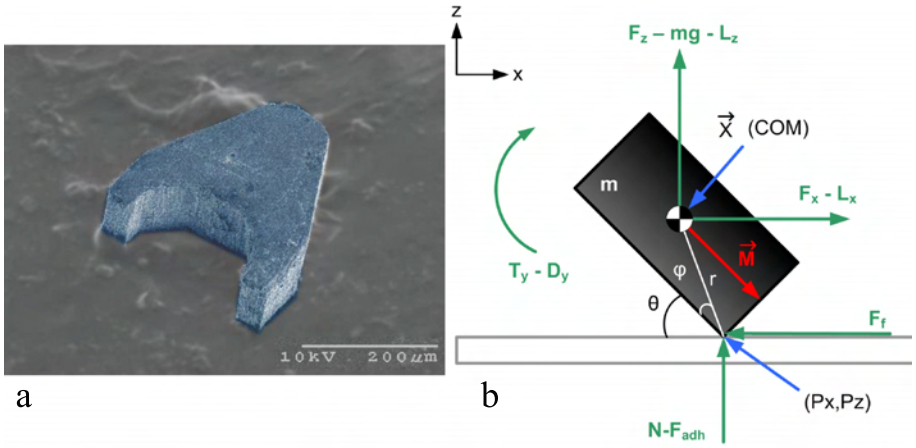

Figure 12: (a) Microrobot cut from a large permanent magnet with dimensions of 250×130×100 μm; (b) The addition of a z component to the magnetic field tips the robot on end, reducing friction and making it easier for the robot to jump forward during pulses. The magnetic piece measures 250×130×100 μm^3 [19].

and an assembled robot.

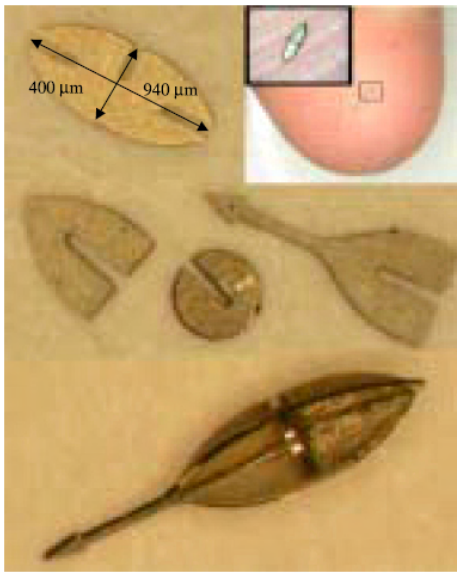

Figure 13: IRIS biomicrorobot platform with parts and final assembly [53].

The use of multiple parts and materials allows the robot to be magnetically actuated while facilitating the integration of silicon-based sensors and actuators. The

original robot measures 1,000 μm long and 400 μm wide, and is constructed from 50 μm thick pieces, although other robots have been built with lengths varying from 500 to 2,000 μm. Figure 14 shows a 500 μm long model in the tip of a 20 gauge needle.

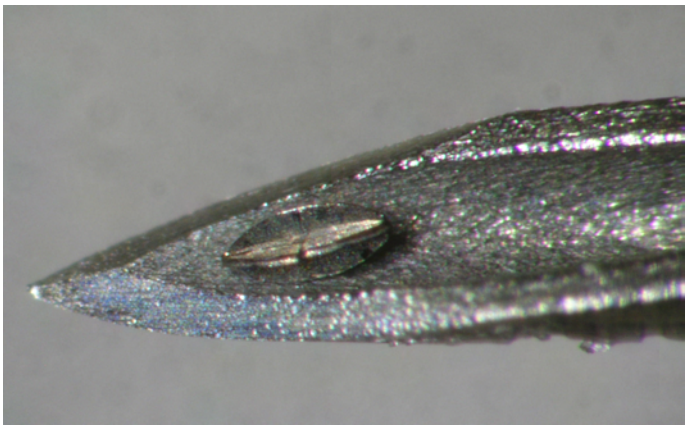

Figure 14: 500 μm long biomicrorobot in the tip of a 0.9 mm needle (20 gauge).

As part of the same project, Ergeneman et al. published work detailing the development of an oxygen-sensing system that can be used in conjunction with the microrobotic platform for localized oxygen measurements in the vitreous of the eye [17]. The system relies on the use of oxygen-sensitive dye that is extremely responsive to small changes in levels of dissolved oxygen at biologically significant concentrations. Abbott et al. of the same group published work detailing their investigations of the torques and forces on soft magnetic bodies in a magnetic field [1]. They present experimentally verified but counter-intuitive results showing that maximum torque on an ellipsoidal body is achieved at 70° from the long axis. The group is also investigating drug delivery methods and retinal vein puncture forces for use with the microrobotic platform. The lack of suitable wireless actuators for use in this project provided the initial motivation for the development of the wireless resonant magnetic microactuators detailed in this thesis.

2.5 Rectification and Impact Drive

Rectification of oscillatory motion, impact drives and linear-to-rotary converters are other topics that are important to the development of wireless actuators. Many of the

wireless actuators and propulsion methods for microrobots presented earlier in this chapter rely on the conversion of oscillatory or rotary energy to linear motion. Others convert the displacement of short throw actuators to long-distance displacement or propulsion. The capture and conversion of energy from resonant and short-throw actuators to usable forms is an important component of a successful system. This section will present some of the key examples of microactuators that demonstrate rectification, impact drive and motion conversion.

Microresonators of a variety of "flavors" are relatively simple to fabricate and operate. They typically enjoy high resonant frequencies and high quality factors (Q), and can be used as both sensors and actuators. Several examples of actuators were presented earlier in the chapter where the system frequency response was used to control multiple actuators with a single source of broadcast actuation energy. These cases relied on impact and rectification to convert the resonant or rotational energy into useful motion.

Impact actuators are commonly used in macro systems where the instantaneous delivery of large amounts of energy is needed to overcome mechanical restraining forces. Jack hammers, impact wrenches, pile drivers and hammer drills all rely on the sudden release of stored kinetic energy. By collecting the smaller forces that are injected into the system over the nonimpact part of the cycle, this energy can can be stored for instantaneous release. This creates a mechanical amplifier that decreases the duty cycle of the applied forces but increases the peak force, often by many orders of magnitude. Some of the early investigations into microimpact are presented by Lee and Pisano (1993) [29]. The authors also demonstrate an electrostatically driven angular microvibromotor that is driven by oblique impact of a pointer with a rotating wheel as shown in Figure 15 [28]. The pointer is attached to a bimodal flexure, which is driven by two comb-finger electrostatic actuators. By selectively choosing at which resonant mode to drive the pointer, the direction of impact between the pointer and the wheel can be changed. It is reported that the wheel can be driven clockwise or counterclockwise at speeds up to 60,000 rpm. In this situation, the linear motion of the comb finger actuators is converted to rotary motion through impact and selection of different resonant modes, allowing driving in different directions. The rectification allows limitless rotations to be driven by a short-throw electrostatic actuator.

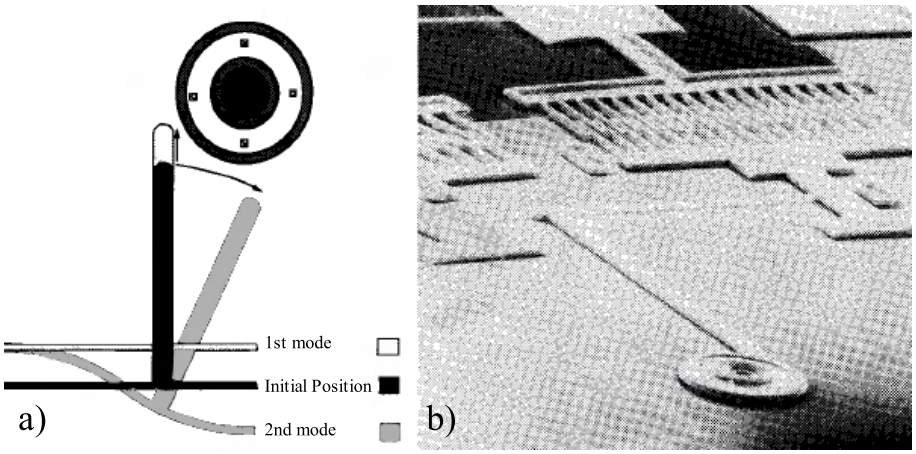

Figure 15: (a) Schematic of the device showing the two resonant modes and the resulting motion of the pointer tip as it impacts the rotating wheel; (b) SEM image of the fabricated device with the wheel in the lower center and the two comb drive actuators in the upper right and left [28].

Another rotary motor design is presented by Tabib-Azar and Satapun in their paper describing a high-torque rotary micromotor, shown in Figure 16 [47]. The motor consists of a central rotor with thin fingers extending at an angle from the edge. The rotor is situated between two oscillating actuators that are driven with a phase difference of 180°. The actuators contact the tips of the fingers during the inner extremes of their motion. This contact with the fingers transmits both normal and tangential forces through the fingers to the rotor. As the actuators move toward the center of the rotor, the fingertip remains in static contact with the actuator, causing the rotor to rotate. When the actuator reverses direction, the fingertip slides against the surface due to lower normal force, and the rotor remains in the new position. Careful design of the actuator travel distance, finger angle, length and number ensure that a second finger is in position for the next oscillator stroke. Compared with other rotary motors, which typically produce torques in the $pN \cdot m$ to $nN \cdot m$ range, it was expected that this design would produce $mN \cdot m$ torques. Macro-scale models of the motor were built but no micro-scale results were reported.

Traditionally, piezoelectric actuators offer limited travel range based purely on their physical change in dimension. More recently they have seen increased use in

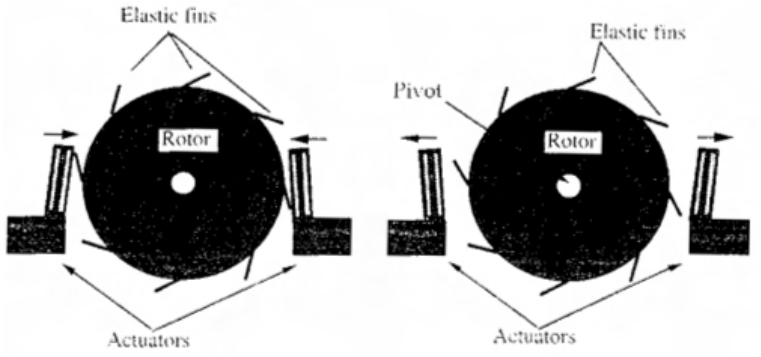

Figure 16: Linear to rotary converter powered by a swinging arm pushing against the ends of flexible fingers [47].

systems where long-range motion is achieved through stick-slip actuation or impact. By varying the rising and falling slopes of the driving sawtooth waveform, piezo actuators are used to move SEM and TEM sample holders around a microscope stage with sub-μm precision [31,32]. The system works by relying on the difference between static and dynamic friction coefficients. By using a sawtooth waveform with one side significantly steeper than the other, inertial forces created by the mass mounted on the free end of the piezo overcome the static friction when moving quickly in the desired direction and remain below the level of static friction while moving slowly in the other direction.

These examples represent the state-of-the art in microrobot propulsion and compatible wireless actuators. The next chapter begins the discussion of magnetics, starting with the basics of magnetic materials and their interactions, followed by an investigation into the modeling of magnetic forces between microfabricated magnetic bodies.

3 Overview: Magnetics and Magnetic Forces

3.1 Magnetics

The law governing the force between two magnetic poles was simultaneously discovered in 1785 by John Michell and Charles Coulomb. The law states that the force F between two magnetic poles of strength p_1 and p_2 separated by a distance d is given by

$$F = \frac{p_1 p_2}{d^2} \tag{3}$$

in CGS units with p defined in units of pole strength. Magnetic poles create magnetic fields, which are typically represented as H (or B) with units of oersted (Oe) defined such that a pole of unit pole strength in a field of one Oe will feel a force on one dyne, leading to the conclusion that field strength is inversely proportional to the square of the distance from the pole:

$$H = \frac{p}{d^2} \tag{4}$$

H and B have the same units but represent different things. H is often called the magnetizing field, while B represents the sum of H and the field created by magnetic material exposed to the field H. BH loops or hysteresis loops are usually used to describe the response of material to an applied magnetic field (H). A typical hysteresis loop is shown in Figure 17.

The horizontal axis represents the magnetizing field H going from positive to negative values, while the vertical axis represents either B, $4M$, or M. The plots differ by the magnitude of the vertical axis and the slope of the line. An unmagnetized sample placed in a magnometer begins at the origin. As the magnetizing field (H) increases, the magnetization of the sample moves along the dashed line until saturation is reached at point "a." After this level, further increasing the H field yields no further increase in magnetization. When the field is reduced to zero, the magnetization of the sample moves to point "b," labeled as the retentivity or remanence and commonly given as B_r. At this point, the value of H becomes negative and the magnetization of the sample follows the curve to point "c." Here, there is no net magnetization in the

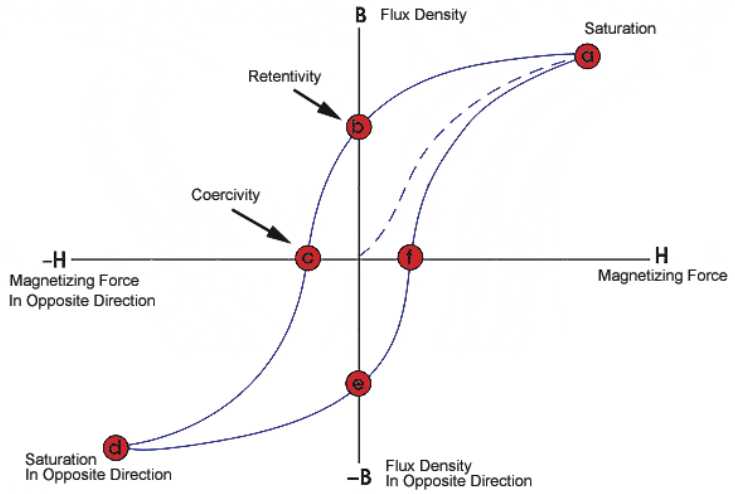

Figure 17: BH loop showing magnetization and hysteresis of a permanent magnetic material [39].

sample as the internal field cancels the externally applied field. This point is referred to as the coercivity (H_c). Further increasing H in the negative direction saturates the magnet in the other direction (point "d"). The decrease and reversal of H moves the magnetization along the other half of the loop, demonstrating the hysteresis inherent in magnetic materials.

Permanent magnets or hard magnetic material are characterized by large B_r and H_c values. The maximum product of the two (BHmax) is used as a measure of energy stored in a permanent magnet. The B_r value describes how strong a magnet is or how well the internal spins of the individual atoms remain aligned after the magnetizing field is removed. It also indicates how much force can be generated when the magnet attracts a piece of magnetic material. H_c is a measure of how resistant the magnet is to being demagnetized and how much force can be generated by trying to push the magnet with a similarly poled magnet. Soft magnetic materials such as nickel and iron easily lose their magnetization and are characterized by small values of B_r and H_c. Their saturation magnetization is often much higher than that found in permanent magnets, but they require large fields to saturate.

Figure 18 shows the MH curve of an electroplated nickel rectangle measuring 1,000×500×50 μm and measured along the long axis. Notice how the coercivity and

residual magnetization of the material is quite small compared with the saturation. The coercivity is approximately 5,570 A/m (7 mT, or 70 Oe) while the B_r is 0.136 T and the saturation is 0.75 T. Idealized soft magnetic material would have zero coercivity and residual magnetization, but in reality most materials have small nonzero values.

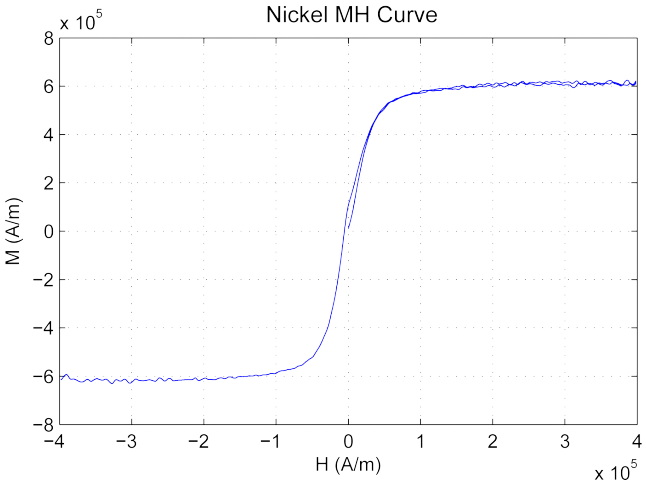

Figure 18: MH plot showing magnetization and hysteresis of soft magnetic material.

Magnetic materials can only be completely explained by their BH loop. They can be partially explained by two parameters—susceptibility and permeability. Susceptibility (χ_m) is the relation between the internal magnetization (M) and the magnetizing field (H).

$$M = \chi_m H \tag{5}$$

The total magnetic field or the magnetic flux density (B) is given in CGS units by

$$B = H + 4\pi M = H(1 + 4\pi\chi_m) = \mu H \tag{6}$$

where μ is the permeability. Loops as shown in Figure 17 and 18 can be plotted with M, $4M$ or B. Care must be taken to determine which value the author is reporting. Susceptibility is an intrinsic material property and is extremely sensitive to sample preparation, history and fabrication methods. Stresses within the crystal

grains can stress interatomic bonds and create stress anisotropies in the material, which have strong influences on the magnetic properties. The shape of the sample also plays an important role on the final value of B_r. Internal demagnetization causes samples that are short in the magnetized axis (compared with the other two axes) to lose a large fraction of their magnetization due to this energy-poor configuration. This demagnetization factor (N) can be calculated analytically for ellipsoids, but analytical calculations can not account for sharp corners or non-ellipsoidal geometries. FEA simulations must be used in these situations. N is given as a percentage of demagnetization and is shown in Equation 7:

$$B = H + 4\pi M - NM \tag{7}$$

When measuring the magnetic properties of a sample such as that shown in Figure 18, the measurement records the magnetic moment m of the material, which is volume dependent and related to the magnetization by the relation

$$M = \frac{m}{v} \tag{8}$$

where v is the magnet volume. The magnetic moment is related to the pole strength of the magnet p by the distance between the poles (d).

$$m = pd \tag{9}$$

In practice, the poles of a real magnet are distributed over a finite volume and the distance between them is difficult to quantify.

3.2 Magnetic Forces

Magnetic materials in magnetic fields are subject to both translational forces and rotational torques. The translational magnetic force and torque that are exerted on a piece of magnetic material with magnetization (M) in a magnetic field (B) are given as

$$\vec{F}_m = V_m(\vec{M} \bullet \nabla \vec{B}) \tag{10}$$

and

$$\tau_m = V_m \vec{M} \times \vec{B} \tag{11}$$

Equation 10 shows that a magnet in a uniform magnetic field feels no translational force, only torques, which are defined by Equation 11. This is demonstrated by the operation of a compass in the Earth's magnetic field, which can be considered uniform compared with the size of the compass. Torque causes the needle to rotate and align with the local magnetic field lines. The local presence of large amounts of magnetic metal or naturally occurring magnetic minerals will bend the local field lines and deflect the compass needle.

While Equations 10 and 11 define the forces felt by magnetic materials in a magnetic field, it is useful to be able to calculate the the forces between two neighboring magnets. The magnetization (M) and pole strength (p) are related by the cross-sectional area (a) of a uniform magnet as shown in 12, which can be derived from Equations 8 and 9:

$$M = \frac{p}{a} \tag{12}$$

The forces between two magnets can be calculated using the pole strength p as shown in Equation 3 and the cross sectional area a of the magnet. If the opposite poles of two magnets are brought into contact with a contact area A in cm^2 with induction in the magnet B in gauss, than the force is given in dynes in Equation 13. This only works when the two magnets are in contact; force falls rapidly when the magnets are separated as indicated in Equation 3. The force also depends on the shape, interface quality and magnet properties.

$$F = \frac{AB^2}{8\pi} \tag{13}$$

3.2.1 Interbody Magnetic Forces

As previously stated, Equation 10 shows that magnetic material placed in a uniform magnetic field will feel no translational force, only torque to align it with the field. This is true for both hard and soft magnetic material, although soft magnetic material will be magnetized by the local field. If the shape of the soft material is such that

one axis is significantly longer than the other, shape anisotropies will create a torque on the material so that the easy axis (the axis with the lowest N value) is parallel to the applied field. If two pieces of material are placed parallel to each other in a uniform magnetic field that is parallel to the long axis of the pieces, they will both become magnetized with similar poles adjacent to each other. The fields from these poles will interact and create a mutual repulsion based on separation distance and magnetization as shown in Figure 19 (b). If the two pieces are aligned end to end, than the opposite poles at the end of the magnets will attract each other as shown in Figure 19 (a). Magnetic forces as described in Figure 19 are commonly used in magnetic reed switches, but no examples have been found of using them for microactuation.

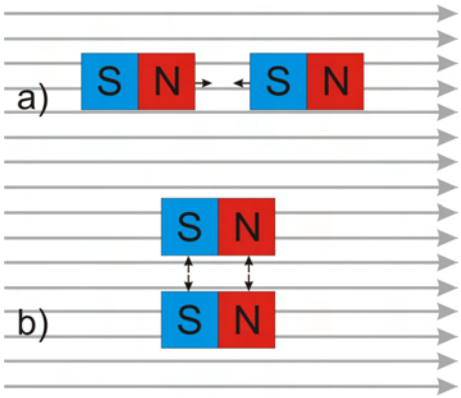

Figure 19: Interbody forces generated between neighboring ferromagnetic bodies in a uniform magnetic field: (a) attractive forces, and (b) repulsive forces.

Analysis of a typical magnetic system such as interbody magnetic forces typically does not allow for analytical solutions. Finite element modeling is often used and there are several software packages available to perform three-dimensional modeling. These packages take into account local magnetization based on H, χ_m and N, and calculate pole interactions dispersed throughout the material. Even with such modeling, care must be taken to validate the results with real-world measurement as the next section describes.

3.3 Comparison of Modeled and Measured Forces

An investigation of interbody forces was made with both experiments and FEM modeling. The experimental setup was modeled using a popular software package named Maxwell 3D. A microforce sensor was used to measure attractive forces between two microfabricated nickel bodies in a uniform magnetic field. Figure 20 is a cross-sectional view (cross section passes through the centerline) of the magnetic coils and cores used to generate the fields for the experiments. A hole in the left side core allows access to the center of the coils with a sensor mounted nickel body. While providing access, the hole in the core also disrupted the uniform field between the cores. Figure 21 shows a plot of the magnetic flux density along the coil centerline. The uniformity starts to drop significantly at about 8 mm from the right core, which starts at 35,000 μm. During experiments, the nickel bodies, with a total length of 2 to 3 mm, were mounted near the right side core to ensure that both nickel bodies were both fully in the region of uniform field.

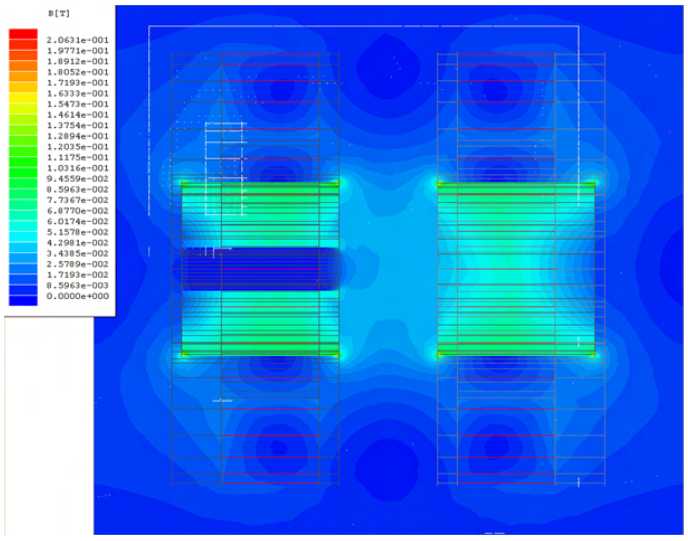

Figure 20: Two-dimensional plot of the magnetic flux density (B) in a cross-sectional view of a FEM (Maxwell 3D) model of the iron cored Helmholtz coil configuration used for interbody force tests. The rectangular areas of high field left and right of center are the iron cores, and the wire frame around it represents the coils. The core on the left has a hole in the middle to allow access with the force sensor.

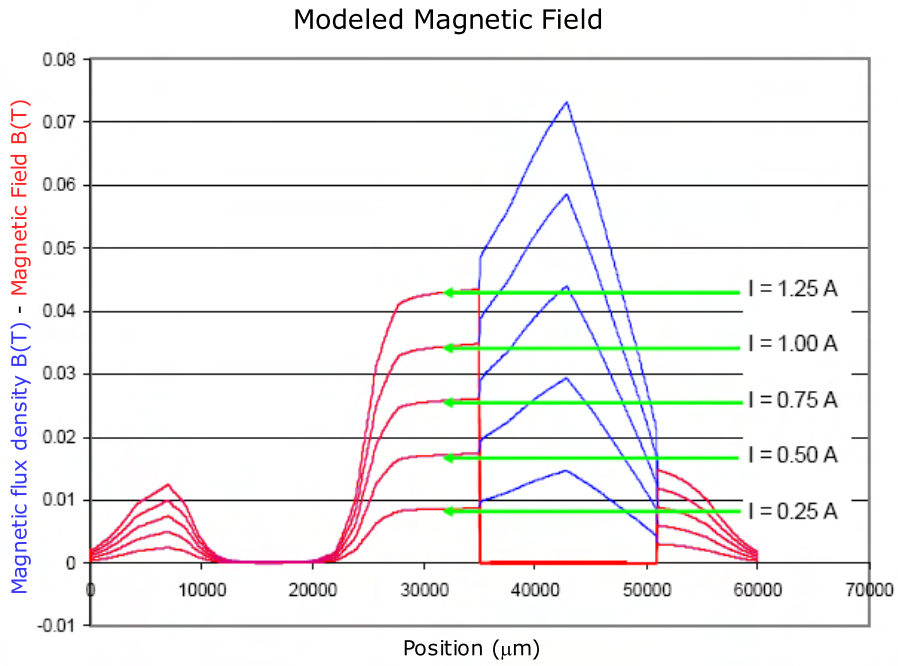

Figure 21: Model results showing the nonuniformity of on-axis field due to the access hole in the left core as shown in Figure 20.

Careful measurement of the magnetic flux density with a hall sensor probe showed that the measured field generated by the coils with iron cores was 23% higher than the modeled field (see Figure 22). The linear field response was 42.5 mT/A. The reason for the discrepancy is that the magnetic properties of the iron cores did not match those of the iron used in the model. This is common with magnetic materials where published properties of commercial material are the result of careful post-processing treatments or blending of different fabrication batches to ensure the product is within specifications. In this situation, common round iron stock of unknown magnetic quality was used to amplify the magnetic field, and measurements were made to compensate for the unknown magnetic properties.

Figure 23 shows the modeled and measured nickel bodies from prototype wireless resonant magnetic microactuator (WRMMA) devices, with dimensions listed in Table 1. The prototype was designed with a cavity for the inclusion of a spring between the two bodies. Small “ears” were added to the second body to provide a magnetic

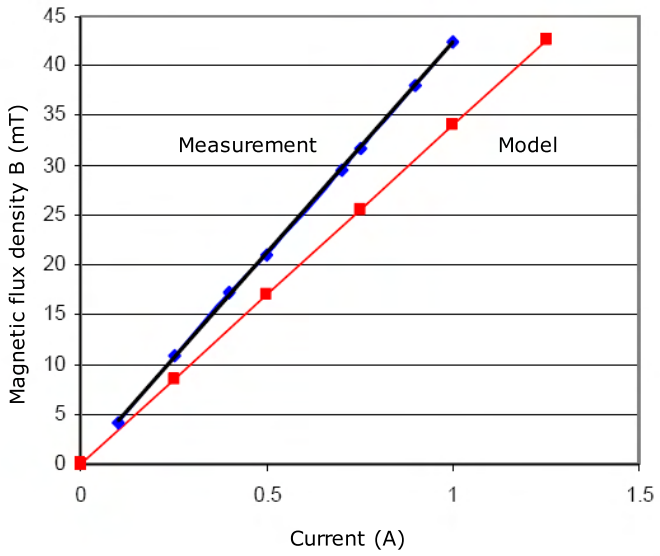

Figure 22: Comparison of the measured and modeled field strengths. Measured values were 23% higher than expected.

flux path between the two bodies. The device was designed so that with no forces or spring deflection, the gap between the bodies would be 10 to 14 μm. Measured body dimensions were compared with designed dimensions and variations were typically 1 to 6 μm. In addition to small changes in lateral dimensions, thicknesses varied across both the bodies and the wafer with the center being thinner than the edges in both cases due to the electroplating process. Thickness variations were often on the order of 5%. During modeling, material properties from Figure 18 and actual device dimensions were used with the average thickness. .

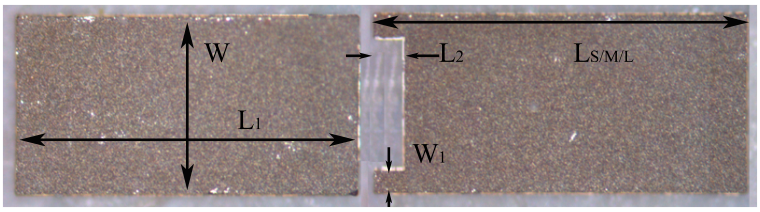

Figure 23: Electroplated nickel bodies of an early generation WRMMA. The bodies were designed to be separated by SU-8 fabricated leaf-type springs in the cavity between the bodies. The small "ears" are magnetic flux paths around the spring.

Table 1: Designed and measured nickel body dimensions in μm.

	Design	**Device**	Δ
W	480	483	3
L_1	1,000	1,003	3
W_1	60	61.4	1.4
L_2	90	89.7	-0.3
L_S	590	589.9	-0.1
L_M	1,090	1,097.1	7.1
L_L	1,590	1,594	4

Three different lengths of nickel bodies with ears were modeled (L_S, L_M, and L_L in Table 1). Results predicted slight variations in the expected forces with maximum forces of 1.3, 1.05 and 0.9 mN with no gap. Experiments confirmed that the force variation between the bodies was quite small, as shown in Figure 24, but the measured forces were approximately one-third of the expected values. Experimental and modeled data for the longest body are shown in Figure 25, where where modeled results are represented by the upper line with relatively few data points.

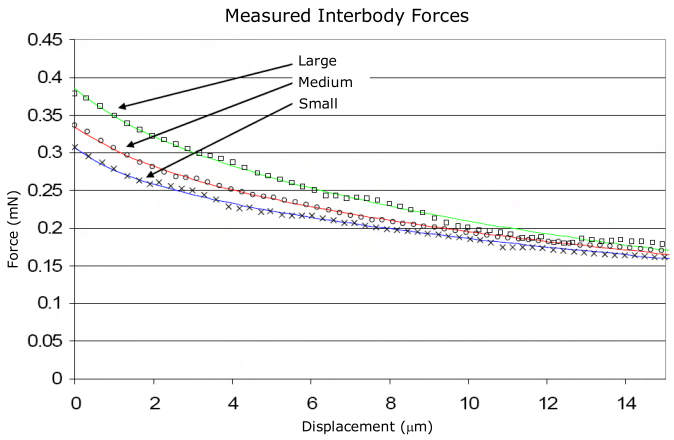

Figure 24: Measured interbody magnetic forces for three different sized bodies as described in Table 1 in a 42.5 mT field.

The deviation between modeled and measured results are attributed to the difficult-to-model sidewall angle and underplated nickel lip on the base of the bodies, as shown in Figure 26. The lip was a result of underetching of the photoresist mold and was

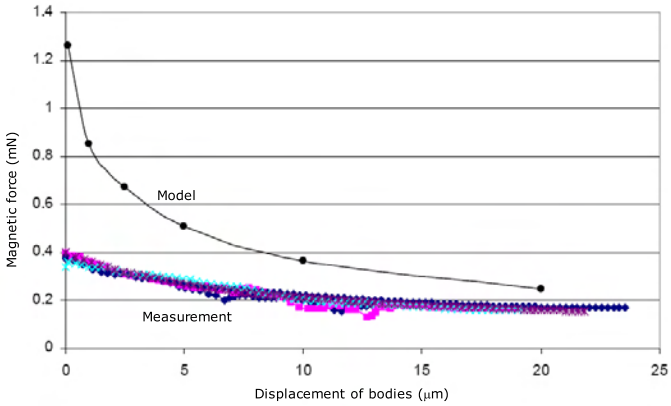

Figure 25: Modeled and measured interbody magnetic forces. The measured forces are significantly lower than the modeled forces.

typically very thin and could be broken-off before measurement. The side-wall angle was a permanent feature of the bodies and is an artifact of the sidewall angle of the photoresist mold used to form the nickel bodies during electroplating. Figure 26 shows two bodies with lines defining the mating sidewalls. The sidewall angle varied between devices and wafers, but was typically in the range of 3° to 6°.

Figure 26: Sidewall angles and lips on electroplated nickel parts that result from the fabrication process. These fabrication artifacts are a function of the processing and vary both across a single wafer and between wafers fabricated at the same time. The effects are exacerbated by the thick film resist used to fabricate the photoresist molds, which are discussed in a later chapter.

To show that the differences in measured and modeled forces resulted from sidewall angles, additional measurements were taken in which the probe-mounted nickel body was inverted with respect to the fixed body. In this situation, the sidewall angles are reversed with respect to each other, the gap between the bodies is uniform and the bodies come in contact with a larger, more repeatable area. Figure 28 demonstrates the differences in the zero-gap forces when the effect of the sidewall angles are

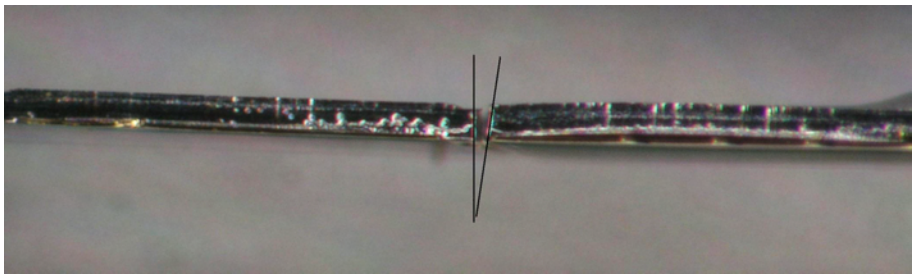

Figure 27: Nickel body sidewalls are not parallel due to sidewall angles in the photoresist molds during fabrication. The nickel bodies are about 1,000×500×50 μm^3.

removed. The two lower lines are from the same device with different orientations (normal and inverted) over a range of excitation currents. The inverted trace matches the single point on the right side of the plot, which is the expected magnetic force based on modeling results with no sidewall angle. Experiments showed that shifts in the lateral and horizontal alignment of the bodies have a minimal impact on the magnetic forces, while changes in angular alignment between the bodies have very large effects on the maximum force. The upper line in Figure 28 shows the effect of removing the spring cavity from the face of the body and was made by reversing and inverting the body with ears so two flat faces were interacting.

Figure 29 shows typical raw force scans at various coil currents. The two 0.5 A scans demonstrate a strong hysteresis in the force levels depending on the direction of motion of the sensor-mounted body. Forces were lower when the bodies were moving together and making contact than when breaking contact and moving apart. This hysteresis, along with a minimum force of 0.8 mN with no magnetizing field, is attributed to the small remanent magnetization of the nickel as shown in Figure 18.

There are many poorly understood and difficult to control variables that can affect interbody magnetic forces. In macro samples of magnetic material it is well known that machining, processing and tempering will change the materials' properties. Magnetic properties of commercial materials are the result of carefully developed processes and procedures designed to deliver repeatable and uniform properties. Processes and procedures are also important in the formation of electroplated microparts; changes in the thickness and plating conditions are well known to cause changes in the internal stress of the deposited material. These internal stresses deform the crys-

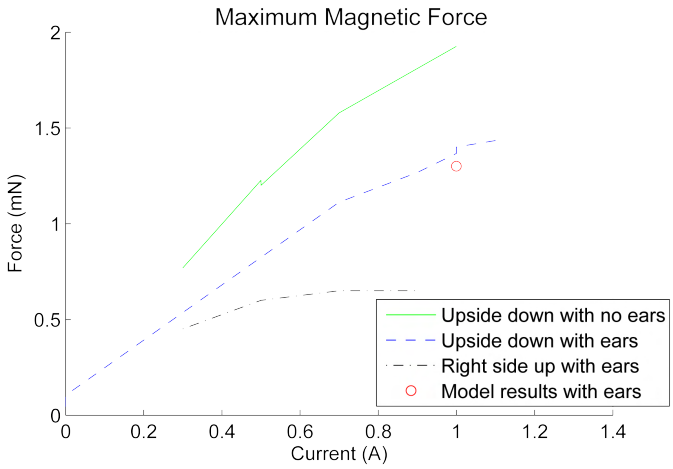

Figure 28: Plots of the maximum forces (zero gap size) between nickel bodies at various coil currents (field strength is 42.5 mT/A). Upside down and right side up with data ears is taken from the same body. Upside down with no ears shows the effects of the spring cavity in the face of the body. The single point for the modeled results is taken from Figure 25 and is in good agreement with the measured values.

tallin lattice spacing and change the magnetic properties. In some situations, crystallin anisotropies develop during the plating process overpower the expected shape anisotropy and change the easy access of the deposits. These uncertainties are best overcome with consistent deposition procedures that ensure repeatable results. They have largely been sidestepped in this analysis by adopting the the use of an additive-free nickel bath and closely controlling the deposition parameters to ensure consistent results.

Perhaps the most important area of uncertainty in determining the magnetic forces between the two bodies is the geometry of the mating magnetic faces. Microfabrication methods typically cause non-parallel sidewalls that hold faces apart or reduce the contact area. In some cases, underdevelopment can lead to rounded faces on magnetic bodies. These interface variations and the misalignment between bodies lead to large reductions in the interbody forces compared with modeled results. To account for these uncertainties, magnetic actuators should be modeled and designed with large safety margins that will allow for operation when magnetic forces are significantly lower than expected. In practice, it is easier to adjust the magnitude of the external

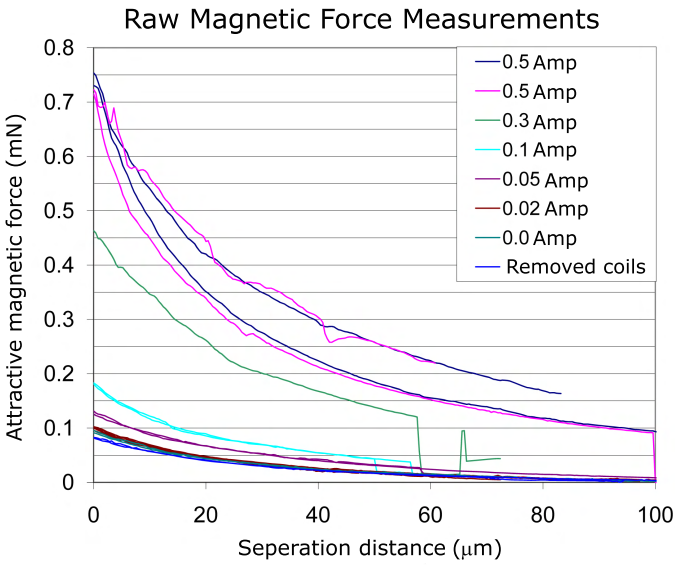

Figure 29: Plots of force data with coil excitation current ranging from 0 to 0.5 A (0 to 21.25 mT field strength). Even with no external magnetic field (coil current at 0 or coil removed from experiment), remanent magnetization of the nickel bodies created forces of approximately 0.8 mN.

magnetic field than reduce spring dimensions, make new masks and fabricate a second batch of devices.

The next chapter continues with a discussion of the basic operation of an actuator designed to harness the interbody forces that were introduced in this section.

4 Modeling and Design of a WRMMA

Few methods for wireless microactuation have been documented in published literature. The lack of suitable miniaturized power sources is a major obstacle to their development. Actuators by definition must do work and expend energy on their environment. As desired forces and working distances increase, energy requirements also increase. One solution is that wireless actuators can receive their energy from their environments or from an outside source. Proposed power sources include adenosine triphosphate (ATP), electromagnetic radiation over a variety of wavelengths, vibrations, and magnetic fields, several of which were presented in the first chapter. In addition to supplying power, methods of controlling the actuators must also be implemented to make the actuator useful. Depending on the application, individual actuators must be activated independent of neighboring actuators. Ideally individual addressing would be a feature of the system design and not require integrated control electronics. Selectivity in wireless systems can be achieved if the system is designed to operate at resonance with different actuators being sufficiently separated in the frequency domain to be individually actuated by frequency-dependent power [44]. Rectification of oscillatory motion is another key component of resonant actuators. Documented methods include impact, ratchet-like behavior and stick-slip motion, all of which can convert oscillating motion to linear displacement or rotation in microsystems. This chapter presents the working principle and design of a new class of wireless actuators named Wireless Resonant Magnetic MicroActuators (WRMMA). The actuators produce large forces and offer individual frequency based control by harnessing interbody magnetic forces with a resonant actuator.

4.1 Wireless Resonant Magnetic Microactuators

WRMMAs are powered by the interbody magnetic forces described in Figure 19. Combined with a pulsating external magnetic field, the forces excite a resonating structure from which rectified energy and motion can be extracted. Figure 30 shows the principle behind the actuator with the magnetic forces and restoring spring force. In the presence of a magnetic field, two soft magnetic bodies are magnetized and attract each other (Figure 30 (a)). When the field is turned off, the magnetization

returns to zero and the spring force pushes the bodies apart (Figure 30 (b)). By separating two soft magnetic bodies with a spring, a wireless resonant structure is formed. When driven at resonance by an external magnetic field, large amounts of energy are absorbed by the system. This energy can be captured by an appropriately chosen rectification method to create useful mechanical motion.

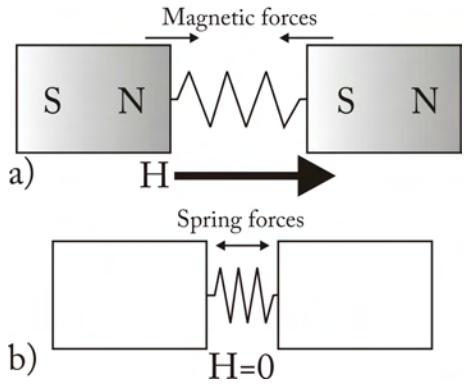

Figure 30: Sketch showing the (a) magnetic forces attracting two neighboring soft magnetic bodies in the presence of an external magnetic field and (b) the restoring spring forces pushing them apart when the external field is removed.

By using interbody magnetic forces in a resonating system, a unique actuator is developed that allows for wireless actuation and control of multiple actuators with one signal. Individual actuators can be selectively controlled by modulating the frequency of the magnetic field pulses that power the actuator. Additionally, the actuator also offers other advantages that make it useful in microsystems. By driving the system to high amplitude oscillations, impact between the two bodies can occur. By utilizing this impact to transmit a relatively large amount of stored kinetic energy over a very short period of time, forces that are much larger than the driving magnetic forces can be generated in the system. The basic design of such a system is also quite simple. It requires two magnetic bodies and a spring system which will not provide a magnetic flux path to short circuit the magnetic forces. It also scales comparable to or better than other actuation methods. The interbody forces shown in Equation 3 scale with the characteristic length (l) to the second power (l^2). This can be seen by combining Equation 12, where M is magnetization per unit volume and is scale independent, with Equation 3. Interbody forces scale similarly to electrostatic forces (l^2) and better than

translational magnetic forces, as given in Equation 10, which depend on the volume of the magnetic body (l^3). The task of generating sufficient strong magnetic fields at increasing resonant frequencies (resonant frequencies scale as l^-1) is perhaps the most technically challenging hurdle to shrinking WRMMAs to single or sub μm dimensions. It is expected that the physical limit to the predictable behavior of the interbody magnetic forces would be at the point where the magnetic bodies are composed of a handful of magnetic domains, or the product of the domain size and the actuation frequency (Hz) is in the same range as the domain wall velocity (magnetic domains grow and shrink by moving the domain wall, which has a measurable velocity).

The following sections present analysis, modeling, and simulation of the expected system behavior. The two final sections discuss proposed applications of the actuators based on the examples presented in the first chapter. The last section presents the MAGMITE platform and an explanation of its origin and operation.

4.2 Magnetic Modeling

As discussed in Chapter 3, calculation of interaction forces between soft magnetic bodies in a uniform magnetic field is best done numerically. In general, the bodies are magnetized by the external field and locally amplify the field at their poles according to Equation 7. This amplification is a result of the superposition of the external field and induced magnetization and demagnetization. It is often drawn in such a way that the local field lines appear to have been sucked into the magnetic material (see Figure 31). Figure 31 (a) shows two bodies aligned with the field. This produces a region of high field strength between the bodies which is energetically unfavorable and creates strong attractive forces. Figure 31 (b) shows two neighboring bodies at an angle to the applied field. This produces a region of high field between them, and on opposing corners–close to the direction of the applied field–causes a torque and subsequent rotation of the bodies to align with the field.

As mentioned in the previous chapter, accurate modeling of the magnetic forces depends on many parameters. In this device, electroplated nickel with magnetic properties (shown in Figure 18) is used to form the magnetic bodies. Figure 32 shows the expected magnetic forces between two nickel bodies in a 5 mT field. The force

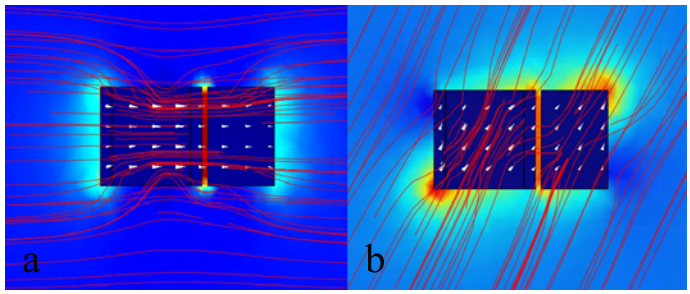

Figure 31: Graphical output of magnetic force modeling between two soft magnetic bodies in an external magnetic field. In (a), the long axis of the combined bodies aligns with the external field, creating attractive forces between the bodies. In (b), the external field is off axis, causing attractive forces and an aligning torque.

between the bodies scales linearly with the field strength as long as the external field remains in the linear response region of the material. With perfectly aligned contact, the forces between these two bodies is 10 μN. The modeled bodies are 150×130×50 μm^3 and lie with their 130 μm^3 axes parallel to the field as shown in the inset. Geometrical fabrication artifacts that influence the minimum gap size and contact area between the bodies are not included in the model, which assumes parallel sidewalls. Because of this, the modeled forces are taken as an upper limit and the device is designed to function with significantly lower forces.

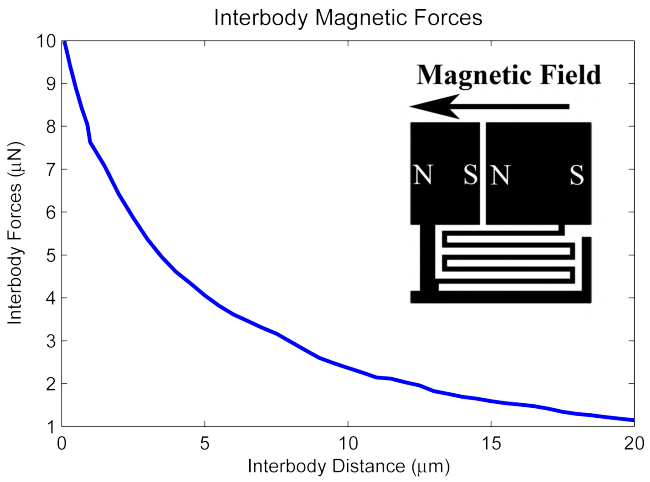

Figure 32: Finite elemental analysis results of the interbody forces between two nickel bodies.

4.3 Equations of Motion

During impact free-oscillations, the resonating system can be modeled as a damped-driven harmonic oscillator similar to those presented in undergraduate physics and engineering texts

$$F(t,x) = kx + c_1\dot{x} + c_2\dot{x}^2 + m\ddot{x} \tag{14}$$

where k and m are spring constant and mass. Linear and quadratic damping terms are given by c_1 and c_2. $F(t,x)$ is the excitation force received from the magnetic field and differs from the driving force given in Equation 1 due to the gap-dependent magnetic forces shown in Figure 32. Because the moving parts in the resonant actuator are quite small, the Reynolds number is much smaller than one and the quadratic damping term (c_2) can safely be set to 0. The resonant frequency can then be given as

$$f_d = \frac{\omega_d}{2\pi} = \frac{1}{2\pi}\sqrt{\frac{k}{m} - \frac{c^2}{4m^2}} \tag{15}$$

when linear damping (c) can not be ignored. In this situation, damping is quite weak and the simpler expression $\omega_n = \sqrt{k/m}$ is sufficient in most cases. In situations where damping is important, Equation 15 can be simplified by defining

$$\gamma = c/(2m) \tag{16}$$

and thus

$$\omega_d = \sqrt{\frac{k}{m} - \gamma} \tag{17}$$

When c is small, and the driving force is 0, a solution for the equations of motion takes the form of

$$x(t) = e^{-\gamma t}(Asin(\omega_d t + \phi_0)) \tag{18}$$

If a damped system is disturbed from its equilibrium position and allowed to decay freely, the amplitude of the oscillations die away at the rate of $e^{-\gamma}$. The peaks of the displacement or velocity amplitude can be fit with an exponential curve that will give

γ and thus c if m is known. Figure 33 demonstrates this behavior.

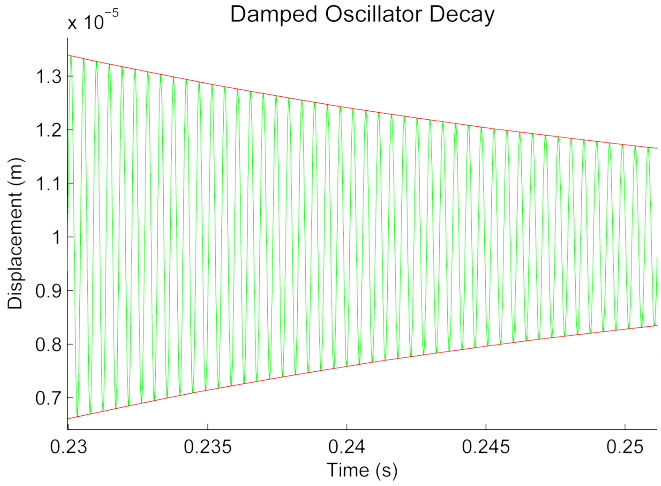

Figure 33: Plot of displacement versus time in an underdamped harmonic oscillator with no driving force. Fitting the exponential decay of the displacement peaks leads to the system damping factor.

In the absence of driving or damping forces, energy is conserved, and the sum of the kinetic and potential energy of a harmonic oscillator remains constant.

$$E = \frac{1}{2}m\dot{x}^2 + \frac{1}{2}kx^2 \tag{19}$$

Increases or decreases of the system energy can be calculated directly from damping and driving forces if they are known. When these parameters are not well characterized, they can be calculated from the the change in energy per cycle if it can be determined. The total energy of a resonant system scales as l^3 and is a property of all resonant systems irrespective of drive mechanism. Differentiating Equation 19 with respect to t and substituting in Equation 14 when $F(t, x) = 0$ gives the decay rate of the system energy.

$$\frac{dE}{dt} = -c\dot{x}^2 \tag{20}$$

Energy loss rates can be combined with steady state performance to determine energy absorption rates in situations where driving forces are poorly defined.

The rate of energy loss in oscillating systems is commonly defined by a quality factor (Q). The Q-factor of a system can be defined in many ways. One of them is 2π times the total energy divided by the energy lost in a single period, which can be found using Equation 20. With simplification, Q can be reduced to the following:

$$Q = \frac{\omega_d}{2\gamma} \tag{21}$$

Since accurate knowledge of damping coefficients in experimental systems is typically found experimentally, a more common expression for Q is based on the sharpness of the resonator response plot. Equation 22 is often used to evaluate systems for which actual data has been collected and damping is unknown.

$$Q \simeq \frac{\triangle f}{f_o} \tag{22}$$

The variable $\triangle f$ is called the "full width at half maximum" and is the width of the peak at half of the maximum response value, and f_o is the frequency of maximum response.

Resonant systems can be built and modeled with either torsional or linear springs. Equations 14 through 21 assume the system has a linear spring. The equations could easily be reworked for the torsional case with the substitution of the variables shown in Table 2. The behavior and analysis of the systems remains the same.

Table 2: Linear vs. torsional resonant systems.

Linear	**Torsional**
Force (F)	Torque (τ)
Linear position (x)	Angular position (θ)
Mass (m)	Moment of Inertia (I)

The moment of inertia for a solid cuboid with height h, width w, depth d and mass m is given as:

$$I_{cm} = \frac{1}{12} m(h^2 + w^2) \tag{23}$$

when the body rotates about the axes, passing through the center of mass in the

depth direction. In the situation when the axes of rotation is offset from the center of mass of the body by a distance r, the parallel axes theorem gives the shifted moment of inertia.

$$I_{shifted} = I_{cm} + mr^2 \tag{24}$$

4.4 Impact Modeling

Impact is an important component of the WRMMA and must also be included in the equations of motion. Impact between bodies can be modeled in a number of ways. The simplest and most frequently used is the coefficient of restitution. In the case of a single object rebounding off of a massive, immobile object, it simply gives the rebound velocity as a fraction of the impact velocity.

$$v_f = -c_r v_i \tag{25}$$

v_f, v_i and c_r are the final and initial velocities and the coefficient of restitution, respectively. In the case that the second object is not massive and immobile, the coefficient is given as:

$$c_r = \frac{v_{2f} - v_{1f}}{v_{1i} - v_{2i}} \tag{26}$$

This treatment of impact lumps all the the complexity of impact and material response into one parameter, which is experimentally determined. In the case that c_r has a value of 1, the collision is elastic and energy and momentum are conserved across the collision. Typically c_r is less than one, and while momentum is conserved, energy is dissipated. Despite simplification of an extremely complex interaction, the coefficient of restitution models impact quite well in situations where it can be experimentally determined. Lee and Pisano [29] present investigations into impact behavior between microfabricated structures with a numerical model using Equations 1 and 25. They compared model results to experimental data from a microfabricated impact experiment. They predicted and found the nonlinear jump behavior shown in Figure 34 and suggest that Equation 25 is sufficient to explain and accurately model

their system. Starting at point A in Figure 34, the frequency is slowly increased until point B is reached, where impact between the two hammers begins. Further increase of frequency leads to point C where the linear response would be expected to decrease in magnitude. Instead, large amplitude impact causing oscillations continue until point D, where the amplitude spontaneously drops to point E before continuing to point F. With a decreasing frequency sweep, the amplitude moves from point E to point C, then from point B to point A without exhibiting a similar behavior on the low frequency side of the response peak. The authors state that the frequency at which the drop from point D to E occurs was found to depend on the coefficient of restitution, with higher frequencies indicating a larger coefficient. They also state that external vibrations, air currents, and rapid frequency changes disrupt the steady state response and cause the oscillations to spontaneously drop to the low amplitude mode.

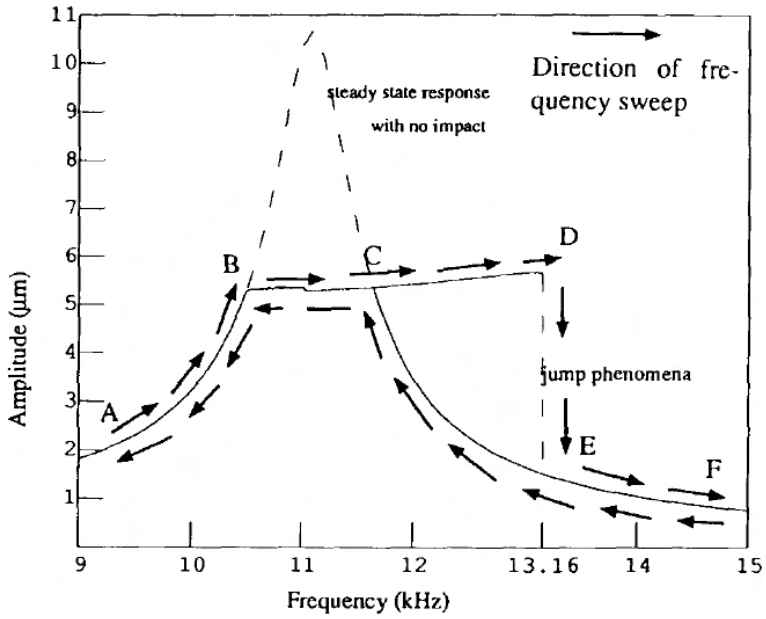

Figure 34: Plot from Lee and Pisano showing the nonlinear response of a microimpactor [29].

4.5 System Simulation

Due to the distance- and time-dependent driving force in Equation 14 and the occurrence of impact between the magnetic bodies, numerical simulations must be used to model the system behavior. A 1-D model of the system was developed in Simulink (a product of the MathWorks company and part of MATLAB) to investigate the performance of the actuator, compare to the measured actuator behavior, and investigate unknown parameters. The model is based on Equations 14 and 25, with the data from Figure 32 used to determine the magnetic forces. The graphically programmed model is shown in Figure 35.

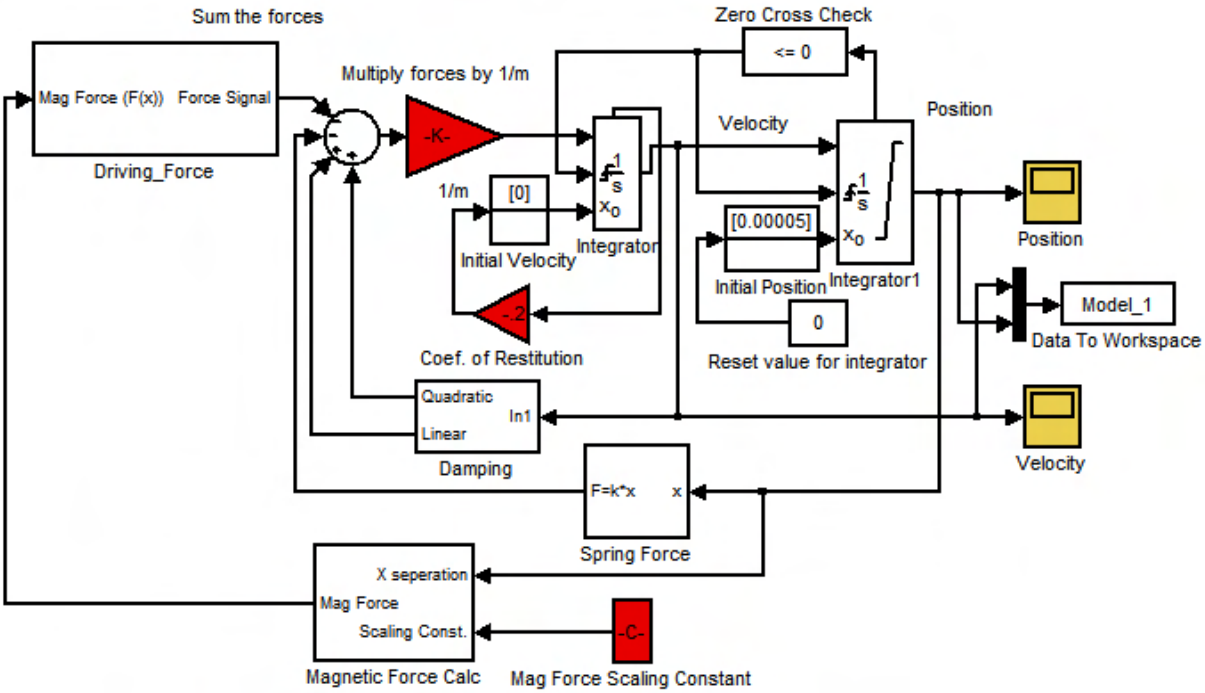

Figure 35: Numerical model created in the graphical simulation package Simulink used to predict the behavior of a 1-D damped-driven harmonic oscillator with position- and time-dependent driving forces.

In the model, the forces acting on the swinging mass are summed and divided by m before being integrated to find the velocity. The velocity is then integrated again to find the position. If the position becomes negative, an impact has occurred and the

program automatically extrapolates to find the zero crossing point. The integrators are reset with the new velocity determined by c_r and the position set to zero. The magnetic force is calculated from a polynomial fit of the data and scaled with a scaling constant. The scaling constant is tuned to match experimental data. This allows the driving forces to be adjusted for different driving field strengths and to compensate for inaccuracies in magnetic modeling. The magnetic force is multiplied by a driving signal that varies in amplitude from 0 to 1 to create the time- and position-based driving forces.

The simulation only models the behavior of a one-dimensional WRMMA and not the stick-slip motion of the MAGMITE microrobot, which is introduced at the end of this chapter as the demonstration platform for the actuator. Performance of the model was verified by comparing it to the behavior reported by Lee and Pisano (shown in Figure 34) and matching simulation output with measured behavior from the WRMMA. Results of varying c_r are shown in Figure 36. In concurrence with Lee and Pisano's findings, increasing c_r caused an increase in the frequency at which the drop from impact to normal oscillations occurred.

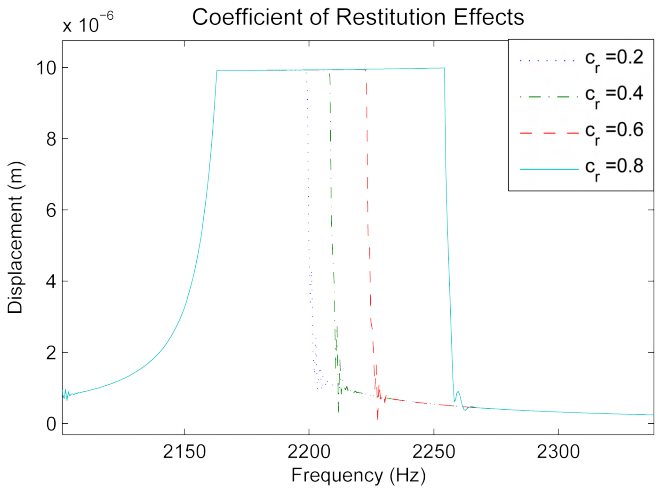

Figure 36: Simulation results from the simulink model showing "jump" behavior similar to that found by Lee and Pisano. Increasing the coefficient of restitution also increases the fall-off frequency.

The jump behavior described by Lee and Pisano was reported to be found only on the high frequency side of the of the resonance peak, as shown in Figure 34. In

the Simulink model, when driving the system with continuously varying frequency "chirps," the behavior occurs on both sides of the resonant peak when scanning up and down, as shown in Figure 37. The below-resonance frequency jump behavior nearly disappears once the excitation signal changes from continuous to stepped, even if frequency changes are as small as 0.1 Hz and the signal phase is preserved. Typical changes in drop-off frequency on downward sweeps are on the order of a few tens of Hz, while upward sweeps are typically several hundred Hz depending on parameters.

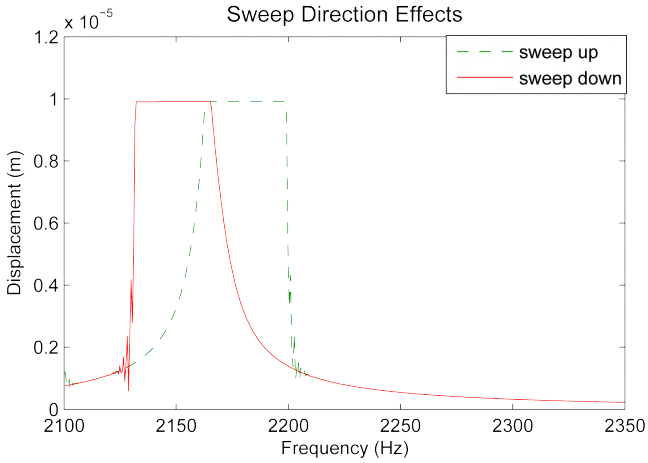

Figure 37: Simulation results showing the jump response when sweeping from both low to high and high to low frequencies with continuously varying frequency "chirps."

The jump behavior shown in the models can be explained by considering the effects of impact and rebound velocity. The initial rebound velocity of the hammer after impact due to the non-zero c_r effectively shifts the mechanical phase of the impactor forward in time so that it catches up to the driving signal, which is higher than the natural resonant frequency. As the driving frequency increases, the velocity of the oscillations must increase so the system can remain in phase. This increases the system velocity and displacement. Increasing c_r increases the amount of energy conserved in the system at each impact, allowing the mechanical system to keep up with the driving signal at higher and higher frequencies. During the upward sweep, the amplitude of the displacement during oscillations continues to increase with increasing frequency. This is due to the increased energy in the system from the higher frequency of oscillations, which increases the velocity and maximum displacement.

To analyze simulation data such as that presented in Figure 37, the physical displacement of the oscillating mass is recorded and an envelope function is applied to trace the upper edge of data. In simulations where the driving velocity is stepped, post-simulation analysis of displacement or velocity is used. Due to the discontinuous steps in drive frequency, large transient oscillations in displacement data are often observed and mean values of steady state behavior are a better representative of system behavior. Fast fourier transform (FFT) analysis of the simulation data is of relatively little use due to leakage and spreading of bin energy. Figure 38 shows three different analysis methods on the same simulation displacement data. Since true velocity or displacement is typically more useful in system analysis and windowing was not used in spectral analysis to correct for energy leakage.

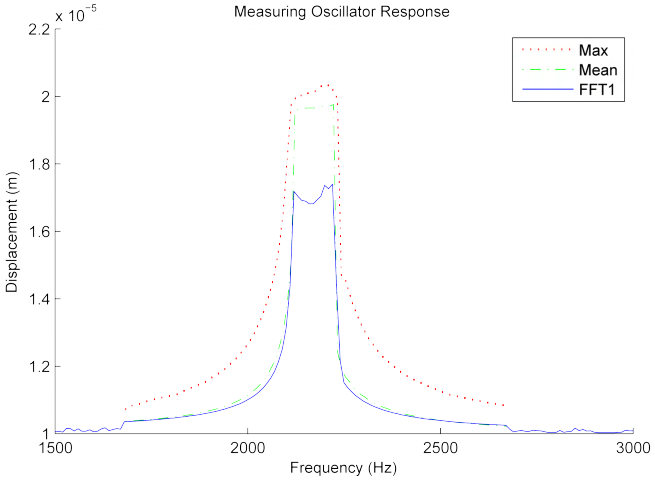

Figure 38: Analysis of displacement data using max, mean and FFT peak hold. Transient motions due to stepped excitation frequencies cause large differences between max and mean values for non-impacting frequencies. Leakage of energy in FFT analysis makes accurate recovery of actual displacement amplitudes difficult.

System response to various driving fields was also investigated by comparing system displacement in response to five different driving waveforms with identical RMS values. Figure 39 shows waveforms and their RMS value of 0.707. S1 is simply a sine wave centered at 0 with min/max values of +1 and -1. S2 is a full sine wave with a maximum value of 1.15 and minimum value of 0. S3 is the positive half of a sine wave, with the maximum amplitude of $sqrt(2)$. Sq1 is a square wave with peak value

of 1 and 50% duty cycle, while Sq2 is a square wave with peak value of $sqrt(2)$ and 25% duty cycle. Due to the nature of the physical WRMMA system and the fact that repulsive magnetic fields can not be generated with an on-axis field (see Figure 19 (a)), S1 was modified to be the absolute value of the sine wave and the driving frequency was half that of the other waveforms.

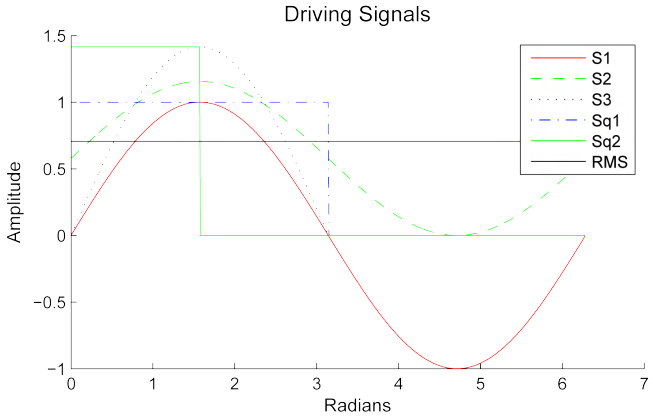

Figure 39: Plots of the five different driving signals used in simulations to compare system response.

Table 3 shows the maximum mean displacement from from simulations with identical parameters using the waveforms from Figure 39. The waveform labeled S3 induced the largest response, followed by the square waves. Figure 40 shows the simulated interbody forces resulting from the S3 and Sq1 waveforms. The S3-generated forces clearly show the results of sinusoidal driving waveform and it is difficult to detect the position dependence of the magnetic forces. The dependencies are clearly visible in the data generated with the square wave.

4.6 Proposed Applications of WRMMAs

The preceding sections presented the concept of a wireless resonant magnetic microactuator that can be used as a source of power in a wireless microsystem. A key component to the successful implementation of any motor is a suitable method of extracting the motion and energy and converting it to useful energy and motion. In effect, with the motor in hand for a microrobotic actuator, a suitable drive train must

Table 3: Simulation response to driving signals shown in Figure 39. Responses are normalized with maximum response from the S3 signal and taken under excitation levels too low to cause impact.

	Displacement
S1	0.34
S2	0.70
S3	1.0
Sq1	0.84
Sq2	0.95

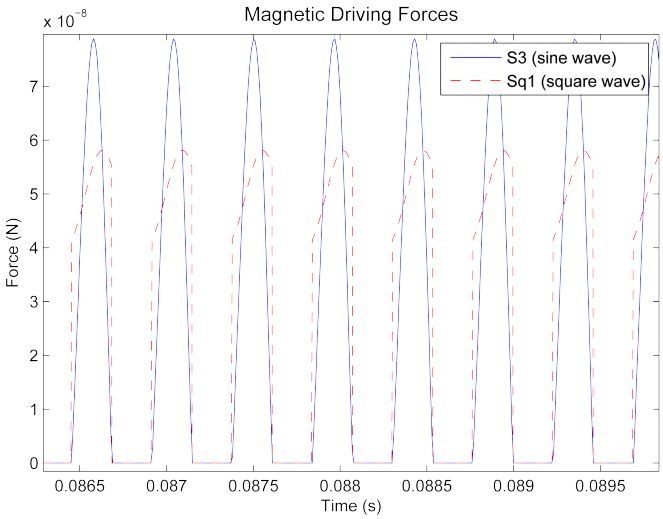

Figure 40: Plot of the simulated magnetic forces between the magnetic bodies with S3 (positive values of a sine wave only) and Sq1 (50% duty-cycle square wave) driving waveforms. The effect of the time- and position-dependent forces is clearly visible in the Sq1 plot. Impact did not occur during this simulation.

be developed. Of the actuators and methods of rectification that were presented in Chapter 1, several of them lend themselves to easy WRMMA integration. They are briefly reviewed in the following paragraphs with suggestions for adapting them for use with the new actuator.

The vibration-driven vibromotor presented by Saitou et al. and shown in Figure 3 is an excellent example of a mechanical rectification method that could be driven by wireless resonant actuators. The bent-spring vibration-driven impacting actuators

could easily be modified to incorporate magnetic bodies on their heads that interact with each other across the slider or with other bodies mounted behind them. The rectified motion could be used to drive a microslider back and forth for fine positioning or assembly, as was suggested by the authors. If the material of the parts was chosen to be non-magnetic, the parts would be unaffected by the external driving energy, unlike the authors' experiences with vibration-based power.

The rotary actuator described by Tabib-Azar and shown in Figure 16 would also be a prime candidate for a wireless resonant magnetic drive. By replacing the proposed thermal or electrostatic actuators with a single WRMMA body pair, which are mounted on flexible beams as shown in Figure 41, or with multiple WRMMA actuators on opposing sides of the rotor, a wireless rotary motor could be made. Such motors could have a variety of uses. Objects to be rotated could be attached directly to the motor or driven by an incorporated gear train or mechanical linkage.

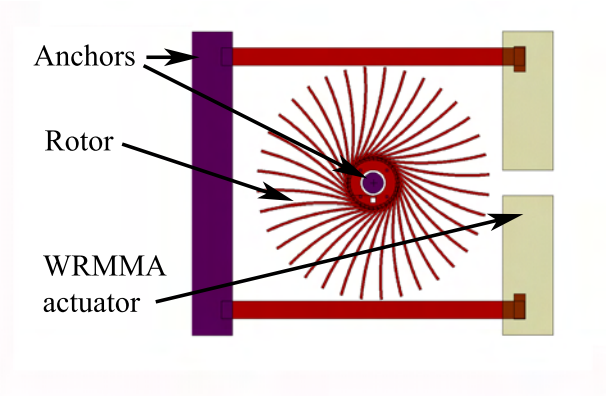

Figure 41: Linear to rotary converter powered by a swinging arm pushing against the ends of flexible fingers.

In many macro systems that operate on flat surfaces, impact actuators or stick-slip-type motions are used to provide long-range travel. In general, these require precise knowledge, control and repeatability of the frictional forces between the device and the substrate. Some rectification methods utilize asymmetries in friction or force to move devices on a surface. Stick-slip actuators utilize the differences between static and dynamic friction. In work by Liu and Wang, the momentum of a piezo-mounted body is combined with an asymmetric sawtooth actuation signal to cause a macro-

scale platform to jump across a surface with high resolution steps at a high frequency [32]. A similar idea is presented by Mita et al. in their paper on a micromachined, impact-driven microactuator that could move itself across a surface by overcoming static friction with the impact force of a moving body. Both of these methods rely on the production of asymmetric forces to overcome friction. In a situation where friction coefficients and surface properties are well defined, this approach works quite well. Another method is to operate devices on a specially designed surface where attractive forces can be controlled at will. Such a surface was presented by Donald et al. [15] and provides a simple method of producing easily controlled frictional forces with interdigitated buried electrodes, charge separation in conductive bodies and subsequent electrostatic attraction. In this way, normal forces and thus friction can be adjusted and controlled by voltages applied across the electrodes.

Early prototypes for WRMMAs investigated the creation of both rotary and linear actuators. Rotary systems were based on the design shown in Figure 41. Linear systems were based on the use of frictional fingers on bodies that fit in a trench. The fingers contacted the trench walls at an angle and thus slid more easily in one direction than the other. Impact energy from a WRMMA was intended to drive the device forward while increased frictional forces from the fingers prevented backwards motion. Generating repeatable friction forces between the fingers and walls was found to be extremely difficult due to fabrication variations.

4.7 WRMMAs for Microrobot Propulsion

4.7.1 RoboCup 2007: Nanogram

In the fall of 2006, an opportunity presented itself in the form of the RoboCup 2007 Nanogram Demonstration Competition. To qualify for the league, the robotic platforms had to fit inside a $300 \times 300\ \mu m^2$ box and operate without wires or tethers. The competition consisted of three tasks shown in Figure 42, that were to be performed on a $2.5 \times 2.5\ mm^2$ field. The task consisted of a straight line sprint, a slalom and manipulation of microfabricated disks into a goal. The tasks had to be performed autonomously under the direction of external computers with video feedback and vision tracking. The league is based on the actuation method presented by Donald et al.

[15], and buried interdigitated electrodes are provided in the field. Upon announcement of the competition in mid-2006, it was decided that the Institute of Robotics and Intelligent Systems at ETH Zurich would field a team.

In addition to sending a team to the 2007 RoboCup competition, the competition also become the focus the capstone mechatronics laboratory course offered by the group. The class historically consisted of competitions between multidisiplinary student teams with wheeled robotic platforms programmed by the teams and carrying equipment and actuators designed by students to complete specific tasks. The Nanogram competition presented an opportunity to shift the focus of the class from large mechatronics projects, which were maintained, developed and used only for the course, to a microrobotic system closely aligned with group research and interest. The course gives students the opportunity to work on projects that are on the cutting edge of microrobotics research and to develop real-world research skills in a multidisiplinary team environment, motivated by the competitive aspect of the class.

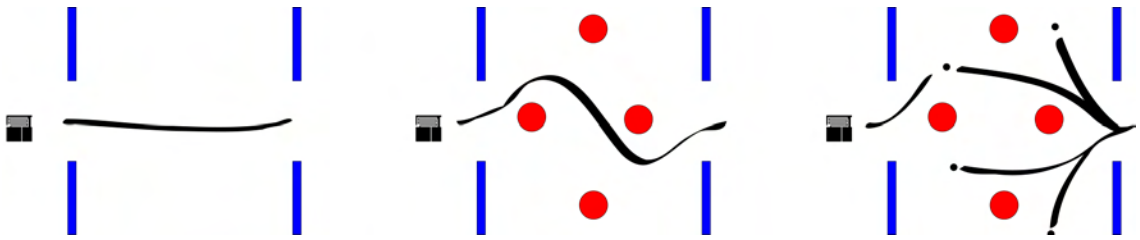

Figure 42: The Nanogram competition consisted of three tasks: (a) a sprint from one side of the field to the other, (b) a slalom from one side of the field to the other, and (c) manipulating balls (thin disks) into the opponent's goal. The field measured 2.5×2.5 mm^2 and balls measured 50 to 100 μm in diameter.

At the beginning of the class, the students are presented with a working microrobot prototype and the electronics necessary for its operation. The students then design and model their own robots based on the given fabrication restrictions. After several design reviews, the students create the mask files to be used in fabrication. Meanwhile, other team members are exploring and learning the control software, implementing tracking and control algorithms, and writing software packages and plugins to work with the supplied low-level software. After the microfabrication masks are ready, students assist with the fabrication process to produce their robots. The students

are always given the option of using the prototype robots and are encouraged to be creative in their designs. After fabrication of the robots, the teams spend their time perfecting their handling and control of the robots before the class competition. In 2007, the winning student team competed in the Nanogram competition at RoboCup in Atlanta, Georgia and swept the competition consisting of four US and Canadian schools. They were the only team to complete all the tasks and were an order of magnitude faster than the nearest competitors.

4.7.2 Magmite Prototype Design

Before the class began, a multidisiplinary advisory team consisting of the author and two PhD students formed in the fall of 2006 to develop the microrobotic platform and associated hardware. After examination of possible actuation methods, WRMMAs were chosen to provide power and propulsion for a microrobotic platform named "Magmite." When working with a system of the size dictated by the Nanogram rules, behaviors and forces are well within the transition regime between the macro and micro worlds. Surface forces and interactions grow in importance, while volume based forces such as gravity or magnetics decrease. The main source of surface forces that affect the Magmite operation is surface tension from water films and van der Waals forces between flat mating surfaces. These forces are difficult to model and maintain for repeatable operation of an impact or stick-slip actuator. Fortunately, the embedded electrodes in the field can be used to to modulate the frictional forces and apply an extra degree of control. By clamping the Magmite robot to the field with an electrostatic potential, the clamping forces can be modulated with a phase-locked voltage signal to provide asymmetric frictional forces. This provides a higher degree of control and repeatability than relying on natural frictional forces. The phase offset and amplitude of the clamping signal can be arbitrarily set to maximize robot performance. In certain situations, the phase offset can be changed by π radians to drive the robots backward.

The microrobot platform was modeled in Comsol to determine the magnetic forces, torque, and spring constant, in addition to the natural resonant modes. As is the case with all microsystems, the fabrication process is a key component of the design phase and many iterations of the design took place before arriving at a prototype that fit

fabrication constraints. The prototype was designed and fabricated with processes commonly used at the ETH FIRST-CLA cleanrooms. The fabrication is described in the next chapter. In addition to the Magmite platform, multiple generations of electronics and control software were also developed by the team and are described in the experimental results chapter. Figure 43(a) shows a Comsol model of the final prototype design. The Magmite consists of three main parts–the magnetic bodies, a spring and a frame as shown in Figure 43(a) (b). The two magnetic bodies are constructed of nickel; one body is attached to the frame, which is fabricated from gold and and has dimples on the bottom side to limit stiction. The moving magnetic body is fabricated on the end of the spring, which is also made from gold, and is held $7\mu m$ above the substrate by the frame. Figure 44 shows how small a Magmite microrobot is by showing it on the lap of Lincoln's statue on the back of a US penny.

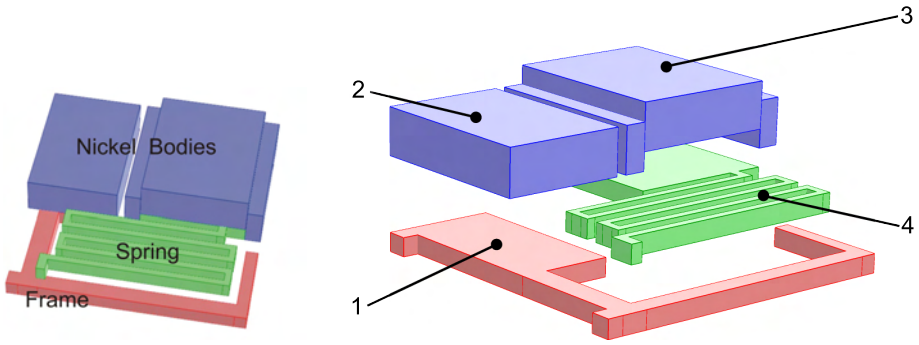

(a) Assembled view

(b) Exploded view showing (1) frame, (2) fixed body, (3) swinging body and (4) spring.

Figure 43: The final prototype Magmite design.

The asymmetric design was chosen because of size, design and fabrication constraints imposed on the prototype. To decrease the resonant frequency to levels that would be easily achievable, the spring was lengthened by adding several bends. This not only increased the area that must be dedicated to the spring, but also reduced the spring constant and the strength of the magnetic field needed to actuate the device. The length of the combined nickel bodies was made as long as possible to ensure adequate torque to turn the device with the applied magnetic field. The design was refined until simulations showed that the the rotational resonant mode shown in Fig-

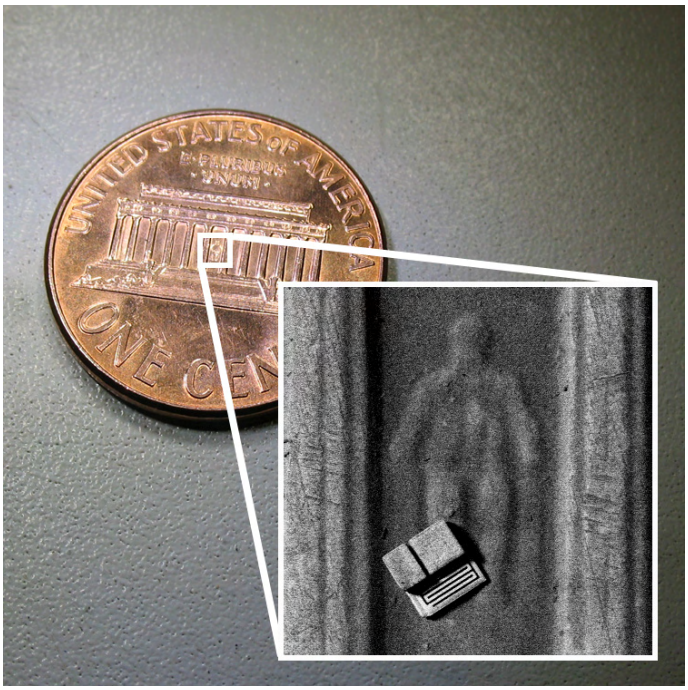

Figure 44: A US penny with an SEM image showing the Magmite microrobot on Lincoln's lap shows just how small 300 μm is (image courtesy of Bradley Kratochvil).

ure 45 was the first resonant frequency. Up and down, out of plane motion of the swing hammer, was identified as the second mode, and compression of the spring was the third. The thickness of the spring layer was increased to the maximum reliably achievable in fabrication, in attempt to increase the separation between the first and second modes. Despite the effort, resonance in the second mode was typically only 10 to 20% higher than the first mode depending on design specifics.

During operation, the microrobot is placed on a small die with buried interdigitated electrodes connected to a high-voltage amplifier that supplies a computer-controlled clamping signal to the electrodes. The die and robot are subjected to a uniform magnetic field of user-controlled direction. Upon application of the field, the magnetic bodies in the microrobot magnetize, causing it to rotate and align the bodies' combined long axes with the external field. The magnetization of the bodies also creates interbody magnetic forces, which deflect the spring and narrow the gap. When excited with an oscillating magnetic field of the correct frequency, the system

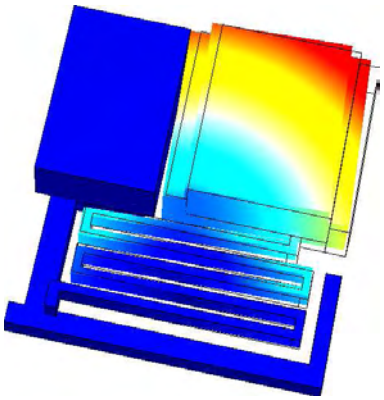

Figure 45: Simulation results showing the first resonant frequency, which is rotation of the moving body about a point near the spring/frame joint.

is driven to resonance, large amounts of energy are absorbed and impact occurs between the bodies. By combining this with a phase-offset clamping signal that releases immediately before impact, the microrobot can slide forward before clamping again when the next cycle starts. If the momentum of the swinging hammer alone is enough to break frictional forces, the device can be driven both forward and backward by simply adjusting the clamping phase.

Few details of the Magmite design and modeling are presented here because they were the results of a team effort between the members of the advisory team. Additionally, the nature of the system is simple enough that complicated modeling and optimization is unnecessary and often inaccurate due to fabrication issues discussed in the next chapter.

5 Magmite and Magnet Microfabrication

Magnetics and magnetic actuators are omnipresent in the world around us. With the exception of storage media, magnetics are not nearly as popular in microsystems. This is due to a number of things. In the world of traditional microfabrication, which gave birth to the field of MEMS, the prevalence of thin film and two-dimensional processing hinders the fabrication of thick layers necessary for large-volume micromagnets. Additionally, magnetic forces were often said to scale poorly when compared to other methods of actuation. This is only partly true, as closer analysis shows that scaling factors range from l^4 to l^2, depending on assumptions or implementation of the magnetic systems. In addition to volume-related challenges, fabrication methods for magnetic material are typically developed for materials and thin films commonly used in magnetic media. These methods do not address material issues and difficulties that arise when fabricating thick structures, and common materials are often not optimal choices for magnetic actuators.

As the field of MEMS has developed and matured in the last decades, unique fabrication methods and processes have developed with it to address the needs of micromechanical structures. Not content with the two-dimensional restrictions of traditional microfabrication processes, researchers commonly talk of 2.5-D processes where the extra half dimension comes from increased thickness of the layers and devices. Advances in photoresist technology now allow for deposition of lithographically defined patterns hundreds of μm thick. Deep-trench etching can etch narrow trenches through a wafer in a few hours. Advances in polymer processing allow for hot embossing of features of hundreds of μm thick, all the way down to nm in size. Other advances in electroplating, tape casting, screen printing and microassembly are leading the way to the integration of new materials into microfabrication processes.

This chapter covers the microfabrication of magnetic systems, focusing on the fabrication of the Magmite microrobot and the wafer-level integration of permanent magnetic material. Traditional microfabrication processes are typically divided into surface and bulk micromachining. During surface micromachining, layers of material are deposited and patterned on the surface of the wafer to build structures. Bulk micromachining relies on etching patterns into the substrate to form structures out

of the substrate material. Both of these approaches rely on the photolithography to pattern photosensitive material on the surface of the wafer that acts as masks, molds or sacrificial layers in subsequent etching, deposition or liftoff processes. Micromagnets are usually made using electroplating, screen printing, tape casting, spincoating, bulk etching or assembly. These processes offer different advantages in terms of size, accuracy, precision, strength, material, cost and repeatability. Systems requiring soft magnetic material are often electroplated because soft magnetic materials with favorable properties are typically quite easy to deposit. Permanent magnetic materials are much more difficult to form into micromagnets. Typical high-strength magnetic materials such as samarium cobalt (Sm-Co) and neodymium iron boron (NdFeB) are specialty products with complex fabrication processes that are not easily recreated in wafer-level processes. For these reasons bulk material is often deposited in wafer-level processes to form magnetic composites on the wafer. The second part of this chapter presents research on wafer-level integration of NdFeB magnets. The next sections present the fabrication of the Magmite microrobot.

5.0.3 Photolithographic Molds for Magnetic Material

Early investigations into microfabricated micromagnetic systems typically involved LIGA (Lithographie, Galvanoformung and Abformung) type processing based on the use of high-energy synchrotron x-ray radiation to expose thick film photoresist. It was developed in the early 1980s in Germany as a low-cost microfabrication technique applicable to a wide variety of materials [5]. The late H. Guckel was a legend in the field and instrumental the mainstream acceptance of the technology and its application to magnetic systems in the United States. In a typical process, thick photoresist patterns were filled with a variety of electroplated metals. Nickel electroplating was often used to form individual parts or nickel molds for subsequent embossing procedures (see Madou [33] for a more in-depth description). The widespread adoption of LIGA processing was hampered by the cost of the synchrotron exposure and the thick x-ray blocking masks. While its acceptance was limited, it did present a method for the generation of thick microparts if suitable photoresist could be found. This was done in 1987 when IBM filed a patent on the use of photoinitiators in epoxy resins, and SU-8 as a UV-sensitive photo-imageable spin-on polymer was developed (see Madou

pp 35–37 [33]). Modern mixtures of SU-8 sold by Microchem provide thicknesses well over 100 μm in a single spin application with near vertical sidewalls, are optically transparent, are chemically and temperature stable and can be exposed with standard photolithography equipment. Unfortunately, SU-8's chemical stability is also its biggest drawback for forming micromolds–it is extremely difficult to remove from the wafer surface after crosslinking. With the success and limitations of SU-8 in mind, other thick film spin-on resists were developed and several products have been introduced in recent years, such as KMRP 1000 and Futurrex 20000P, which are strippable and allow single spin coatings over 100 μm thick. With the availability of thick spin on resists, high-volume electroplated deposits of magnetic material can be made in wafer-level processes with standard cleanroom equipment. Determining the material with which to fill the molds is an open-ended question. Soft magnetic materials are relatively simple to deposit with electrodeposition. Hard magnetic materials are much more difficult and are discussed at the end of this chapter.

5.0.4 Early Experiences

The design and fabrication method chosen for the Magmite was based on previous designs of and attempts at fabricating WRMMA actuators. Initial efforts attempted to use the mechanical properties of SU-8 to form the spring between the magnetic bodies. SU-8 also formed "friction fingers" to allow the actuator to crawl in a narrow trench. The angled friction fingers contacting vertical sidewalls provided asymmetric friction, allowing the robot body to slide forward but not backward during impact. It was found that, during processing, the crosslinked SU-8 of the fingers and spring caused unexposed photoresist in subsequent lithography steps to crosslink and encase the SU-8 in a shell of resist that could not be developed away. The thin conformal coating of resist prevented the nickel layers from encasing the SU-8 to provide a strong mechanical fit needed to hold the fingers and spring. The unwanted crosslinking was attributed to the leaching of the photoinduced acid from the SU-8 into the surrounding resist during processing. The best results were achieved when the SU-8 was covered in a thin sputtered titanium layer in attempt to form a diffusion barrier between the two materials, but even these results were poor and this method of embedding the spring anchors and fingers was abandoned. Additionally, experiments on friction and spring

forces with SU-8 found that the mechanical properties of the polymer were extremely sensitive to small processing variations and residual stress caused cracks to develop in the springs. Attempts at using SU-8 polymer layers as structural members were abandoned in favor of using a gold due to the uniformity of its deposition in thick layers, the ability to use copper as a sacrificial layer with both gold and nickel, and the availability of thick, repeatable deposits with uniform properties achievable with a gold-plating bath. Further experiments with gold springs led to the change of spring design from two face-to-face leaf springs in a pocket between the magnetic bodies (magnetic bodies are shown in Figure 23), to a spring beside a swinging magnetic body which produced higher magnetic forces (see Figure 28) and lower spring constants.

5.1 Magmite Fabrication Process

The Magmite microrobots for the Nanogram competition were fabricated with a surface micromachining process and thick photoresists and electroplating. Figure 46 illustrates the process. A short description is given below, and a step-by-step description is given in the Appendix. Figure 46 (a) shows a top-down view of the Magmite robot with the frame and spring in gold and the gray nickel bodies. The line A-A* represents the cross-section for the rest of the illustrations. The first step (46b) is the creation of dimple holes in the wafer. The dimples lift the body of the robot off the substrate and reduce stiction. Robots without dimples stick to the substrate and do not move. After etching the dimples, the wafer is cleaned and coated with a titanium/copper/titanium seed layer before spinning photoresist to form the copper islands that elevate the swinging part of the robot, as shown in 46c. The titanium overcoat improves photolithography results and is etched immediately before copper plating. After copper electroplating (46d), the resist and remaining titanium overcoat are stripped and a second titanium overcoat is deposited to improve the adhesion and performance of the photoresist defining the gold springs and frame (46e), which is applied next. After gold plating (46f), the nickel-defining resist is applied (46g) and the nickel bodies are plated (46h). The device is released into solution (46i) with a selective copper etch. Although gold is soft and ductile, it was chosen for the spring material due to the ease of fabrication, the availability of a compatible Cu-selective

etch, the uniformity of its coverage and most importantly its nonmagnetic properties. If a magnetic material were to be used as a spring to connect the two magnetic bodies, it would form a magnetic circuit that would rob the gap between the two bodies of magnetic field strength and force. Nickel was chosen for the magnetic bodies due to its ease of deposition. Using material with higher susceptibility produces increases in interbody forces; this is currently under development and should be tested in the next fabrication run.

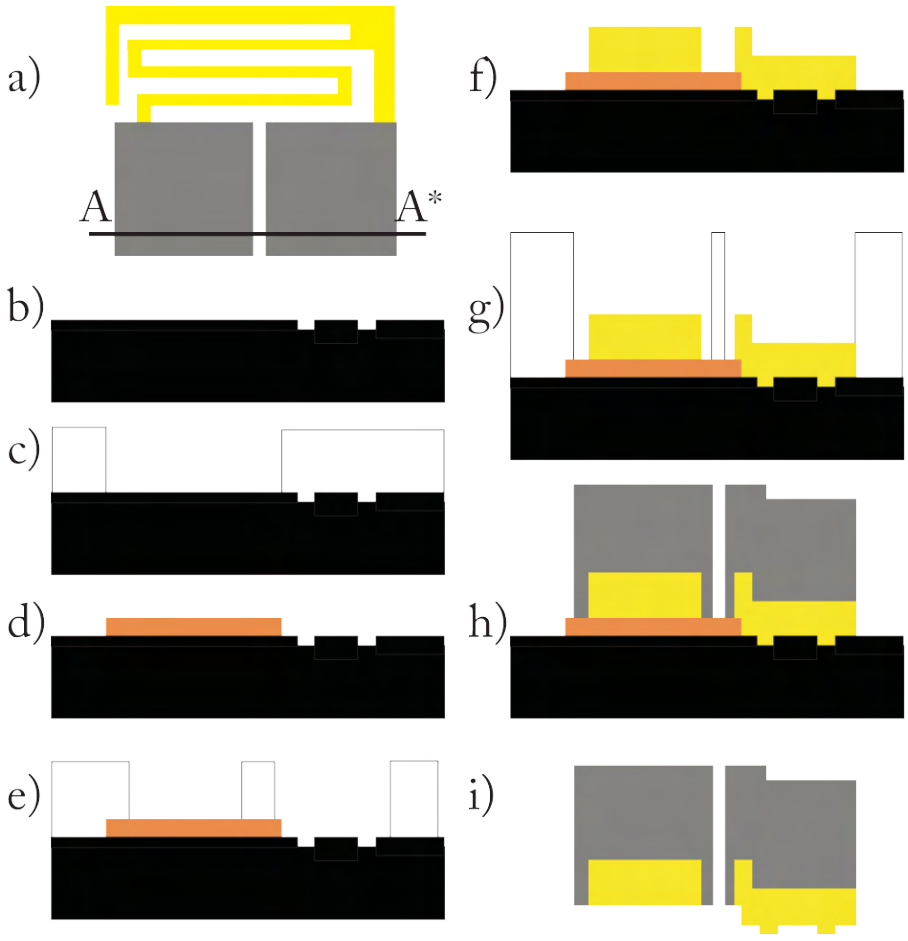

Figure 46: Magmite fabrication process with steps (a) through (f) described in the text.

5.1.1 Field Fabrication

The Magmite robots are driven on a specially prepared substrate with embedded interdigitated electrodes. A fabrication process for the field is also detailed in the Appendix. In brief, an oxidized silicon wafer is covered with aluminum, which is patterned and etched to form the electrodes. The wafer is then covered with a 1 μm thick layer of PECVD deposited Silicon dioxide, which is patterned with bonding pads. Maze walls, Nanogram regulation fields and obstacles can then be fabricated on top of the field with SU-8. The fields are then diced, mounted and wire bonded in open-face packages for use in specially designed printed circuit boards with appropriate connectors for the electrostatic clamping signal. The active field area with interdigitated electrodes was approximately 1 cm^2. Two different electrode patterns were fabricated. The first consisted of straight electrodes stretching across the whole field. The second consisted of zigzag lines. In both cases, the pitch and separation distance were 15 and 3 μm, respectively. Although extensive servoed parameter analysis has not yet been performed, there is no noticeable difference between the two field types in terms of robot performance.

5.2 Fabrication Results

Processing thick spin-on photoresist is quite different and more challenging than processing thinner layers commonly used for traditional thin MEMS devices. Increased thicknesses lead to greater effects from sidewall angles, lower resolution, larger variation in designed dimensions, increased layer stress and decreases in repeatability. Futurrex 20000P was used in Magmite fabrication due to familiarity with the product and relative ease of processing and removal. Serial processing of multiple wafers with thick Futurrex resist was typically met with poor results due to extreme variations in rest times between process steps. Required exposure times were typically three to five times longer than recommended by the manufacturer and approached 15 minutes for 90 μm thick layers. Combined with bake times of five to 10 minutes and five-minute cooling times, processing a single wafer could stretch to 45 minutes. Fortunately it was possible to overlap the processing of multiple wafers such that each wafer underwent the proper process; this greatly accelerated the throughput.

Many photoresists exhibit poor results when attempting to process directly on copper layers; this was also the case with the Futurrex resist. Typical problems are lack of adhesion and undercutting of the resist around developed areas. In this case, processing was further complicated by large variations in resist thickness as it was spun over copper and gold features over 35 μm thick. Profolometer measurement of photoresist topography typically showed a bump of approximately 5 μm when covering a feature of 40μm after the application of a 90 μm thick layer. As a result, resist covering the structure was only 60% as thick as the rest of the wafer and even thinner near the structure edges. The practical implication of this is that during development, large voids on top of the structures would develop more quickly and begin to underetch as the developer attacked the wafer-resist interface. Additionally, due to the large aspect ratio, the trenches that form the spring would develop slower due to the decreased diffusion of resist-saturated developer out of the trench. A major process improvement that significantly increased device yield was the inclusion of a thin titanium layer to cover copper layers before the next photolithography step. Immediately before plating, the titanium layer was etched in an hydroflouric and ammonium-fluoride-based etch that did not attack the copper or penetrate to the underlying titanium adhesion layer.

Even with the the additional titanium layer, it was still common that the photoresist fingers separating the spring arms would underetch and allow the springs to grow together, as shown in Figure 47. The underetch was typically more severe at the gap between the frame and spring, or between the hammer platform and spring due to the faster developing of the large voids. To minimize this, these gaps were typically made a few μm wider than the gaps between the spring arms. Additionally, due to geometry and increased developer flow, the spring corners would typically develop faster than the long arms, which would lead to underplating between the ends of the springs and the frame. To minimize this, springs were designed to be 1 μm narrower around the corners than around the long narrow arm. This evened the development time and increased yield. There was no observable change in final spring thickness, as the small change in thickness was beyond the resolution of the thick resist. Development was done with frequent inspections under a microscope to determine the end point. Variations in development across the wafer led to a typical loss of about 20%

of the devices due to over- and under-developing of particular spots across the wafer. Uniformity of the gold features and fidelity to the designed dimensions was another issue. Figure 47 shows spring widths that are 10 to 35% wider than designed. After this was discovered, later devices were designed with 7 μm wide springs with the expectation that they would widen during fabrication. Additionally, the changes in dimensions were not constant from the top to the bottom of the metal layer. Figure 48 shows the profile of the gold sidewalls.

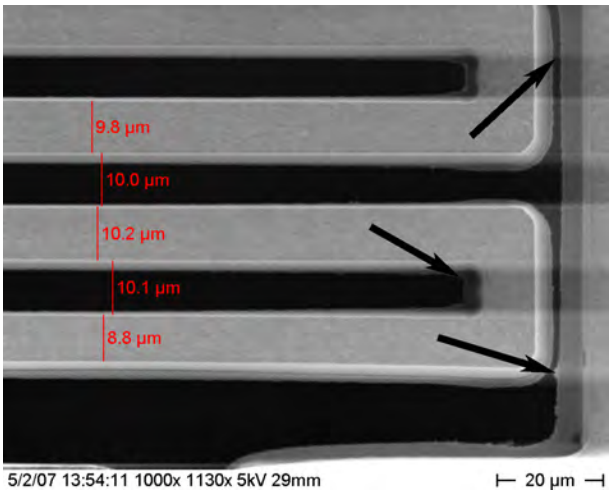

Figure 47: SEM image and measurement of spring width. Springs were designed to be 8 μm wide with 12 μm gaps. Arrows point to underplating of the gold between spring arms and the frame. In this situation, the springs remained separate and the device still functioned.

The nickel gap was another problem area that benefited from the copper-covering Ti layer. Initial gaps were designed to be 10 μm but it was found that after fabrication gap sizes typically measured 5 to 7 μm or had completely grown together. This had the effect of ruining many devices, while those that turned out often performed poorly due to the remnant magnetization (shown in Figure 29) that causes the bodies to latch together due to the small gap and weak spring forces. Steady hands and a careful eye were required to manually stretch the spring and increase the gap size to allow the devices to operate as intended. Increasing the designed gap to 20 μm greatly increased yield and improved performance. Additionally, further improvements were made by not fully developing the nickel-defining photoresist. The plating thief around

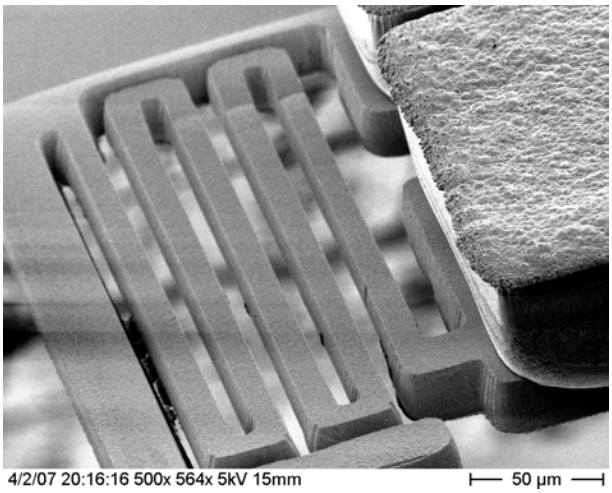

Figure 48: SEM image showing the slightly rounded profile of the gold springs in addition to the rounded corners of the nickel bodies. In this device, the nickel grew over the top of the mold.

the edge of the wafer was left spotted with a light film of resist while the nickel bodies were well formed. The thief was recreated with adhesive-backed copper tape during electroplating. Following these precautions, it was typically possible to get well formed nickel bodies, although in most devices the interface between the bodies was not well formed, and the nickel faces were rounded on the corners (see Figures 48 and 49). In situations where nickel bodies of widely varying size were on the same mask, large bodies would develop to the point of growing together long before the small bodies were developed enough to exposed the metal underneath them.

The additional titanium layer had a secondary advantage in that it increased the performance of the initial titanium adhesion layer. A processing run would typically take five to seven days. If it was interrupted and the wafers were allowed to age, they would typically suffer adhesion failure between the copper and Ti layers at some later stage. It was suspected that this was due to diffusion of oxygen or other gasses through the copper layer. It was found that adhesion failure could be avoided or lessened by covering the copper layer photoresist or titanium if processing needed to be interrupted.

The devices were fabricated on tethers connected to large bars of plated metal

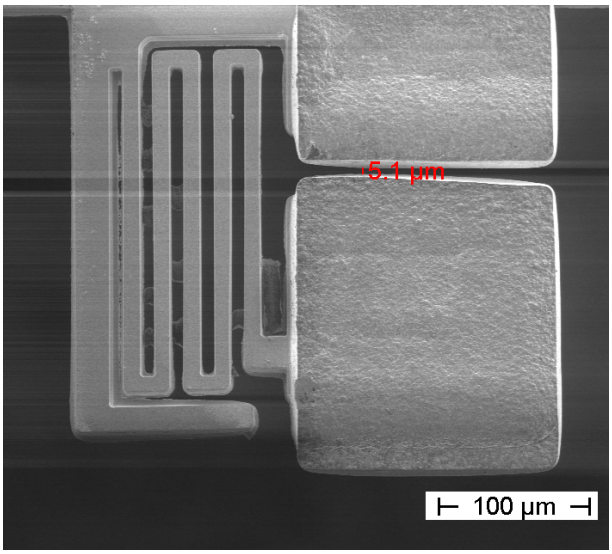

Figure 49: SEM image and measurement showing the slightly rounded faces between the nickel bodies. The gap size was designed to be 10 μm, but was 5.1 μm on this device.

that facilitate handling during release. Releasing was done with a solution of 10% ammonium peroxidisulfate by weight and deionized H_2O. This mixture is commonly used for its preferential etching of copper in the presence of nickel. For some undetermined reason, a small fraction of early release attempts suffered unexpected nickel etching. The nickel would show large pits and holes and eventually be reduced to a thin shell of metal with only the sidewalls and corners remaining. It was found that the addition of a small amount of ammonia (5 ml) to the etching solution would stop the nickel etch and accelerate the copper etch [35]. Typical etch times are in the range of one to two hours, but devices left in solution overnight suffer no harm.

The Magmite fabrication discussion points out the difficulties and hurdles of the thick-resist fabrication process. While the spring widths and hammer faces varied, the functional result was that optimum actuation frequencies for individual devices varied and was best determined individually. Regardless of the variations between devices, if the springs, dimples and gap between the bodies were well formed, the device would work on the field if the appropriate frequency could be found. Due to the variations in fabricated dimensions, little effort was made to match experimental

results with modeling after the initial design phase. Constants used in simulation are derived from best-guess estimates of hammer mass and from fitting simulation results to measured data.

The next section continues with wafer-level fabrication of screen printed permanent magnets and their comparison to published results of other integration methods.

5.3 Microfabrication of Permanent Magnets

While the advantages of magnetic actuation are well known, the development of efficient magnetic microactuators face many obstacles, including material limitations and lack of fabrication techniques. This section presents research on the wafer-level integration of screen-printed (NdFeB) magnets in a microfabricated electromagnetic actuator. It also compares the strengths of the screen-printed magnets to those presented in other works with different materials and fabrication methods. Many methods of using and generating magnetic fields and forces on a microscale have been demonstrated. They typically involve ferromagnetic or permanently magnetic material interacting with a magnetic field generated by an electromagnet. The materials and fields can interact with attractive-repulsive forces [9,10,27,50] described by Equations 3, 10 and 13, or torques can be generated as shape or material anisotropies, and magnetic orientations attempt to align with the applied fields as described by Equation 11 [25,43]. The actuator demonstrated here (see Figure 50) is used in an attractive-repulsive mode with the magnet fabricated on a cantilever above a planer coil.

5.3.1 Cantilever System Fabrication

The screen-printed magnets were fabricated using commercially available spherical magnetic powder with a mean diameter of 25 to 55 μm (Magnequench MQP-S-9-8). The bulk powder has an intrinsic coercivity (H_{ci}) of 6.40 to 7.60 kA/m (8.0 to 9.5 kOe) and a residual induction (B_r) of 0.68 to 0.72 T (6.8 to 7.2 kG), as shown in Figure 51. Maximum operating and processing temperatures are 150° to 170° C and 300° C, respectively. Full magnetization of the magnets requires a 2.5 T field. For screen printing, the powder was mixed with a variety of binding agents to determine

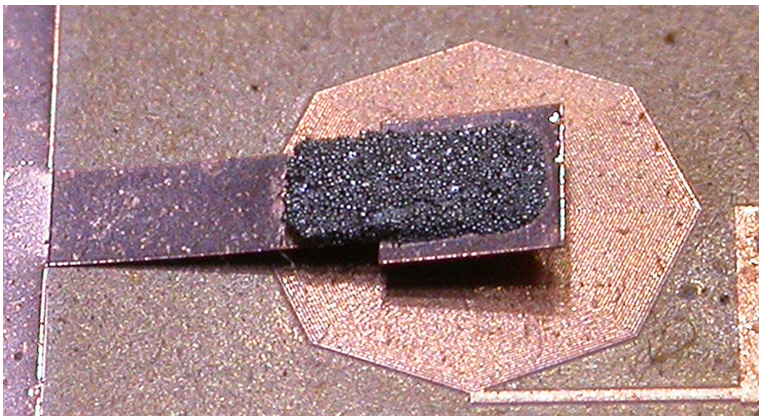

Figure 50: Screen-printed magnet (1000×2000×100 μm) on a copper cantilever above a planer coil.

their compatibility with printing and microfabrication processes. Polyimide (HD Microsystems Pryalin PI2560), two-part epoxy and a polymeric resin were used. A pre-mixed polymeric resin-solvent paste was supplied by DuPont iTechnologies and consisted of 82% magnetic powder, 15.5% solvent and 2.5% organic binder by weight [41]. The epoxy was mixed with 88% powder by weight, while the polyimide was mixed with 86% powder by weight.

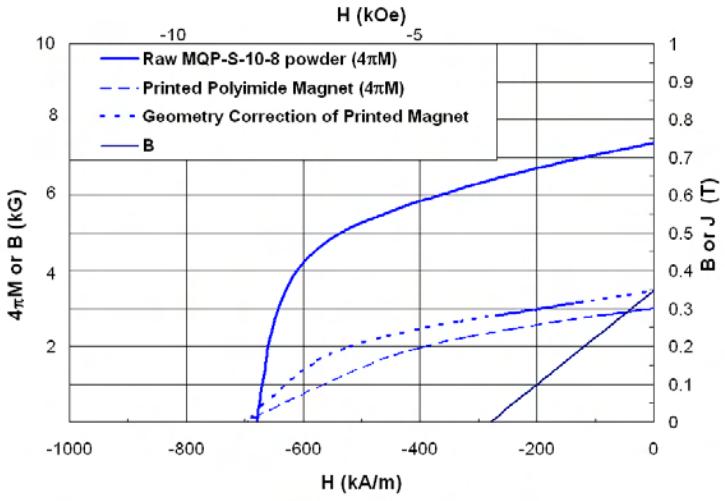

Figure 51: Demagnetization curves of printed polyimide magnets and raw powder.

Neither the polyimide or epoxy pastes were optimized for thick-film printing–they were simply prepared until the visual consistency matched that of the DuPont paste. Typical screen-printing pastes, including the DuPont sample, exhibit a reduction in viscosity during times of high shear, meaning they are pseudo-plastic in nature, allowing the paste to flow easily through the screen as it is printed. After the shear stops, viscosity increases due to thixotropy, and the paste holds its shape. Polyimide and epoxy pastes mixed in the lab did not appear to exhibit this behavior, although no viscosity or rheology measurements were made.

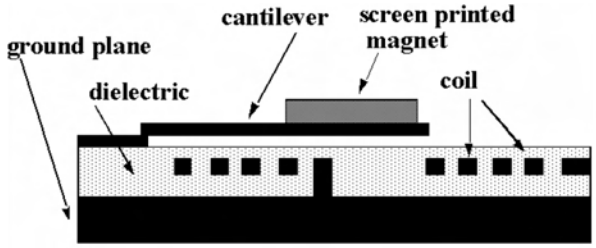

Figure 52: Cross-sectional view of the magnetically activated cantilever.

The magnetic microdevice was surface micromachined using electroplated copper and gold (see Figure 52). A 20 nm titanium adhesion layer and 400 nm of copper ground plane were sputter deposited on a blank wafer. A 5 μm layer of photo-imageable cyclotene (BCB) was spun, patterned, developed and cured with via holes to connect the inner loop of the coil to the ground plane. A Ti/Cu seed layer 20 nm and 40 nm thick, respectively) was sputtered on the BCB. The coil was patterned in 2.5 μm thick photo resist and formed with 4.5 μm thick electroplated copper. Each coil had 40 turns with resistance ranging from 20 to 100 Ohm depending on thickness and wire width. After removing the seed layer, the coil was covered with BCB to insulate it from the cantilever. A hard-baked sacrificial photo resist was patterned with cantilever anchor points and covered with a sputtered seed layer. The cantilevers were defined with resist and plated with either gold (4.5 μm thick) or copper (10 μm thick) after which the cantilever-defining resist and seed layer were removed. The magnetic paste was prepared by mixing measured amounts of powder and carrier until the paste had a consistency similar to that of the DuPont paste. A 150 μm thick stainless steel stencil was used to print the magnets. They were cured at 150°

C for two hours before being magnetized in the out-of-plane direction in a 2 T field. The spherical NdFeB powder is isotropic so there is no need to pole it during the curing process. Polyimide-based magnets were found to be the most compatible with the heated solvent release and thus were used on all devices. The more robust copper cantilevers could be dried on either a 125° C hotplate after a methanol rinse, or in a liquid CO_2 critical point dryer. Some of the gold cantilevers were bent by turbulence in the dryer before it was discovered that stacking a dummy wafer over the samples reduced the turbulence and prevented the cantilevers from being bent.

5.4 Screen-Printed Magnet Results

The solvent-based paste supplied by DuPont iTechnologies, produced the most uniform magnets with both screen and stencil printing. They were the strongest and had the straightest sidewalls and best uniformity of the pastes tested. Unfortunately, the magnets were not compatible with subsequent processing as they dissolved easily in acetone and other solvents. Because of this, polyimide magnets were used in fabricated devices. Polyimide and epoxy magnets were weaker than the DuPont magnets. Reflow after printing and during curing made it difficult to determine the volume and magnetic properties of the epoxy and polyimide paste difficult. The B_r values measured with a super-conducting vibrating sample magnometer in the perpendicular direction were 2,850 G, 3,000 G and 3,250 G for epoxy, polyimide and the DuPont binder, respectively. Demagnetization correction of the perpendicular measurements based on magnet geometry adjusted the data to closely match the long axis measurements, which were 3,500 G for the polyimide magnets (see Figure 51). The intrinsic coercivity (H_{ci}) was 8,050 Oe (644 kA/m) and the coercivity (H_c) was 3,500 Oe (280 kA/m). Table 4 compares these results with other reported results of magnet integration using a variety of materials and methods. The intrinsic coercivity and residual induction are the largest reported for non-assembly processes. The NdFeB material is comparable in strength to SmCo magnets.

Cantilever deflection was measured by the depth of focus method on an optical microscope with a motorized sample stage. The stage had a 0.04 μm resolution with a 1.5 μm resolution in optically determining the focal plane. Magnetic and deflection

forces were measured with the same motorized stage and a microbalance with a 0.001 g (9.81 μ/N) resolution.

The magnets demonstrated both attractive and repulsive forces, as shown in Figure 53. Internal stresses raised the Cu beam in Figure 50 approximately 600 μm above the surface after release. In the region of small deflections of ± 50 mA, the deflection rate was nearly linear at 1.1 $\mu m/mA$, as shown in Figure 53. The stiffness of the cantilever was measured to be 0.81 $\mu N/\mu m$. Combining the experimental results gives a force generation of 0.89 $\mu N/mA$ when the magnet is 600 μm from the coil. The nonlinear deflection on the right side of Figure 53 is due to the increasing magnetic force as the magnet approaches the center of the coil. Plastic deformation was negligible and the cantilever returned to within 4 μm of its initial position after current was removed.

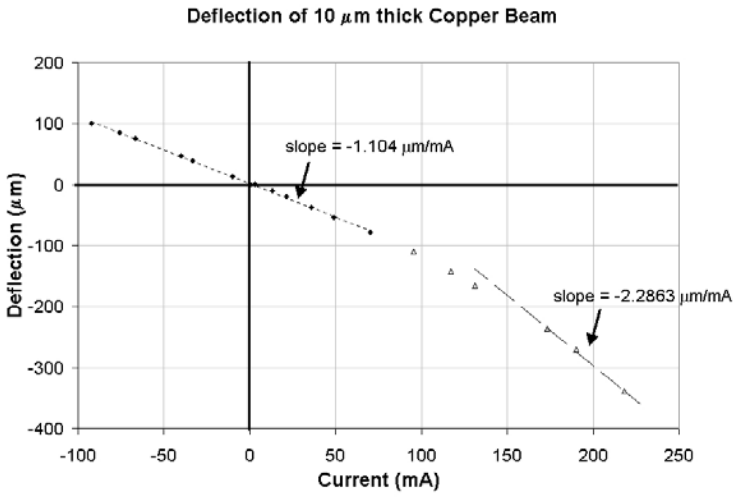

Figure 53: Deflection of a 10 μm thick Cu cantilever.

Compared with the Cu beams, deflection of the thinner gold beams was more dramatic with total deflections well over 1,000 μm (Figures 54 and 55). The cantilever deflected linearly with current for approximately 200 μm with a slope of 1.84 $\mu m/mA$, before nonlinearity in the field gradient appeared and snapdown occurred. As current decreased, the cantilever returned to a position lower than the initial position due to plastic deformation.

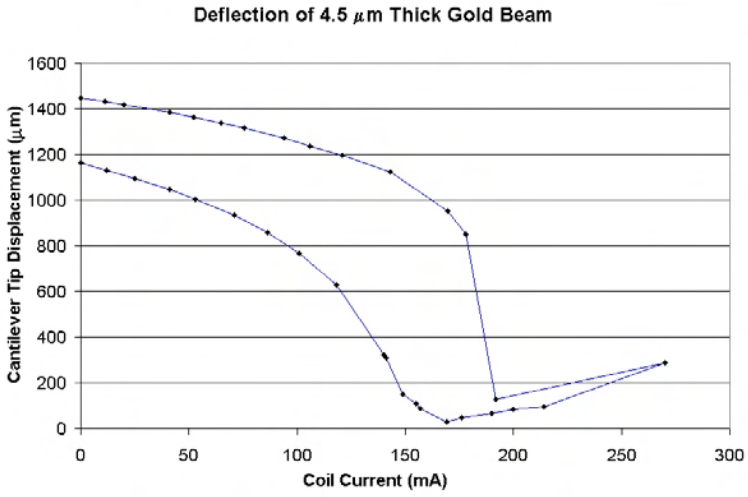

Figure 54: Deflection of a 4 μm thick Au cantilever.

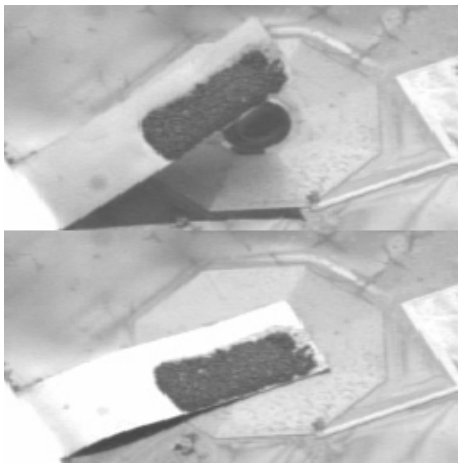

Figure 55: 4 μm thick Au cantilever in deflected and undeflected states.

5.5 Permanent Magnet Comparison

Several researchers have demonstrated the deposition and use of polymer composite magnets [10, 16, 26, 27] with thicknesses ranging from tens of μm to near 100 μm (see Table 4), but few have stressed the importance of magnet volume or attempted to increase magnet thickness past 100 μm. In this work, magnets with thicknesses of up to 200 μm were printed in a wafer-level process. In addition to volume limita-

tions, material limitations are another obstacle to efficient magnetic microactuation. Most microfabricated magnetic films have low coercivity and retentivity, which limits the forces and efficiency of the systems. By incorporating commercially available high-strength rare-earth NdFeB powder with large coercivity and retentivity values, magnets that are significantly stronger than ferrite powders and similar in strength to the difficult-to-prepare Sm_2Co_{17} powders are possible. Hard magnetic materials have been integrated into devices in a variety of ways, including sputtering, thermal evaporation, assembly, electroplating, screen printing, spin coating and molding. Each method offers advantages and disadvantages. Assembly of small magnets into microsystems has been demonstrated by many researchers [23, 43, 48, 50] and incorporates the strongest magnets of any available integration methods (see Table 4). This assembly is typically done on a device level and is considered a relatively costly and time-consuming process. Electroplating, screen printing, spin coating and in situ molding are other methods being investigated for wafer-level deposition of permanent magnets. Electroplating is often used by the magnetic memory industry. Soft magnetic materials are used in read-write heads, while hard magnetic materials are used as the magnetic medium where the digital bits are stored. The thicknesses of the films are limited by internal stresses, while material limitations produce low H_c and B_r values [9, 25, 43, 51]. Recent work has demonstrated the formation of magnetic composite electroplated films with increased coercivity and retentivity based on the codeposition of electroplated films with embedded magnetic particles, offering improvements over standard electroplating [21]. Screen printing, spin coating and molding produce magnets with strengths typically between that of electroplating and assembly with wafer-level processes. Polymer magnets offer a unique combination of high-strength magnets, wafer-level processing, versatile fabrication methods and economical manufacturing.

Table 4: Comparison of magnetic integration methods, materials and strengths.

Author	**Method**	**Material**	**Dimensions** (μm)	$\mathbf{H_{ci}}$ **(Oe)**	$\mathbf{B_r}$ **(G)**	$\mathbf{BH_{max}}$**(MGOe)**
B. Vikramaditya et al. [48]	Automated assembly	NdFeB bonded magnet	550×220×220		6,000	
H.J. Cho, C.H. Ahn [9]	Electroplating	CoNiMnP	40×40×50	800-1,300	2,000-3,000	1.75
B. M. Dutoit, et al. [16]	Spin coating	Sm_2Co_{17} powder	1,250×1,250×35	7,000	3,400	2.8
H.J. Cho, C.H. Ahn [10]	Photoresist molds	Strontium ferrite powder	50-200 diameter, 60-70 thick	4,480	330	0.34
S. Guan, et al. [22]	Composite electroplating	Nickel with ferrite	10 thick films	2,000 (Hc)	2,000	0.25
L.K Lagorce, M. G. Allen [27]	Screen printing, spin coating	Strontium ferrite powder	4 mm circle, 90 μm thick	3,975	2,800$\parallel$ 600$\perp$	1.5
K. Vollmers (this work) [49]	Screen printing	NdFeB	1,000×2,000×100	8,400	3,500$\parallel$ 3,000$\perp$	2.5

6 Experimental Results

This chapter covers the WRMMA and Magmite testing, along with explanations of the experimental setup, driving electronics and software. It also compares experimental and simulation results to determine unknown system parameters.

6.1 Magmite Experimental Setup

The experimental setup for driving the Magmites and testing the WRMMA actuator consists of a control computer, drive computer, custom-made electronics, a current source, a high-voltage amplifier, a coil setup and a camera for vision feedback. A schematic of the setup is shown in Figure 56 with arrows indicating the general flow of information. The electronics are the result of extensive effort by multiple members of the Magmite team and IRIS, staff and only a general overview is given unless the details have significant impact on other areas of interest.

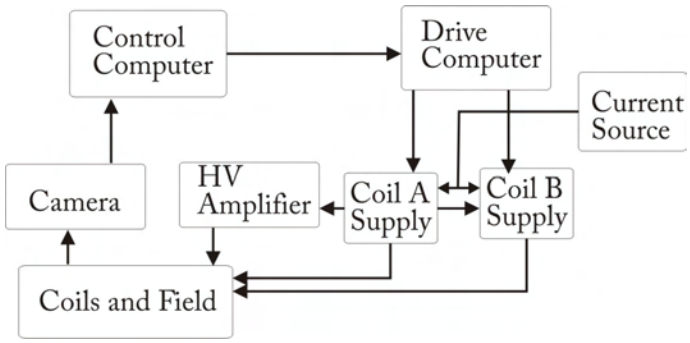

Figure 56: Sketch of the control system.

6.1.1 Electronics

The system was designed for the robot to operate autonomously as needed for the Nanogram competition. A FireWire video camera with a fixed-focus zoom lens and ring light was mounted above magnetic coils to provide video feedback of the robot during operation to the control computer. Software on the control computer tracks the robot position, compares it to the desired path, calculates the desired waveform

signals and sends the data to the drive computer, which in turn passes it to the custom electronics that are mounted on an integrated N-Bus. The electronics for each coil pair, called "coil supply" (see Figure 56), includes a field programable gate array (FPGA) and microprocessor that communicate with a current sensing board. The sensing board produces or receives a trigger signal to synchronize multiple channels depending on its configuration. The sensing boards also produce a synchronized 0 to 5 V clamping signal that is sent to a high-voltage amplifier with a 0 to 150 V range and a gain of 30. The third function of the sensing board is to control the coil current. An analog comparator circuit compares the output current of the H-bridge motor controller board to the internal value and commands the motor controller to increase or decrease the current as needed. The motor controllers both draw current from a single dual-output 30 V, 5 A power supply hooked in series. During the generation of 5 A, 2,500 Hz pulses in both sets of coils, the RMS current draw on the power supply is less than 1 A.

H-bridge motor controllers and a pulse-width modulated (PWM) type of control were chosen due to the inductive nature of the coils and the need to drive a high-frequency field. High voltages were needed to overcome the inductively produced voltages and ensure fast field changes. High currents were needed to produce large field strengths with low inductance coils using a minimal number of turns. PWM control was chosen because of the need for widely varying field frequencies; linear power amplifiers were thus unsuitable due to their power dissipation at low frequencies. To increase the frequencies and simplify the control electronics and FPGA programming, the coil currents were continually driven either up or down and were not allowed to decay naturally at any time.

6.1.2 Coils

The Magmite robots were operated in a uniform magnetic field between two orthogonal Helmholtz coil pairs as shown in Figure 57. The coils were designed with matched performance (field strength/input current) and minimized inductance while falling within the limits of the driving electronics and power supply. At the center of the coil pairs, 1 A of current produced 0.7 mT of field with field strength rising to 0.71 mT five mm from the center point along the coil axis. The coils were designed

to allow the PCB carrying the field to be inserted in the center, with fixtures holding the board flat and centered in the coils. The coil parameters are given in Table 5.

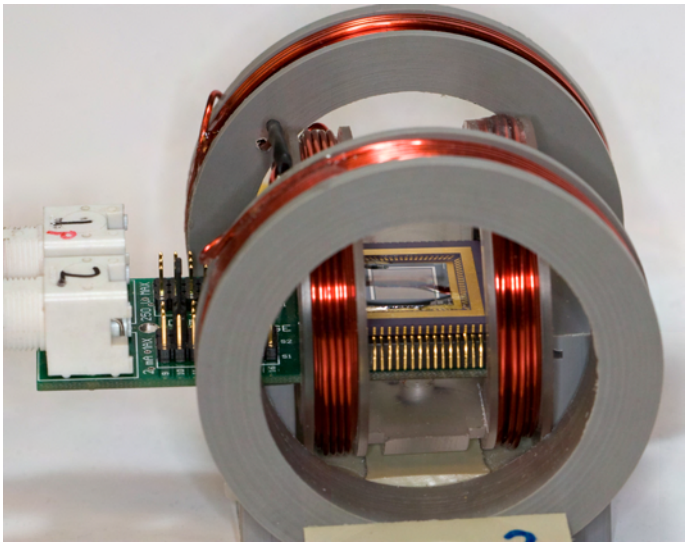

Figure 57: Coils used to actuate the Magmite microrobot with the PCB and field inserted.

Table 5: Coil parameters.

	Inner Coil	**Outer Coil**
Turns	24	42
Wire thickness	1.6 mm	1.6 mm
Calculated inductance per coil	34 μH	148 μH
Area of wire (w×h)	7.5×6 mm^2	10×7 mm^2
Separation (face to face)	25 mm	45 mm
Inner diameter	44 mm	60 mm

The inductance of the coils was calculated with the multilayer air core inductance formula given in Equation 27, where L is the inductance in μH, n the number of turns, r_i the inner radius, and w and h the width and height in meters of the cross-sectional

area of the wrapped wire:

$$L = \frac{31.6 * n^2 * r_i^2}{6 * r_i + 9 * w + 10 * h} \tag{27}$$

The inductance of the coil pair together is undoubtedly higher than that calculated by the above formula for a single coil, but it is expected to be accurate by better than a factor of three, which is approximately the inductance expected when arranging the two coils face to face and calculating them as one wider coil.

6.1.3 Field

The interdigitated electrode fields on which the robot drives are based on the ones described by Donald et al. [15]. Due to the high speed of the robot, the field area was increased to approximately 1 cm^2. The fields were mounted and wire bonded in open-faced packages, as shown in Figure 58. the packages were then mounted in testing sockets on custom made PCB boards with the appropriate connections for electrostatic clamping. During operation, the package was covered with a piece of glass to protect the field and robot from contamination. When the robot would become stuck to the field and undrivable, a small magnet was used to pull the robot to the glass and drop it back on the field.

6.1.4 Control Signal Properties

The method of generating the driving waveform is an important aspect of the system with practice impacts on system operation and performance. A single wavelength of the magnetic excitation signal is shown in Figure 59. A wavelength is defined with a length of T_{wave}, which is broken into n pieces, each Δt long in time. The transition from high to low magnetic field takes place at an integer multiple of n, as the duty cycle of the square wave is only adjustable by integer units of n, shown as x in Figure 59. Adjustment of the frequency of the excitation signal is performed by adjusting the value of Δt, which has a minimum resolution of approximately a single ns. This means that a small change in Δt will make an n larger change in T_{wave}. If n is set at its maximum value of 100, there are significant jumps in T_{wave}

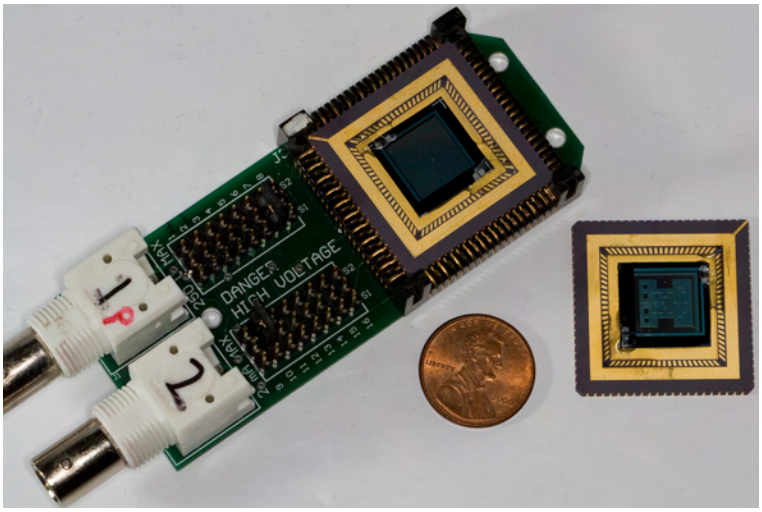

Figure 58: Packaged interdigitated electrode field and PCB with US penny for scale. The field on the right has an SU-8 maze fabricated on the surface.

and the excitation frequency. A large n also means there many possible values for the duty cycle and other other adjustable parameters that will be described shortly. If n is set to a small value, e.g, two, the minimum step in frequency in the 2 to 3 kHz range is approximately 1.7 Hz. The minimum frequency step size is not constant and increases with the excitation frequency. The choice of n depends on the needs of the user and other system parameters. Low n values are important for vibrometer analysis, which is described later in this chapter. In addition to frequency adjustments of the driving signals, the high and low values of the waveforms are also adjustable. Typical current values of the magnetic signal are 0 A (or a slightly negative value to reduce the remnant magnetization) to a high value ranging between 3 and 10 A with a 50% duty cycle.

The waveform shown in Figure 59 is an idealized sketch of the actual waveform. Figure 60 shows traces of the actual current passing through the coils. Measurements with high-bandwidth Hall sensors confirmed that the magnetic field matches the current traces in shape and phase, and thus the currents levels are often used rather than magnetic field strength in the following discussion. Figure 60 (a) shows the waveform at a moderate frequency where ramp times are becoming a significant fraction of the total waveform. Closer inspection of the waveform shows the high-frequency noise

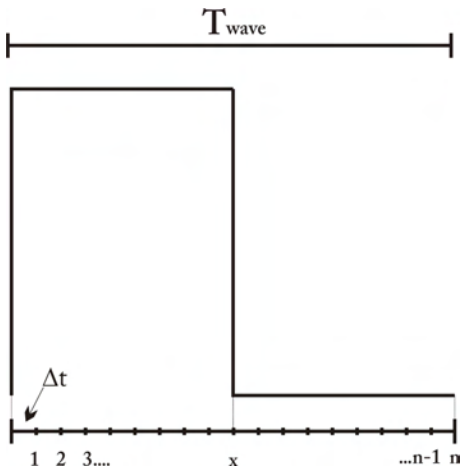

Figure 59: Sketch of a single wavelength of the idealized magnetic field.

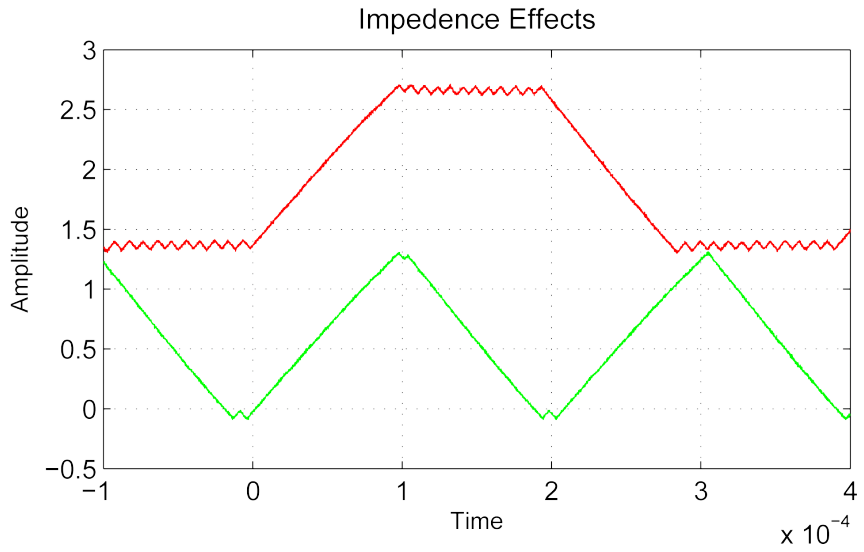

Figure 60: Plot of the coil current at two different frequencies with current pulses of the same amplitude. (a) At low frequencies, a trapezoidal wave is formed, (b) while at higher frequencies the flat areas disappear and the wave becomes triangular. The sawtooth pattern in the constant value areas of the waveforms are artifacts of the PWM-style current control. Their frequency depends on the speed of the comparator electronics and their amplitude depends on the driving voltage and inductance.

from the sample frequency of the analog comparator system. Figure 60 (b) shows the effects of a higher excitation frequency. Here, the flat areas of the waveform have

nearly disappeared and signal bounces between the high and low values. The rate of current change (slope) in the system is directly proportional to the voltage of the current supply, and inversely proportional to the inductance of the coils. At higher frequencies or higher current pulses, the flat-topped trapezoidal waveform becomes triangular and begins to attenuate, as the current does not have enough time to reach the set value. In an effort to make the waveforms from both coil pairs match, the inner coils were driven with either a separate current supply at a lower voltage or with only one side of a dual output supply arranged in series. The effects of the different shaped waveforms or power supply voltages on robot performance were not investigated.

The magnetic control signal is synchronized with an electrostatic clamping signal, as shown in Figure 61. The phase between the two signals can be adjusted by $p \times \Delta t$, where p is an integer. The duty cycle of the electrostatic wave is also adjusted by multiples of Δt with the variable y in the figure. The period is the same as the magnetic signal. Similar to the magnetic signal, the high and low values can be adjusted independently with typical high values of 2 to 4 V, which corresponds to 60 to 120 V from the HV amplifier.

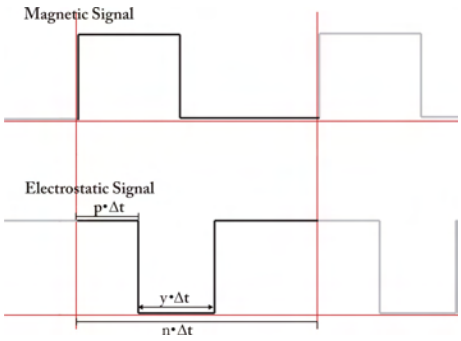

Figure 61: Synchronized magnetic and electrostatic control signals.

Figure 62 shows the synchronizing, electrostatic and clamping signals together as captured from the system. The inductive effects on the magnetic signal are much more subtle at typical Magmite operating parameters than Figure 60 implies. In this example, the clamping phase is set to zero and duty cycles are 50%. Notice the arrangement between the three signals: The upward transition of the magnetic

field begins at the start of the waveform, while the downward transition starts at the 50% mark. As long as the wave does not become triangular and begin to attenuate, the area under the curve remains constant. Assuming the magnetic forces are linear with field strength, as simulations and measurements have shown, then the magnetic work injected into the system remains constant even though details in the waveform change. It is important to note that this does not imply that the energy absorbed by the system remains constant under such changes.

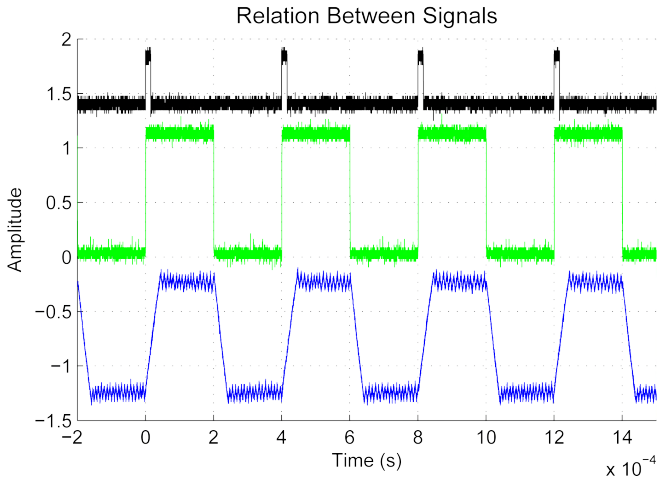

Figure 62: Magmite signals with no phase offset; (a) synchronizing signal, (b) electrostatic clamping signal and (c) magnetic signal.

The velocity of the Magmite is adjusted by changing the number of electrostatic clamping waveforms sent over a set period of time, as shown in Figure 63 where the robot is allowed to move only when the clamping signal is low. By reducing the fraction of the time that the system is allowed to slide over the surface, the effective velocity is reduced.

Figure 63: Velocity control applied to the electrostatic clamping signal.

In addition to velocity control, the forward/backward direction of the robot can

be controlled by shifting the phase of the clamping signal by π radians as shown in Figure 64. Clamping occurs when the c_2 traces are high, and magnetic forces are applied when the c_3 traces are high. The plots in Figure 64 are representative phase relationships that were found to drive most robots. A phase offset of approximately 1.05 radians would drive the robots backward while 4.2 radians would drive them forward. The effect on robot performance of the firmware-derived spike in the clamping voltage of Figure 64 (b) was not investigated.

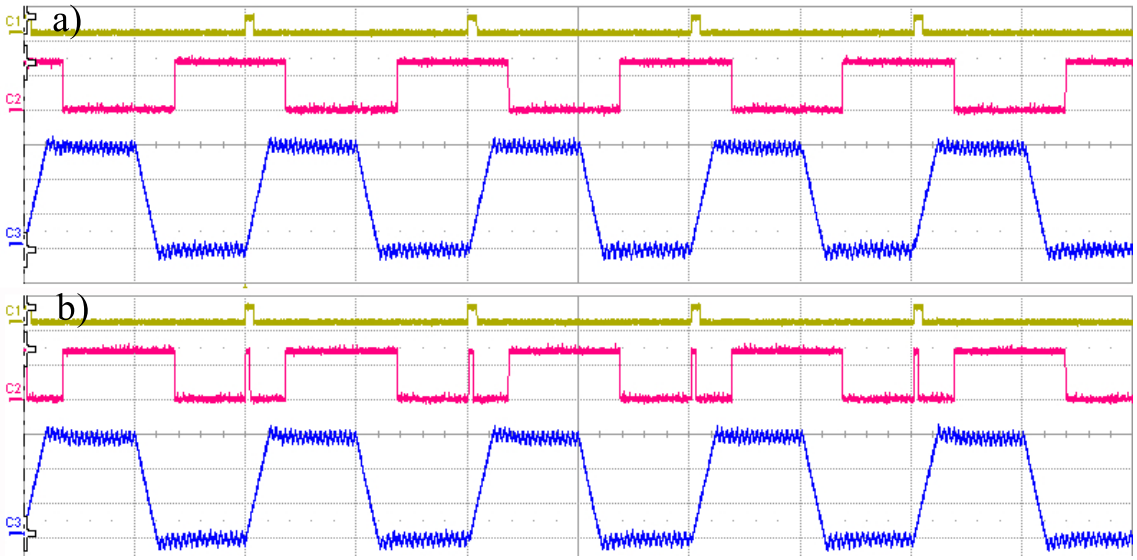

Figure 64: (a) Forward and (b) backward driving signals where c_1 is the synchronizing signal, c_2 is the clamping signal and c_3 is the magnetic signal. The clamping trace when moving backward ((b)-c_2) also contains a firmware programming error that caused an unwanted spike in the clamping at the beginning of each waveform.

The creation of the waveforms detailed in Figures 59 to 63 is done by the control software, which is described in the next section. The direction of the robot is controlled adjusting the ratio of the currents sent to the two coil pairs. The resulting superposition of the two individual fields causes the robot to rotate and align its long axis with the field. During constant operation of the robot with no changes in parameters, the outgoing waveform runs through 100 cycles before beginning again. When parameters must be changed, the outgoing waveform is stopped regardless of phase and the new waveform starts with an initial phase of zero. This is an important

point to consider when attempting to simulate the system. The phase of the driving signal is broken every time the signal is updated, while the phase of the WRMMA must be physically preserved. Additionally, the software is only capable of generating square waves and comparison of different driving signals in experimental data is not possible.

6.1.5 Software

The control software was written by Magmite team members and adapted from other projects in the IRIS group. Figure 65 shows a screen shot of the software with a robot on a field in the video display. The software is modular in design and is used in several projects for microrobot control, vision tracking, image processing and other robotic tasks. While used on the Magmite project, a module for manual control of the robot was developed along with modules for loading and executing parameter sweep scripts, visual tracking of the robot during operation and very recently visual servoing and multiagent control through time and frequency multiplexing, which are not in the scope of this thesis. The software can also capture and save video data or load saved video images for reanalysis. While software performance is dependent on computer speed, it routinely tracks the robots in real time at 60 Hz, or one frame every 17 mS. The maximum observed speed of the Magmite robot to date is 1.25 cm/s, which leads to a displacement of $\tilde{2}00$ μm per frame. Efforts are underway to increase the frame rate, tracking performance and control algorithms to the camera limited 100 Hz.

6.1.6 Variable Sweeps

An important function of the software is the loading and execution of sweeping scripts for the analysis of the WRMMA. A sample script is shown in Figure 66. The starting point of the sweep is set along with the step size. The number of steps, the step time, a pre- and post-scan pause and an inter-step pause can also be set. Due to hardware and firmware resolutions and limitations, numerical values set here are not necessarily achievable. In the case of the frequency, the value is rounded to the nearest possible value, while in the case of other variables, the value is rounded down. Care must

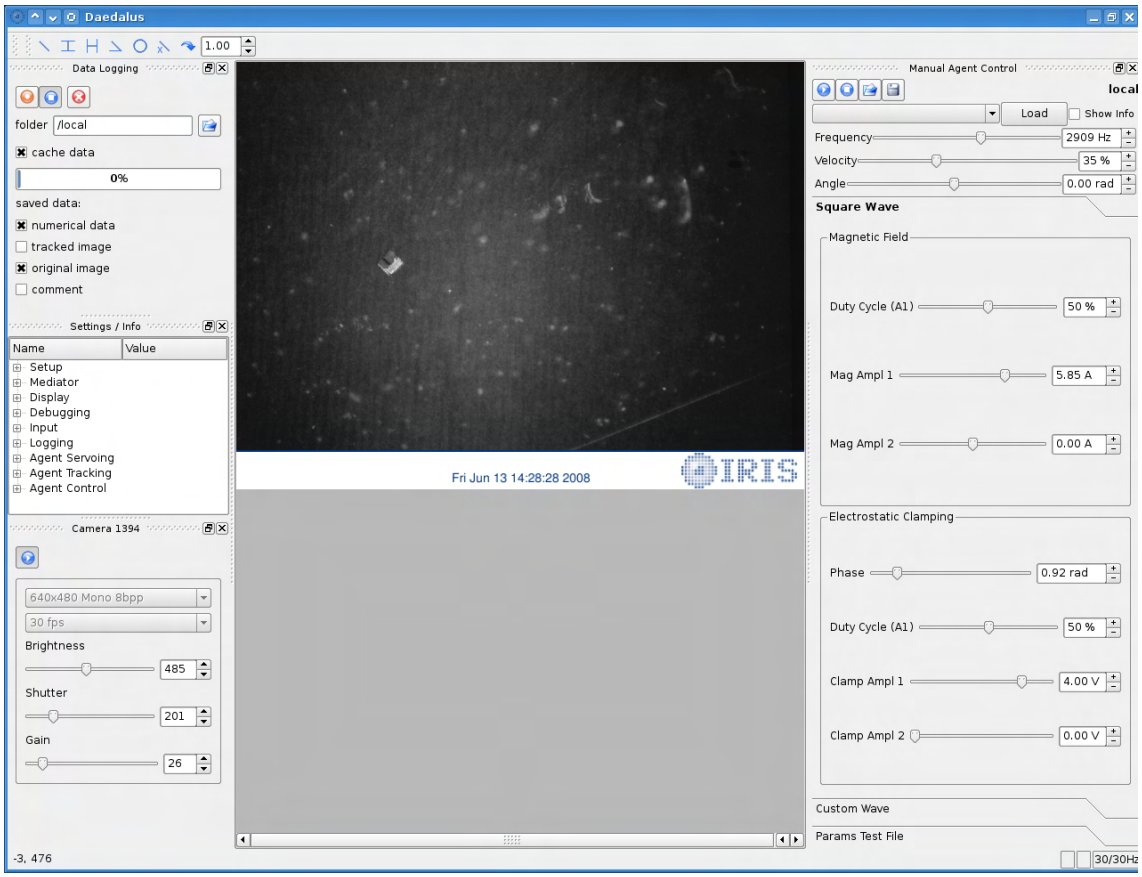

Figure 65: Screen shot of the control software. Adjustable parameters are sorted and grouped according to use under various tabs.

be taken to understand the limits of the software and hardware, their impact on the measurement results and how to configure the system to achieve the desired results. Sweep scripts were used extensively in the laser vibrometer analysis that is discussed shortly.

6.1.7 Experimental Descriptions

The results presented in this chapter focus on the WRMMA performance and characterization as derived from laser vibrometer measurement, surface friction measurement and a few driving experiments in addition to comparison to simulation results.

Understanding the behavior of the WRMMA actuator is critical to its development

```
<?xml version="1.0" standalone="no" ?>
<nanogram>
  <test type="square">
      <frequency start="2300" step="1" />
      <velocity start="100" step="0" />
      <field_angle start="0" step="0" />
      <mag_duration start="50" step="0" />
      <mag_current_1 start="1.6" step="0" />
      <mag_current_2 start="0.0" step="0" />
      <elec_phase start="4.07" step="0" />
      <elec_duration start="50" step="0" />
      <elec_amplitude_1 start="0.0" step="0.0" />
      <elec_amplitude_2 start="0" step="0" />
      <motor pos="0" step="0" />
      <dead_time start="0" step="0" stop="30"/>
      <steps count="200" time="400e-3"/>
  </test>
<!--  <test type="custom">
    <waveform filename="test_waveform.dat" />
    <frequency start="2000" step="0" />
    <velocity start="1.0" step="0" />
    <dead_time start="500e-3" stop="500e-3"/>
    <steps count="10" time="100e-3"/>
  </test>-->
</nanogram>
```

Figure 66: Screen shot of a variable sweep script. In this example, the frequency is being swept from 2300 Hz to 2500 Hz in steps of 1 Hz with 400 ms between steps. There is no initial or inter-step pause, but there is a post scan pause of 30 ms.

and adaptation. The laser vibrometer is an important component in the analysis and understanding of the actuator. A laser vibrometer can measure the velocity of a moving surface with a high degree of accuracy and bandwidth. Operating similarly to doppler radar, the laser light reflected off a surface is recombined with a reference signal and pulsations in the interference pattern are measured to determine the speed of the object in the direction parallel to the beam. Raw data from a vibrometer typically consists of velocity as a function of time with a user-selected sample rate and scan time. This data can be analyzed in a number of ways to reveal details about the operation and behavior of a system. Three distinct types of vibrometer measurement were performed on the actuator powering the Magmite robots. The first type of measurement was an automatic fast fourier transform of the data collected from a frequency sweep. The second type of measurement was the collection and analysis of raw data during steady state operation at the peak actuation frequency. This data was used to analyze system energy and impact forces. The third type of measurement was analysis of the dynamic rise and decay times from periotic pulses,

which reveal information about the rate of energy uptake and damping. The results of these measurements can then be used to develop and validate the Simulink system model.

6.2 Laser Vibrometer Analysis

Measurements were taken with a microscope-based Polytec vibrometer mounted on a probe station. The sensing laser passed through the camera-equipped microscope head and could be automatically positioned anywhere in the field of view by steering mirrors within the head. Magnification and beam size are adjusted by internal zoom or selecting an objective lens of different magnification. During measurements, the Magmite robots were mounted at the center of a Helmholtz coil pair with dimensions identical to the inner coil pair detailed in Table 5. The robots were mounted with their long axes parallel to the magnetic field, just as they would be when driving. The coils were driven with the standard drive electronics and the parameter-sweep software module. The coils were mounted such that they could be easily rotated to expose three sides of the swinging hammer to the laser. The robots were mounted on removable posts with glass cover slips or specially constructed interdigitated fields to study the effects of electrostatic clamping. Methods for mounting robots included gluing them to the glass, pushing individual robots against the vertical edge of a piece of double-stick tape or mounting a tether full of robots on the edge of a piece of double-stick tape with the robots suspended in air above the surface. While pushing individual robots into the tape made it possible to mount them on specially wired playing fields, it was difficult to recover the robots for later driving analysis; thus few measurement were made. Additionally, the nickel sidewall angle would often cause the robots to tip so the back or side of a robot would be lifted off the substrate, thereby making it difficult to take accurate measurements of electrostatic excitation of the resonating bodies. Gluing was also extremely difficult and was quickly abandoned in favor of analyzing a full string of robots mounted on tape.

6.2.1 FFT Analysis

The first types of measurements made were frequency sweeps in order to create frequency response plots of the resonating devices. In typical situations, these would be performed by exciting the system with a "chirp" signal, which contains a wide range of excitation signals. This was not done in this work because the Magmite driving electronics would not allow such a form of excitation. Additionally, measurements that reflect the steady state magnitude of the oscillations at different frequencies and current amplitudes is more useful than simply identifying the resonant frequencies. The vibrometer was run in a repeating loop with a peak hold function recording the maximum response in all channels while the excitation signal was stepped through a range of actuation frequencies. This allowed the system to reach steady state behavior at each excitation frequency while combining all the FFT scan results into a single plot. Figure 67 shows the FFT output for excitation at three distinct frequencies. By sweeping the excitation through all frequencies, the peak responses were collected to show the full spectrum response.

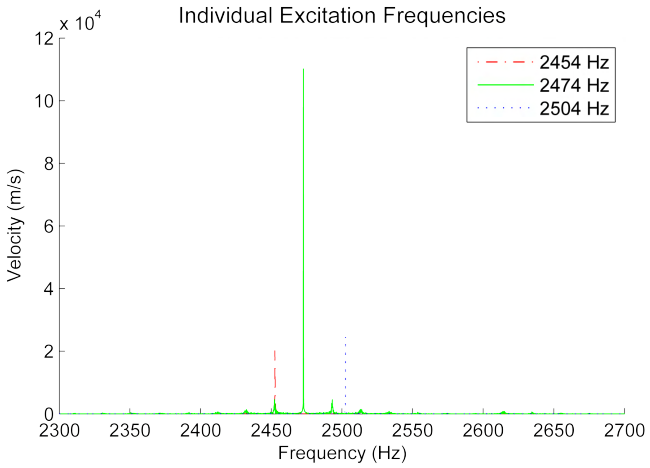

Figure 67: Raw FFT data from the vibrometer showing the excitation at three different frequencies.

The dwell time at each step was dictated by the single scan time of the vibrometer which was a function of scan range and resolution. Typical measurements were from 0 to 10,000 Hz with 12,000 line resolution scans that took 1.3 seconds to complete. Due

to the frequency resolution of the excitation system, the minimum frequency step of 1.2 Hz was clearly visible in the vibrometer FFT data (shown in Figure 68) where the jagged blue line is the original data and the green line is an envelope function applied in MATLAB. There is concern that due to the actuator's sensitivity to the excitation signal, the peak amplitude is most likely not the true maximum. This should not be an issue when operating a device because the response peak broadens during impact, but it may influence the comparison between measured and modeled data.

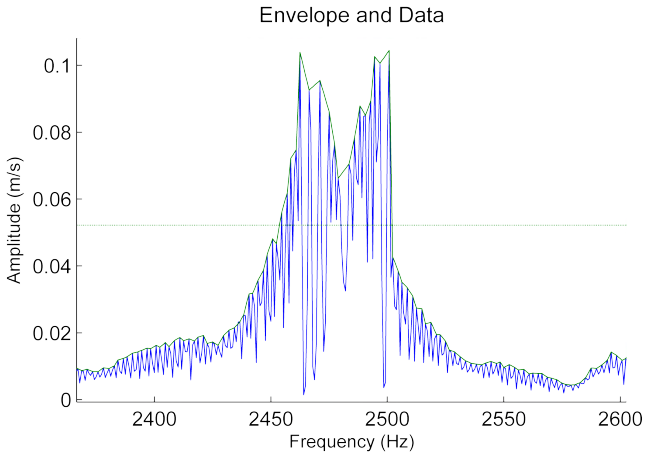

Figure 68: Raw FFT data from the vibrometer showing the steps in the excitation frequency and a MATLAB-applied envelope used to smooth the data.

Figure 69 shows data from a typical scan where the device was excited from 2,300 to 2,700 Hz with high resolution excitation and 12,000 line FFT analysis. To help ensure that sampling occurred during excitation, the excitation step time was set slightly longer than the FFT scan time. High resolution excitation scans were typically limited to a narrow region of interest that was identified with a much faster and wider low-resolution scan.

Figure 70 shows the FFT of a typical actuator in response to increasing the driving field. As the driving field strength increases from 1 to 5 A, or from 0.71 to 3.55 mT, the maximum velocity of the swinging hammer increases from 0.01 m/s to 0.10 m/s. Between 3 and 4 A the peak begins to plateau; further increases in excitation current only serve to increase peak width and decrease the Q factor. The Q factor based on full width at half-max measurements in this example drops from 148 to 43, with the

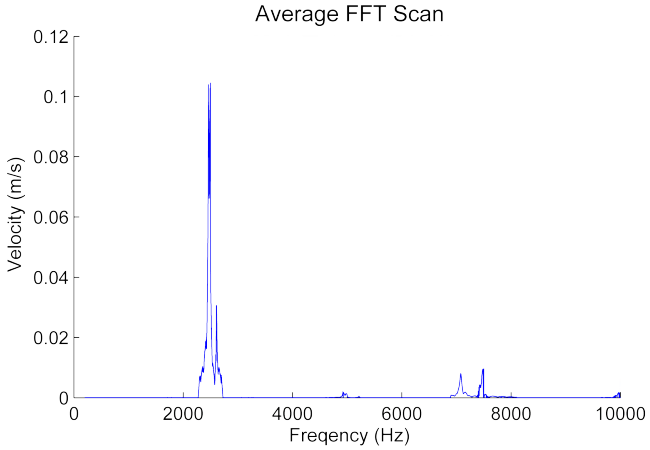

Figure 69: FFT data from 200 to 10,000 Hz with a 2,300 to 2,700 Hz excitation sweep.

biggest drop between 2.13 and 2.84 mT. This behavior is attributed to mechanical limiting of the oscillation amplitude due to impact between the magnetic bodies.

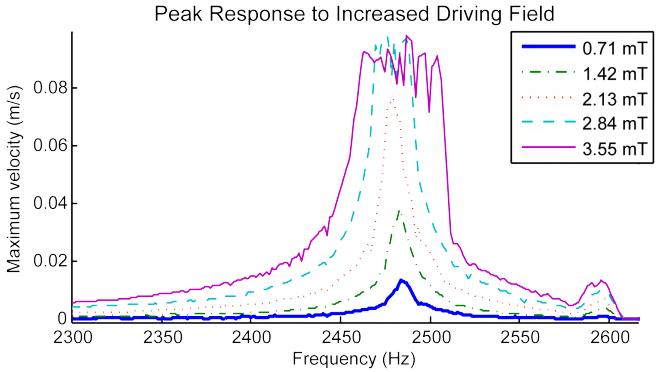

Figure 70: Typical device response to increasing driving field.

Analysis of 16 devices at 0.71 mT with the same designs showed a variation in responses due to fabrication differences between devices. The Q factor based on full width at half max was 152 with a standard deviation of 12. The driving resonant frequency was 2,470 Hz with a standard deviation of 75 Hz, and the maximum amplitude was 0.011 m/s with a standard deviation of 0.0061 m/s.

6.2.2 Motion Reconstruction in 1-D and 3-D

In addition to providing information about the frequency response, the FFT data can be combined with phase data comparing the motion of the hammer to the excitation signal. In this work the synchronizing signal shown in Figure 62 was used as the reference signal by the vibrometer. This allowed for the comparison of multiple physical scan points in both time and frequency. By programming the vibrometer to scan over a series of points, the 1-D motion of the individual points can be linked by the phase information to create an animation of the motion of the surface at all the frequencies scanned, as shown in Figure 71. It must be noted that the 1-D motion is captured along a specific line in space. Any topography on the surface of the hammer moving perpendicular to the line results in artifacts in the data, making it appear as if the solid metal hammer is flexing like a membrane when in reality variations in surface profiles cause the artifacts.

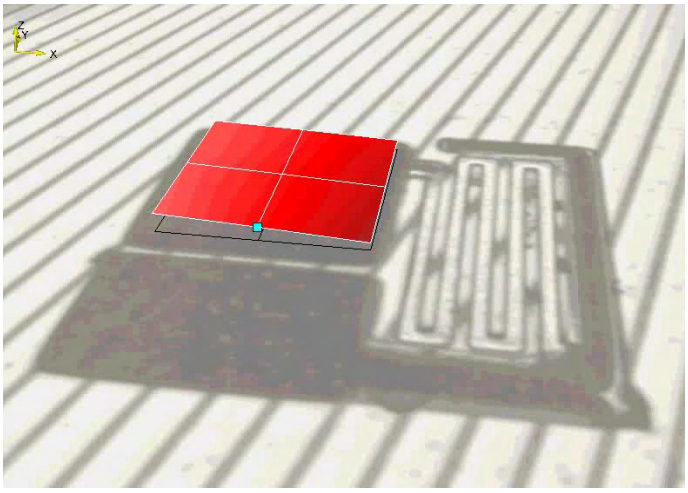

Figure 71: Still image from the vibrometer-produced video showing the motion of the swinging hammer in the out-of-plane direction.

By scanning the swinging hammer at multiple points on three orthogonal sides, the exported frequency, amplitude and phase data can be used to recreate the motion of the hammer, as shown in Figure 72. This allows for visual analysis of all 6 degrees of motion of the hammer at all frequencies included in the scan, and is extremely useful for visualizing the motion of rigid bodies.

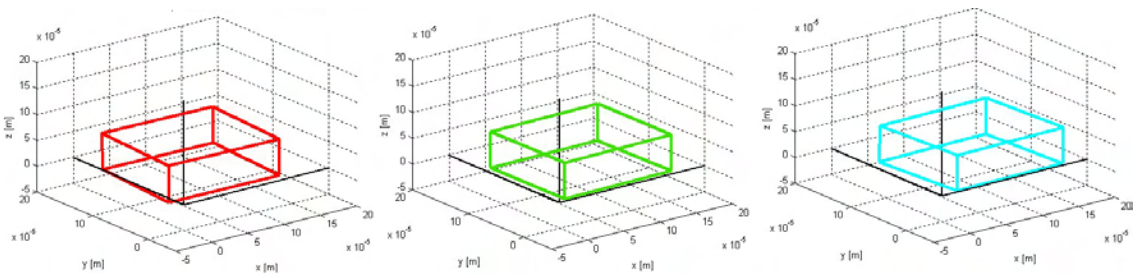

Figure 72: Still image from the MATLAB-produced video showing the 6 DOF motion of the swinging hammer reconstructed from orthogonal vibrometer scans.

6.2.3 Comparison of FFT Data to FEM Modeling

FFT data can also be compared to suggested frequencies from FEM modeling results. Comparison of measured values with models based on the designed dimensions show good relative agreement with the correct order of the resonant frequencies, but a general shift to higher resonant values was observed. This is attributed to variations in fabricated versus designed dimensions of the springs and to a lesser extent to reductions in swinging body mass to to rounded corners. Models based on measurements of actual spring and body dimensions determined from SEM images are much closer to the measured values but are time intensive in both measurement and modeling time. Due to these variations, resonant frequency modeling is an important part of the development of a design, but comparison of the fabricated and modeled devices has fewer useful results. In the microrobot application, the FFT data has been most useful in identifying resonant peaks at which the robot drives with the lowest excitation frequency.

6.2.4 Comparison of FFT Data and Simulations

Simulink-based simulations demonstrate the same growth and widening, of the resonant peak that is found in measurements as shown in Figure 70. The "jump" behavior, as reported by Lee and Pisano [29], was not observed in the FFT data. It is assumed this is a result of the stepped nature of the driving signal, as this behavior disappeared from simulations with any driving waveform other than continuous "chirps." Correlation of the FFT and simulation amplitude is of little use due to

energy leakage. Although a Hamming window was applied to the vibrometer samples prior to FFT analysis, it is unknown if the amplitudes were corrected by the software. Additionally, system damping has not yet been determined. It is important to note that simulations use idealized square waves to drive the system rather than the impedance-affected waveforms shown in Figure 60.

6.2.5 Linear or Torsional?

Up to this point, any analysis of vibrometer data is largely independent of system geometry. Before continuing, an assumption must be made about the basic nature of the system. Table 2 gives the equivalent variables for the analysis of a torsional resonant system following the method described in Chapter 4. The swing arm actuator shown in Figure 43(a) is a combination of torsional and linear systems. The hammer follows a curved path, as shown in Figures 72 and 73. Figure 45 shows that the displacement (and thus the velocity) is not constant throughout the body and in this way the system behaves like a torsional system. At the same time, it is also not a traditional torsional wire actuator, the angle of deflection is quite small and the swinging body rotates while translating on a curved path with varying radius due to bending of the spring. Determination of the swinging body's path and rotation would require FEA

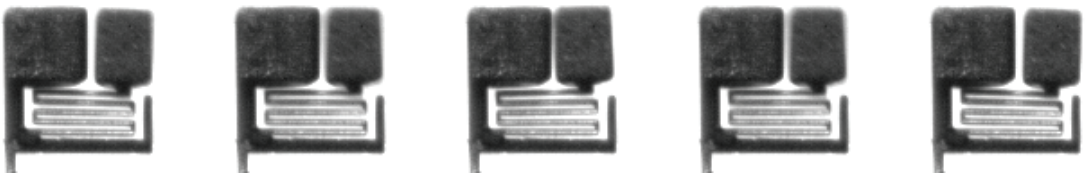

Figure 73: Still image from high-speed video of a resonating actuator.

analysis and the results would be subject to inaccuracies due to variations in spring dimensions. Also of consideration, and mentioned in the Appendix (see Figure 98), is the second-generation system made possible by the addition of a second sacrificial copper layer in the fabrication process. This allows for the fabrication of symmetric robots, which are better approximated as a linear system. Since these symmetric robots exhibit better driving characteristics, it is likely that the prototype will be the only asymmetric design. For these reasons–combined with the linear velocity data

from the vibrometer and the continued efforts to develop and analyze new symmetric designs with the methods developed in this thesis the following analysis assumes the system is a linear 1-D oscillator. To help ensure that the presented analysis is still accurate, velocity data is taken from a point on the robot body where the kinetic energy of the system is the same in both the linear and torsional systems. This point was approximately 20 μm from the rear outside corner of the swinging body, although during typical experiments, changes in reflectivity and surface topography limited the options for laser placement due to low signal strength.

6.2.6 Raw Scan Data Analysis

In addition to the FFT data, the raw velocity data from the vibrometer can also be saved for off-line analysis. The raw data files can be extremely large when sampling at 25.4 MHz and thus scan lengths are often limited to a few hundred milliseconds when capturing high-resolution slices of oscillator behavior. This data provides a valuable insight into the behavior of the oscillating hammer–analysis can determine oscillator energy and average impact forces that can be extracted from the actuator. Figure 74 shows a small piece of raw time scan data. Typical scan times were a few hundred ms. In the raw vibrometer data, negative velocities indicate that the hammer is moving away from the laser and the gap between the two bodies is decreasing.

Figure 74 clearly shows the periodic repeating behavior of the swinging hammer during low-amplitude oscillations. Closer inspection of the plot reveals high=frequency noise components in the signal, which are most visible in regions of near-uniform velocity at the peaks and troughs of the curve. The peaks and troughs occur when the hammer is moving through the region of zero spring deflection. FFT analysis of the data reveled that the high-frequency noise is relatively evenly distributed in a band of frequencies between 100 and 120 kHz. While this is similar to the high-speed switching frequency of the pulse-width modulation hardware, there is no sharp peak to indicate that this is the cause.

Figure 75 shows a compilation of averaged waveforms for scans of a device with stepped excitation currents from 1 to 12 A in 0.5 A steps, driven at resonant frequency. The first six lines (1 to 3.5 A) are sinusoidal in shape with minimum noise. From 4 to 12 A of excitation, an increasingly large number of higher-order modes are excited

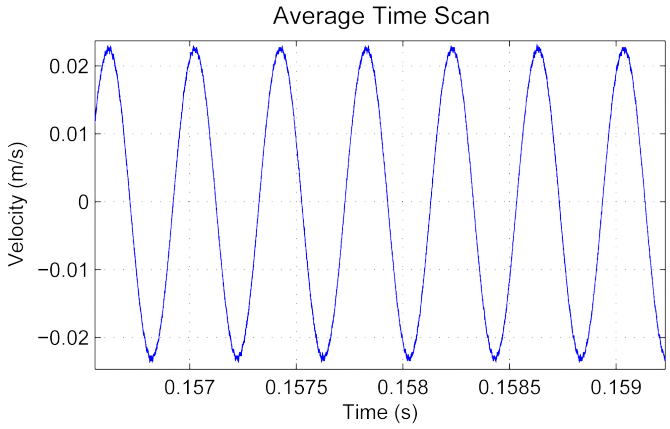

Figure 74: Plot of 5 ms of raw scan data with low current excitation.

and the velocity waveform changes shape. During analysis, the data in Figure 75 was heavily filtered to allow identification of the zero crossing point of the base frequencies. The crossing points were then combined with the raw data, which was averaged over 200 ms worth of samples to produce the curves shown in the figure. The filtered frequencies are assumed to arise from higher-order resonance of the spring hammer system, as well as resonances in the tether holding the device.

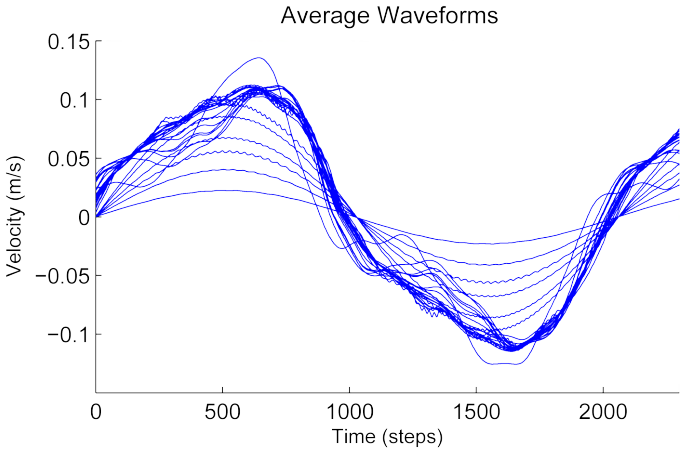

Figure 75: Waveform shape for hammer velocity from 1 to 12 A of excitation current in 0.5 A steps.

With the velocity data shown in Figure 75 and estimations of the swinging mass of the hammer and underlying gold plate, the kinetic energy of the system can be calcu-

lated based on the maximum velocity at each excitation. In addition, the maximum forward and backward velocities can also be calculated, providing insight into the amount of energy added to the system in each cycle. Figure 76 shows the calculated maximum kinetic energy of the system at different coil excitation currents. The energy level increases from 1 to 4 A at which point interactions between the two bodies begin to limit the travel of the hammer. Note that for most excitation levels above 3.5 A the negative kinetic energy (when the hammer is moving toward the stationary body and the magnetic forces are active) is higher than the positive kinetic energy, which is derived purely from the impact rebound velocity and the energy stored in the spring. This difference is energy that is being added to the system by the periodic magnetic field.

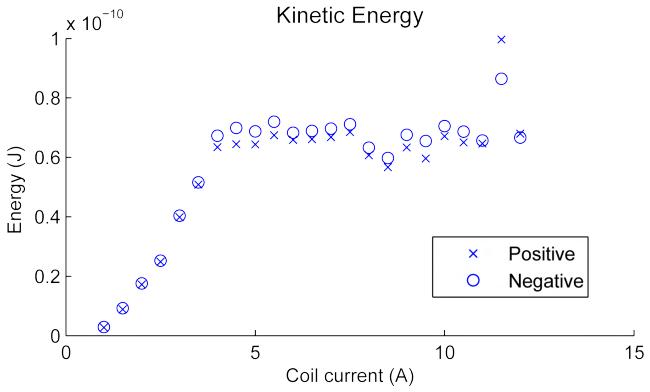

Figure 76: Kinetic energy of the swinging hammer.

Conservation of energy in oscillating systems enables calculation of the system spring constant if the deflection and kinetic energy are known. By numerically integrating the velocity to determine displacement, the spring constant can be calculated; the results are shown in Figure 77. The mean k value for excitation currents where impact does not disturb the oscillations (1 to 5.5 A)is is 2.6 N/m. Combining this with the estimated mass of the hammer gives an expected resonant frequency of 2,498 Hz compared with the actual measured excitation frequency of 2,484 Hz.

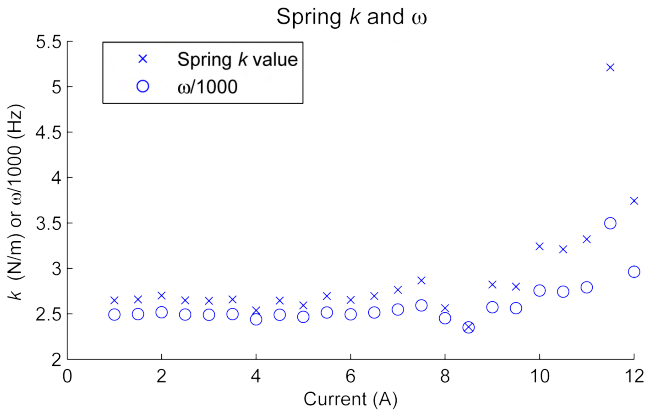

Figure 77: Spring constant (k) calculated from system energy and the resonant frequency assuming mass plotted over the range of excitation ranges.

6.2.7 Impact Analysis

In addition to the data already presented, high resolution time scans can also be used to detect and analyze the dynamics of impact between the bodies. Impact occurrences are recognizable as periods of rapid change in velocity over a very short time with a typical value of 0.5 m/s velocity change in a few μs, as shown in Figure 78. Impact occurrences were identified during analysis as a sequence of consecutive velocity measurements with the acceleration of more than 13,000 m/s^2. Local minima and maxima were identified on both ends of the impact occurrence to accurately calculate the velocity changes and impact time period. Impact occurrences were only found for excitation currents higher than 5 A–not at 4 A excitation as suggested by Figure 76. Visual searches of 4 and 4.5 A data did not reveal any of the characteristic areas of steep slope associated with impact. It is suspected that interactions of some sort are occurring at 4 and 4.5 A excitation but perhaps due to the lower system energy the impact or interactions do not behave as shown in Figure 78.

Figure 79 shows a 200 ms scan with a 12 A excitation current with the identified impacts in red and green, and false positives based only on slope in black. Notice how the raw signal in Figure 79 differs from that shown in Figure 74 with lower excitation current and no impact. The effects of higher-order signals and harmonics that were seen in Figure 75 are clearly visible in the scan.

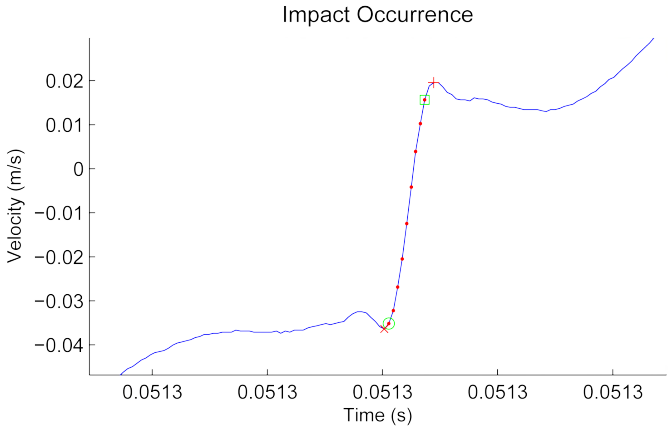

Figure 78: Plot of an impact occurrence. Red dots indicate points of high slope with green circles indicating the limits. Red crosses and x's mark the limits of impact used for energy calculations.

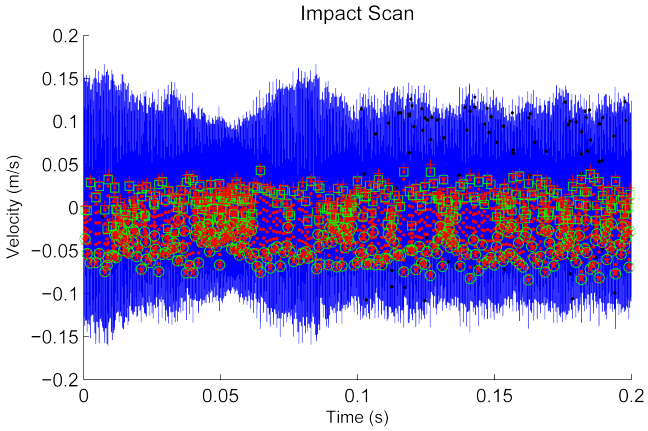

Figure 79: Plot of high-resolution scan showing impact occurrences. Red dots indicate points of high slope with green circles indicating the limits. Red crosses and x's mark the limits of impact used for energy calculations. Black dots indicate areas of high acceleration that were not from impact and were excluded.

With the initial and final velocities, impact duration and mass of the swinging hammer, an average impact force can be calculated from the change in momentum.

$$\bar{F} = \frac{d\rho}{dt} \tag{28}$$

The average impact force is plotted in Figure 80 with the standard deviation and the

maximum measured value. The distribution of impact in both time and energy varies due to higher harmonics and system fluctuation. This force can be compared with the FEM-based magnetic excitation forces, as shown in Figure 32, with a maximum magnetic force of 10 μN at 5 mT field compared with 160 μN of impact force. The energy added to the system is effectively stored in the system until it is released during impact, causing at least a 16 fold increase in instantaneous force.

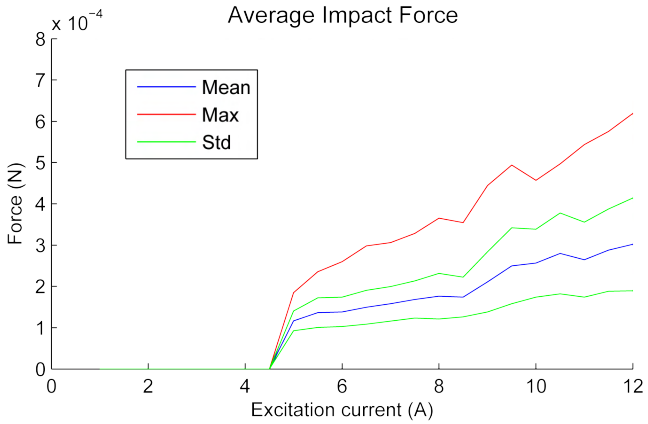

Figure 80: Plot of average impact forces based on changing momentum calculations.

Further analysis reveals that, depending on the intended use of the actuator, different excitation levels may be advantageous. In situations where maximum force is needed, it would be useful to operate at high currents, as shown in Figure 80. If a lower but more frequent impact force is required, operating at lower excitation currents would be beneficial. This is shown in Figure 81, where the increased frequency of impacts with 8 A excitation compensates for the lower average impact force as 8 A excitation generates nearly the same total force as 12 A excitation.

In addition to investigating the impact force, the energy lost in the impact occurrence can also be examined by comparing the initial and final hammer velocities. Figure 82 shows the average kinetic energy of the hammer immediately before impact and the energy lost during impact, which was calculated by subtracting the final velocity. Since the exiting energy is typically quite small, most of the available energy was lost during impact and the coefficient of restitution c_r for this setup is quite small. This is to be expected given the design of the experimental setup. The "stationary"

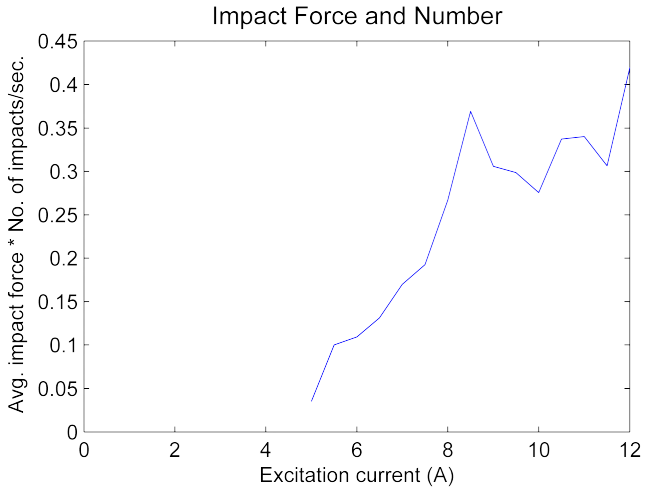

Figure 81: Plot of average impact force times impact frequency. The available force plateaus at 8 A of excitation current.

nickel body is actually suspended in space by a long gold tether to facilitate cutting the robot loose with a razor blade before use. The stationary body forms a spring mass system with the tether and absorbs a large amount of the impact energy. Vibrometer measurements of the motion of the stationary body showed that the body exhibited maximum velocities in the range of 10 to 20 $\mu m/s$ during moderate to large excitations. For this reason no estimations of c_r are made.

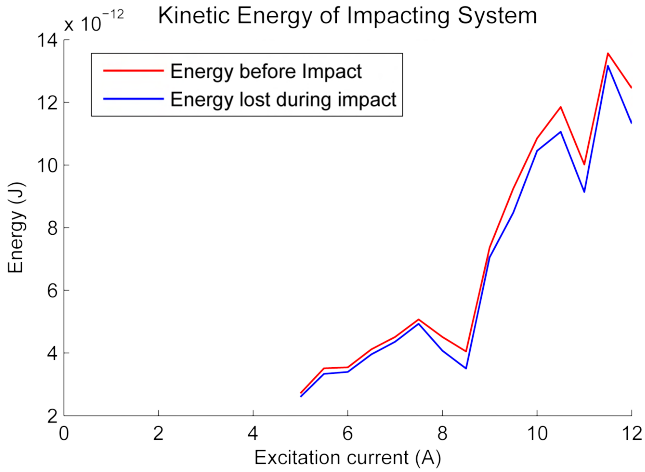

Figure 82: Plot of kinetic energy before impact and kinetic energy lost during impact.

System power can also be calculated based on the initial impact velocity and is shown in Figure 83.

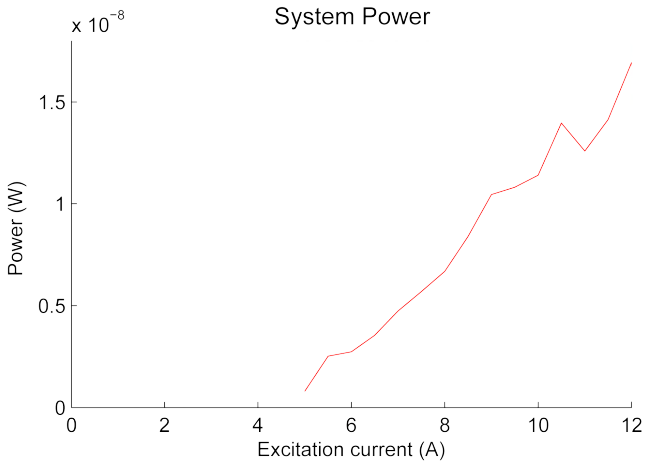

Figure 83: System power calculated from pre-impact velocity.

6.2.8 Pulse Analysis

The last method of vibrometer analysis performed on the actuator is pulse scanning. During the experiment, the actuator is excited with a series of short pulses which revels both the energy absorption and oscillation decay rates. In this example, the excitation current was increased in 0.5 A steps from 1 to 10 A. Scan resolution was typically not as high as the raw data scans due to the need for much longer scan times. Analysis of this data is typically performed on the envelope of the signal and doesn't require high time resolution.

Figure 84 shows the actuator response to a train of excitation pulses. Pulses and pauses of 200 ms each were found to be adequate for the system to reach a steady state. To help ensure repeatable readings, steady state amplitude values were taken from the later part of the pulse after typical transient behavior had died away. The single pulse shown in Figure 85 clearly shows the beginning of the pulse with the steep increase in oscillations followed by the exponential oscillation decay when excitation stops.

While the decay rate remains approximately constant for all pulses, the growth rate of

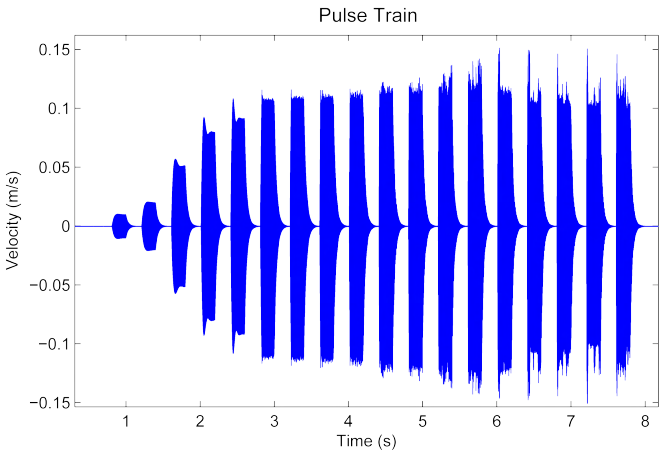

Figure 84: Train of 18 excitation pulses with increasing excitation currents starting at 1 A and ending at 10 A.

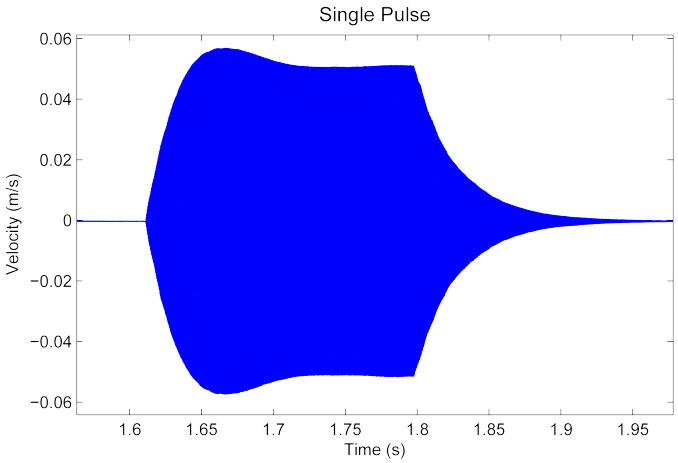

Figure 85: Single excitation pulse with 200 ms excitation period followed by 200 ms decay time before next pulse.

the pulse and steady state value depend strongly on the magnitude of the excitation. The average γ (as described in Figure 33 and Equation 18) was calculated to be 35.24 with a standard deviation of 2.5 for the entire pulse train.

6.2.9 Determining System Parameters

Using Equation 21, the resonant frequency of 2,484 Hz, and a γ of 35.24, the Q value of this oscillator was calculated to be 221. This is assumed to be the more accurate method of measuring the Q due to the energy leakage effects on the FFT data presented earlier. A more precise knowledge of the system Q also allows the energy absorption rate for the system to be determined. The official definition of Q is $2pi$ times the energy stored in the actuator divided by the energy lost per cycle. This value of Q combined with steady state measurements of total energy makes it possible to determine how much energy was lost to damping; this value must be equal to the energy added by the driving field. Figure 86 shows the plot. This data is taken purely from damping and does not include the energy lost during impact that is shown in Figure 82. In this plot, the change in slope at a field strength of 2.45 mT implies that impact or body interactions begin in this region and thus the only useful data where total energy losses are accurately represented are for field strengths below that value.

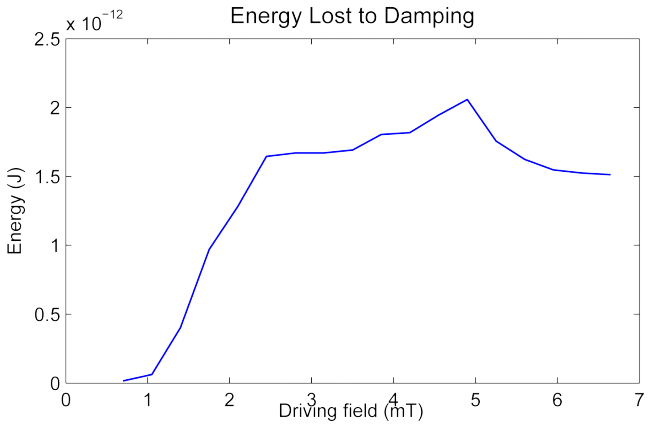

Figure 86: The amount of energy lost to damping and thus absorbed by the system in each cycle during steady state operation.

The data from Figures 86 and 82 can be combined to show the system's total energy loss and is shown in Figure 87 where the energy lost to impact has been averaged to find the energy loss per cycle due to impact. The combined damping and impact loss aligns quite nicely with the initial slope of the damping loss and suggests a relatively uniform energy absorption rate in the system. A linear fit of the system

shows that it absorbs energy at a rate of 9.2 $10^{-13} J/mT$ per cycle with a zero offset of -8 $10^{-13} J$.

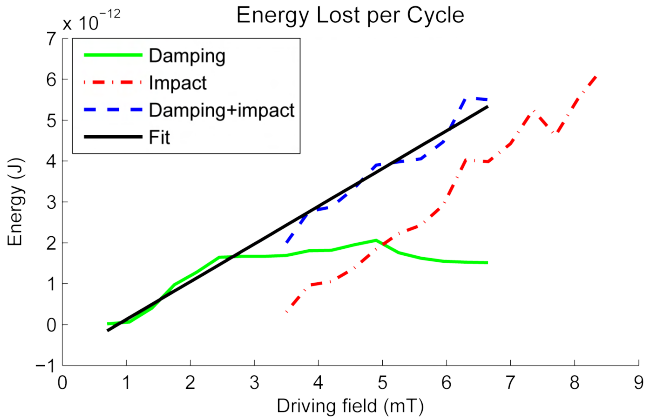

Figure 87: The amount of energy lost and absorbed to damping and impact in each cycle during steady state operation.

Figure 88 shows the energy lost and absorbed per second and is effectively the absorbed power. A linear fit of the data shows an absorption rate of 2.3 nW/mT with a zero offset of -2 nW by the WRMMA. When factoring in the size of the device, the power density of the WRMMA is 364 $W/m^3/mT$. While that damping and dissipation causes the total extractable system power to be less than the total absorbed power, it should be possible to design a system that converts a significant fraction of this energy to useful motion.

Another benefit of knowing γ is that the linear damping term (c) can be determined as described in Equation 16. Based on a calculated swinging body mass of 1.08 $10^{-8} kg$, c is calculated to have a value of 7.34 10^{-7}. Equation 17 will reveal k if ω_d is known from experiments. In this example, k is calculated to have a value of 2.63 N/m. In an ideal situation, m would be determined experimentally, but in this analysis it is based on fabrication geometry and thickness measurement.

Now that the physical parameters and an energy absorption has been determined, the attention can return to simulations to match simulated energy absorption to measured absorption, thereby better understanding the magnitude of the magnetic forces that drive the system. Figure 32 provides a modeled magnetic force, but as was shown in Figure 25, it is expected that interface geometry and body geometry

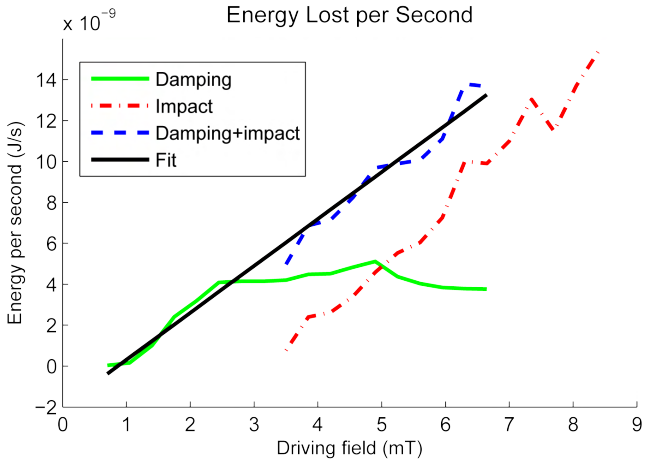

Figure 88: The amount of energy lost and absorbed to damping and impact per second during steady state operation – effectively, the absorbed power.

will significantly reduce the attractive forces. In addition, due to the swinging nature of the body, the gap is closed faster on one side than on the other, causing further reductions in magnetic force. To account for this in the simulation, the magnetic forces are multiplied by a scaling constant, as seen in Figure 35. The amount of energy absorbed by the system from the driving forces can be determined by calculating the amount of work the driving force has done on the system using the equation

$$W = Fd \tag{29}$$

where F is the force that acts on an object that moves d distance parallel to the direction of applied force. In the simulation this becomes a summation

$$W_{total} = \sum F * dx \tag{30}$$

over a period of a magnetic pulse. Figure 89 shows simulation energy absorption as a function of driving field with a magnetic-force scaling constant of 0.0715, plotted with the experimentally determined energy absorbed per cycle. In other words, the magnetic forces needed to inject the same amount of energy into the system as determined by experimental data are only about 7% of those shown in Figure 32. When excited with a 5 mT field, the impact forces generated by the actuator ($\sim$150 μN as

shown in Figure 80) are well over 200 times larger then the maximum zerogap force of 0.7 μN. The same calculation shows the impact forces at 8.4 mT to be over 150 times larger.

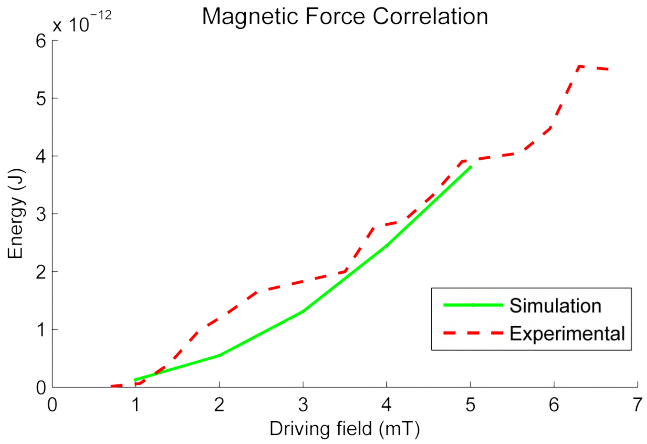

Figure 89: Simulated and measured energy absorption.

Several things are apparent from Figure 89. While the range of the simulated data is appropriate, the squared behavior does not match the more linear behavior of the experimental data. This is due to a number of factors. The squared behavior is expected, and can be explained by the $1/d^2$ dependence of the driving forces. But as was shown in the discussion about modeling magnetic forces (Figure 25), the sidewall angle prevents the bodies from approaching as close as one would expect and limits the small gap forces, thereby reducing the $1/d^2$ effect. Additionally, the modeled forces used in the simulation (Figure 32) assume that the bodies are well aligned when approaching each other. As discussed and shown in high-speed video capture (Figure 73), this assumption overestimates the magnetic forces for this device due to the swinging arm design. Lastly, once impact begins in the measured device ($\sim$3 mT), the interbody gap is closed and any increases in energy must come from the linear increase of the magnetic forces in response to increases in driving field. The simulation data here do not include impact, which began above a driving field of 5 mT; the actual device exhibited measurable impact at 3.5 mT and disruption of steady state energy levels above 2.1 mT. This is due to the rotation of the swinging body, as well as the variation of the interbody caused by fabrication variations. While

the simple model does not capture the complex behavior of the device, it does provide insight into its operation and the magnitude of the magnetic forces that drive it.

6.3 Frictional Force Measurement

Force measurement investigations were also made to measure behavior of the Magmite robot. Frictional forces between the Magmite robot and the playing field, and humidity effects were measured in a specialized setup. Attempts were also made at measuring static friction, impact forces and pushing forces but no satisfactory results were obtained. General trends and qualitative behaviors are clearly evident in the data, but quantitative certainty should not be assumed from the data. Attempts were made to compensate for signal noise levels, light sensitivity, and short-term sensor drift. Of increasing concern was large variability in the measured frictional forces, off-angle forces, probe-substrate interactions and long-term sensor calibration drift.

6.3.1 Experimental Setup

The experimental setup for force-sensing measurements consisted of a specially constructed field, package and field holder with an opening on one side, and is shown in Figure 90. A Femtotools force sensor (shown in Figure 91) mounted on a Sutter micropositioner was inserted into the side of the enclosure to probe the microrobot on the field. The field was connected to the HV amplifier and the entire setup was mounted in the environmental box with the standard coil setup. The force sensor outputs a 2.5 V signal with zero force and has a sensitivity of 131 $\mu N/V$ in both the positive and negative directions. The sensor has a bandwidth of 10,000 Hz but due to noise the signal had to be extensively filtered. The length of the sensor probe was extended by approximately 5 mm with small piece of optical fiber. The Sutter control and data collection was conducted in LabVIEW with subsequent analysis in MATLAB. The micropositioner is a stepper motor-driven XYZ stage with reported 40 nm minimum step sizes. It is equipped with a serial interface and can easily be programmed and controlled with LabVIEW. Measurements were made with Sutter velocities of either 1 or 10 $\mu m/s$. Higher velocities typically produced slightly lower frictional forces but differences were well within typical measurement variations.

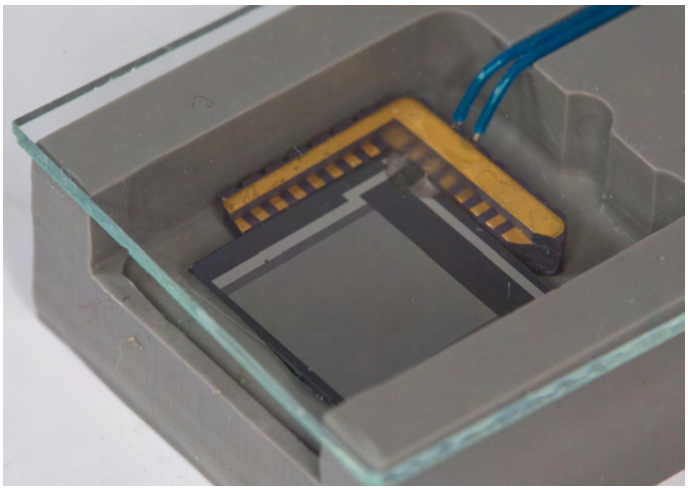

Figure 90: Setup for measuring frictional forces and humidity effects.

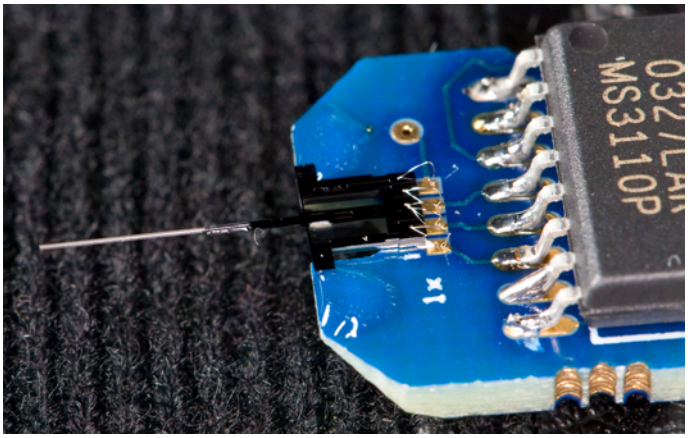

Figure 91: Femtotools MEMS-based microforce sensor with fiber extension.

Initial goals of trying to measure Magmite pushing or impact force were unsuccessful for several reasons. Given an average impact force of 160 μN over a period of 2.5 μs, the force must be averaged over a sample period of 100 μs. This gives a force of approximately 4 μN or 30 mV. A spike of such magnitude over one sample period was not visible in a system with a noise level of nearly 100 mV. Secondly, while the magnetic field had very little effect on the sensor output, the electrostatic clamping field had a very large effect on the sensor reading. This was minimized by extending the probe of the sensor, as shown in Figure 91, but even with the increased

standoff, noise from the electrostatic clamping signal was still quite evident and no experiments with dynamic clamping signals were attempted. Thirdly, fine control of the fast moving robot is extremely difficult under manual control and must be accomplished by a fast computerized servoing system. Efforts to manually drive the front of the robot head-on into the tip of the fiber were met with extremely low success rates.

Attempts at measuring static friction were also met with limited success. It was possible to measure dynamic frictional forces by long-term averaging and filtering of the data, but no traces of force spikes indicating static friction could be found in the data. There are a variety of possible explanations for this. The velocity and stepwise operation of the micropositioner, combined with the stiff spring constant of the force sensor, may have broken the static friction fast enough that the force sensor was not able to capture it. Additionally, the relatively large mass of the sensor body compared with the Magmite and frictional forces may have broken the static frictional forces with inertial forces before the sensor could register them, or quite simply, they may have been lost in the noise.

The friction forces of the sliding Magmite increase with the applied voltage squared, as shown in Figure 92. This is expected as the electrostatic forces as given in Equation 31 and depends directly on V^2.

$$F = \frac{\varepsilon_o A V^2}{2d^2} \tag{31}$$

Where ε_o A and d are the permittivity of free space, the area of the capacitor plates and the distance between them. Assuming that the robot body and interdigitated electrodes are roughly like two capacitors in series, circuit analysis shows that the potential between the robot body and any electrode line is approximately half of the voltage applied to the electrodes [15].

$$V_{robot} = \frac{V_1 C_1 + V_2 C_2}{C_1 + C_2} \tag{32}$$

Additional measurements were made after flooding the chamber with humid air. During experiments, air was bubbled through warm water before injecting it into the environmental box containing the experimental setup. The humidity was increased, then the flow was stopped and a fan inside the box circulated the air for 20 minutes to

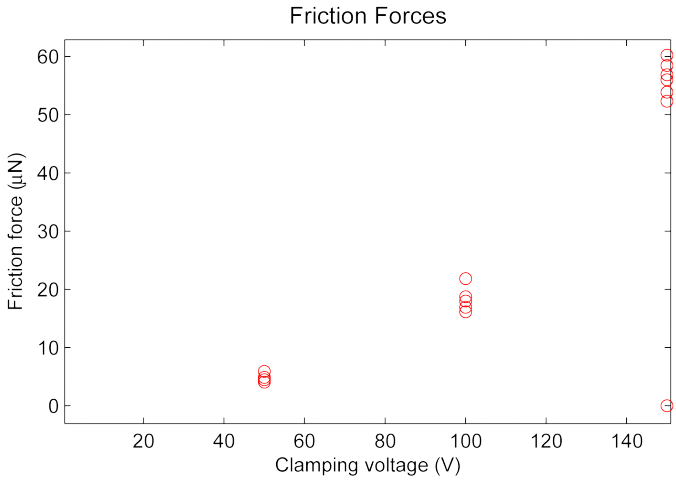

Figure 92: Frictional forces increase with clamping voltages. The outlying data point at 0 μN and 150V is to check for sensor drift.

allow the humidity to settle to a steady state value. While this helped ensure uniform humidity in the chamber, it also introduced long periods of time between measurement and increased variability in the measurements. Figure 93 shows the resulting data. Increases in humidity produced a two- to four-fold increase in frictional forces but the scattered values made it difficult to draw any conclusive results.

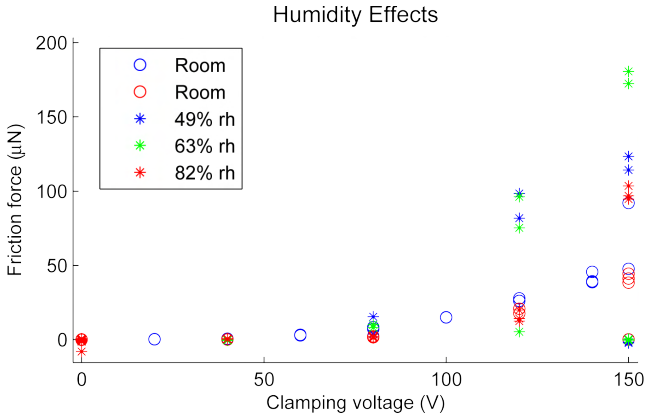

Figure 93: Increased chamber humidity from the standard 25 to 30% leads to large increases in frictional forces, varying from two and four times more than typical measurements. The outlying data point at 0 μN and 150V is a check for sensor drift.

Force measurements highlight the most challenging aspect of the operation of the Magmite robots. The accurate and reliable characterization of frictional forces in microsystems is extremely difficult due to large variations in measured results. When contact areas begin to approach the length scale of asperity size and spacing, that the effects of individual microscopic asperities become extremely important.

6.4 Magmite Driving Results

Results presented in this section are a combination of qualitative observations from robot operation and preliminary measurement indicative of general behavior. Due to the stochastic nature of the frictional forces and robot behavior, a large number of well-controlled experiments are needed to draw any authoritative conclusions. Software controls are not yet developed to allow such in-depth and repetitive testing. The data shown here is preliminary and representative of a "well behaved" robot driving under optimal conditions.

Three general modes of operation were observed that would make the robot move in a controllable manner where it could be commanded to move, stop and turn. In the first mode, robots were often observed to operate reliably without clamping. In most situations, the robot was observed to move backwards from the intended direction (it moved in the direction of the swinging hammer) and thus when it contacted a wall or object, oscillations and the robot would stop. An adequate explanation for this has not yet been developed and is the subject of continued investigation and simulation.

In the second mode, the inertial forces of the swinging hammer were strong enough to overcome frictional forces while driving with field strengths that did not cause impact in vibrometer experiments. The robot would move forward and backward with clamping. The robot is drivable and controllable but does not generate enough force to manipulate objects.

The third mode occurred when excitation signals drove the actuator to impact, moving the robot forward and backward with clamping. In this mode, the actuator generates enough force to push the 150×20 μm gold disks used in the third task of competition.

Output from the visual tracking module in the control software forms the basis

of the driving data. By combining this with the log of the signal parameters sent to the drive computer, the system response can be determined. Efforts are underway to automate the experiments by implementing servo control with parameter stepping. The tracking algorithm reported the X and Y location and the pose of the robot in each video frame, along with the local time stamp. This allowed for comparison between intended and actual direction in addition to detection of sideways motion. One result of the asymmetric design shown in Figure 43(a) is that the robot has a tendency rotate slightly in the field and crab-walk in the intended direction of travel while at a 20° to 25° angle. This produced large sideways motions in the tracker because of the difference in robot body and travel angle. Another point of interest is that while under manual control, the robot needed to be operated slowly to allow the operator to react before it left the field of view and electrode field. Combined with a 30 Hz tracking frequency and a large field of view, typical displacements between video frames were in the low single pixels, leading to significant noise and digitization in the data.

Figure 94 shows typical tracking data with the black dots representing the center of mass and the lines representing the pose of the robot. This is a short path with relatively few sections of straight uniform travel from which reliable tracking data can be extracted. The best results were found by driving the robot back and forth across the field of view and changing parameters while turning.

Typical velocity data is shown in Figure 95 with digitization readily apparent in the raw data. During analysis, individual patches of data between parameter changes are manually inspected and chosen to exclude areas where the robot sticks or exhibits jerky motion and rapid changes in speed. This data can then be correlated to the changing parameters, which in this case was frequency, as shown in Figure 96. The data clearly shows that the sharp response to excitation frequency exhibited in the vibrometer is not present in the driving data. Figure 96 is representative of typical data where velocity gradually peaks and falls off as the excitation frequency is swept across the natural resonance peak.

Investigation into the Magmite's response to driving frequency demonstrated the hysteresis-based effect shown in Figure 97. Once the robot began to move, the driving frequency could be adjusted up or down at will with small changes in velocity. At some

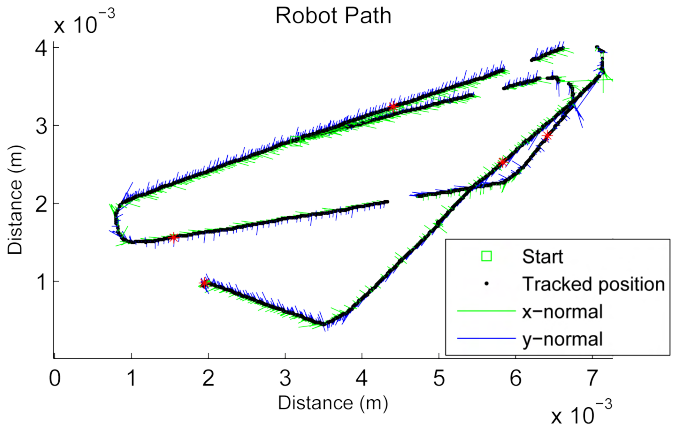

Figure 94: Example of tracking module output showing pose and position of the tracked robot. Blank spots in the data are places where the tracker lost the robot and needed to be manually reset during tracking. Red stars on the path represent uniform time increments to help correlate tracking and video data.

point far enough away from resonance, the robot would stick and further adjustments could not provoke its movement again until the drive frequency was brought back to resonance. Increasing the driving field strength had the effect of increasing robot speed over all frequencies, increasing the width of the frequencies over which the robot would operate by widening the response, and increasing the width of the central feature where the robot would break free and begin to move again. At sufficiently high excitation, the regions of no motion become little loops on the ends of a broad response curve.

The cause of the wide velocity response has not been determined. It is suspected that the swinging motion of the arm plays a roll as it generates a torque on the frame and causes the robot to twist. As mentioned before, efforts are underway to implement servoing and path following in the control software, which should increase the reliability and speed up the collection of data. It is suspected that while the clamping forces increase friction for a period of time, they are not enough to stop motion and clamp the robot frame to the substrate.

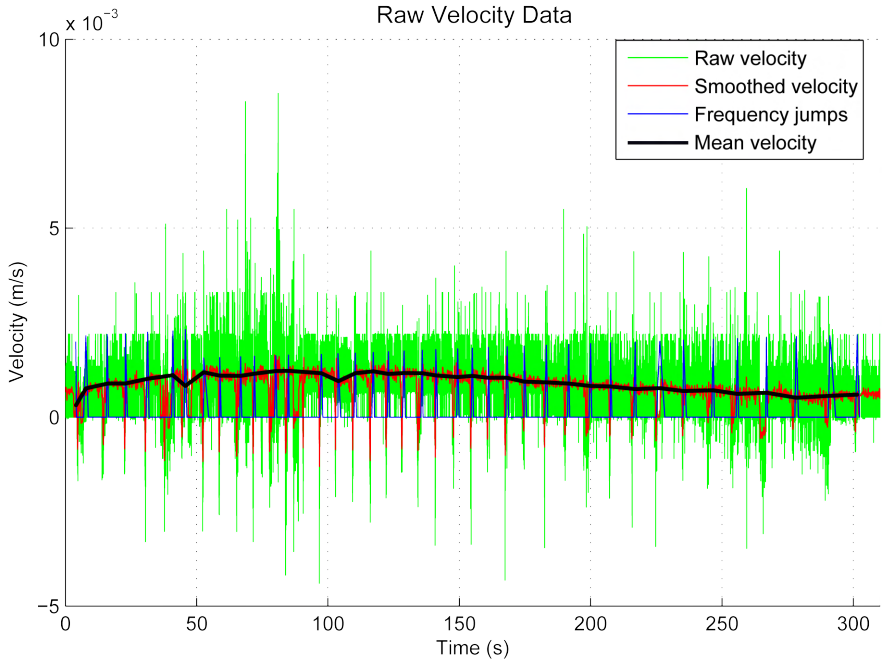

Figure 95: Typical velocity data showing velocity as a function of run time. This scan lasted over 5 minutes. Raw data is represented in green, and digitization and noise are clearly visible. The red trace represents averaged data and the blue spikes represent changes in driving conditions. The black line represents the mean velocity.

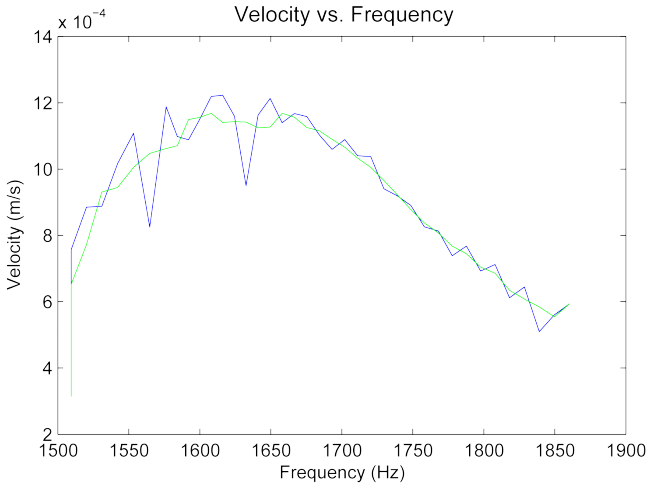

Figure 96: Velocity data that has been correlated to the frequency data of the log file. The green line is a moving average.

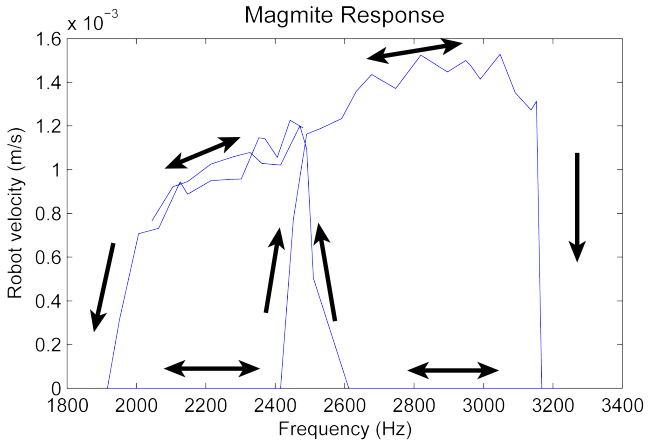

Figure 97: Hysteresis in the driving response. Once activated, the robot can be driven with a wide range of frequencies. At some point, the robot stops moving and sticks to the substrate. The frequency must then be brought back to the robot resonance to break it free again. The resonance of this robot was slightly less than 2,500 Hz.

7 Discussion and Conclusions

The field of microrobotics is developing rapidly with increased interest in biomedical microrobotic systems. Recent trends in medical care have seen the surgical community embracing medical robotic systems as effective and efficient tools. These tools allow surgeons to perform existing procedures with greater accuracy than was previously possible and enable new ones that benefit patient outcome, often by reducing surgical trauma. One important aspect of the robotic systems is that the end effectors are much smaller and often steadier than a surgeon's hand. They can access large portions of the body through small holes, coordinate motion between end-effectors and compensate for rhythmic body motion. As current and new systems shrink, they offer new possibilities such as those offered by GI tract camera pills. As systems continue to miniaturize, even more procedures will be possible. Microrobotics has the potential to have a major impact on the field of medicine. Mobile wireless microrobots will travel through naturally occurring passages in the body to deliver drugs, perform procedures or take measurements that today are only figments of our imaginations. But before this happens a lot of work must be done to develop the basic building blocks to build effective microrobots.

Unless they are to rely on the stochastic distribution of a large number of devices (which is the case with current drug therapy and much more realistic when considering nanosized systems) they will need some sort of propulsion mechanism. They will also need sensors, drug storage and release mechanisms, localization methods and actuators to power onboard mechanical systems. These are not trivial problems with silver-bullet solutions. They will take significant time and resources to develop solutions. One of the complicating factors is the complexity of microfabrication inherent in building the microrobots. Nonetheless, these are all interesting challenges and researchers around the world are working on a variety of solutions. Several groups are actively working on propulsion mechanisms for microrobotic systems as summarized in Chapter 2, while others are working in parallel on sensing modalities and sensors for microrobots. Drug delivery is an active topic of research in bioMEMS and can leverage developments from the area of drug-emitting polymers and drug-coated magnetically guided magnetic particles. Localization of microrobots in the body is an

important and difficult topic because of the device size and required accuracy. The limitations of current in-body localization techniques also complicate the issue. X-ray exposure to both patients and physicians is a problem with fluoroscopy, while current MRI machines have a typical voxel resolution of about 1 mm^3 and it is not clear how magnetic propulsion can be adapted to operate concurrent with imaging. These limitations have steered the efforts at IRIS in the direction of ocular applications where localization by video is possible.

This leaves the subject of actuators. The basic nature of these dictates that they transform energy from one form to another. They must by definition exert forces over a distance (ie, do work) to effect changes in their surroundings. MEMS designers often find it difficult to design microactuators with sufficient force and throw to do useful work, much less design them to operate without wires. It is no surprise that some of the most successful commercial microactuator systems are digital projection systems, which take very little force to move a mirror that changes the trajectory of a photon. It must also be asked whether mechanical actuators are necessary on medical microrobots. What role will active mechanical systems have in the medical field at size scales approaching the cellular level? It is not yet clear what purpose they will play or what new procedures they could enable; however, it is the author's belief that while such procedures could be developed in the future, they most certainly will not be if there are no suitable actuators available.

The wireless resonant magnetic microactuator is an actuator that can be used in any system that can rectify resonant motion. The Magmite is only one of many possible applications that necessitated its own special requirements. Operation and control of WRMMAs can be greatly simplified in other situations. Attaching the magnetic bodies to a fixed substrate would allow them to be driven with non-uniform magnetic fields. Better understanding of the actuator performance and response in future generations can greatly simplify the driving electronics. Well-defined frequency and current requirements would allow the use of simpler linear amplifier circuits rather than the more complex but flexible PWM system developed here to drive the Magmite.

Most actuators (and sensors) are designed to operate far from resonance in an effort to ensure repeatable and linear responses across their entire bandwidths. In this

case, resonant response is a valuable part of the actuator that allows for maximum power absorption and enables individual addressing of multiple actuators with one power signal. Depending on the application, this may necessitate some sort of feedback loop or hard stops to control or limit the actuator. In the case of the Magmite application, visual servoing was used to provide feedback.

7.1 Summary and Contributions

The focus of this dissertation is the development and analysis of a new wireless actuator powered by interbody magnetic forces. The actuators utilize the interbody forces to drive a resonant body to impact, which generates significantly higher instantaneous forces. In addition to high forces, the resonant nature of the actuators makes it possible to control multiple devices with one frequency-modulated driving field. The contributions of this thesis can be summarized as:

- FEM models of interbody forces were compared to experimental measurements and it was found that variations in geometry due to fabrication significantly reduced measured results. Special experiments confirmed that eliminating the geometry effects resulted in forces that closely matched expected results.

- A 1-D simulation was developed to predict actuator performance and determine the unknown interbody forces. When matched to experimental results, the simulation suggests that the interbody forces driving the asymmetric actuator are about 7% of those predicted by modeling, which did not account for geometrical variations and misalignments.

- Performance and response of the wireless actuator was measured in three types of laser-vibrometer-based experiments.

    1. FFT experiments gave the resonant response over a range of excitation frequencies and amplitudes.
    2. Analysis of the laser-vibrometer velocity data gave information on system energy and impact forces derived from analysis of momentum change during impact. Average impact forces of 300 μN were found with 12 A (8.4

mT), which are over 150 times larger than the maximum magnetic force suggested by simulation (at 8.4 mT). Comparison of pre- and post-impact velocities also gave the energy loss during impact.

3. Analysis of excitation pulses and resulting decay determined the damping coefficient. Combined with steady state behavior without impact, this revealed the energy absorption/loss rate. This rate was combined with the energy loss due to impact to determine system energy absorption per mT driving field to be 364 $W/m^3/mT$.

- As part of a team effort, the WRMMA was used to provide power and propulsion for the Magmite microrobot platform. In this application, it propelled the robot at speeds reaching 1.25 cm/s, which is over 40 body lengths per second and scales to over 400 miles per hour for a standard size car. The Magmite offers unparalleled control and performance in a sub-mm robotic platform. It is capable of driving forwards and backwards, turning left and right, and stopping on command. It was adapted as the platform of the competition based mechatronics lab class offered by the IRIS group at ETH Zurich. Through the hard work and efforts of the class advisors and students, the Magmite won the inaugural Nanogram competition at RoboCup 2007.

7.2 Future Work

Research on WRMMAs and the Magmite platform continues at IRIS with efforts to incorporate the wireless actuators into other microrobotic systems. The initial intention of the WRMMA as an on-board actuator on a microrobot platform has not yet been realized, partially because no suitable application has been identified. Achieving this goal will require shrinking the actuator and developing the proper fabrication or assembly process to integrate it with a larger robotic platform. Several potential hurdles must be overcome before this can be done. Firstly, the interaction of the magnetic actuator bodies and larger body of what is presumed to be a magnetically guided biomedical microrobot must be examined to ensure that the local magnetic field is sufficient to power the actuators and that local gradients do not impede its operation. Secondly, higher frequency driving electronics will need to be developed as

resonant frequency scales in proportion to l. The domain wall velocity for the magnetic material may also play a role and may influence the choice of materials or final minimum size. Barring any limitations from these two issues, it is conceivable that the actuator could be shrunk until the magnetic bodies are small enough to contain only a handful or even two magnetic domains, which are typically in the single μm range for common materials. While shrinking the actuators to such a size is highly speculative, investigations are underway to develop WRMMA-powered rotational actuators for externally controlled and powered uncoupling of modular GI-tract robots.

Magmite development is also continuing with rapid advances in new designs, environments of operation and servoed characterization. It has been shown that they can operate and manipulate objects on a flat surface in an aqueous environment. Preliminary results have also shown that it possible to individually control multiple devices at one time. Efforts are underway to develop effective control methods for actuation of multiple devices with a single magnetic field. Developments are needed to improve reliability and repeatability before swarms of robots can be controlled. To address this, research is currently directed at the use of a magnetic material with a lower coercivity and remanence, and reducing stiction between the Magmite and substrate through the use of surface coatings. One of the stated goals of the Nanogram competition is to improve the repeatability and reliability of microrobotics. While the Magmite showed itself to be much more reliable than the competition, it is still painfully unreliable for researchers unaccustomed to the behavior of microscale devices. Additionally, efforts are also underway to improve the simulation, and extend it to the stick-slip behavior of the Magmite. While it is difficult to accurately model the stochastic nature of friction at this scale, it is expected that simulations will shed light on the different operating modes of the devices and the parameters that influence them.

References

[1] J. Abbott, O. Ergeneman, M. Kummer, A. Hirt, and B. Nelson. Modeling magnetic torque and force for controlled manipulaiton of soft-magnetic bodies. *IEEE Transactions on Robotics*, 23(6):1247–1252, December 2007.

[2] J. Abbott, K. Peyer, L. Dong, and B. Nelson. How should microrobots swim. *International Sysmpsium of Robotics Research*, November 2007.

[3] T. Akiyama and K. Shono. Controlled stepwise motion in polysilicon microstructures. *Journal of Microelectromechanical Systems*, 2:106–110, September 1993.

[4] S. Baglio, S. Castorina, L. Fortuna, and N. Savilli. Modeling and design of novel photo-thermo-mechanical microactuators. *Sensors and Actuators A*, 101:185–193, 2002.

[5] E. W. Becker, W. Ehrfeld, E. Munchmeyer, H. Betz, A. H. adn S. Pongratz, W. Glashauser, H. J. Michel, and V. R. Siemens. Production of separation nozzle systems for uranium enrichment by combination of x-ray lithography and galvanoplastics. *Naturwissenschaften*, 69:520–523, 1982.

[6] D. J. Bell, S. Leutenegger, L. X. Dong, and B. J. Nelson. Flagella-like propulsion for microrobots using a magnetic nanocoil and rotating electromagnetic field. *Proc. of the 2007 IEEE Int. Conf. on Robotics and Automation (ICRA)*, April 2007.

[7] R. W. Brockett. On the rectification of vibratory motion. *Sensors and Actuators*, 20(1-2):91–96, November 1989.

[8] S. T. Chang, V. N. Paunov, D. N. Petsev, and O. D. Velev. Remotely powered self-propelling particles and micropumps based on miniature diodes. *Nature Materials*, 6:235–240, 2007.

[9] H. J. Cho and C. H. Ahn. A novel bi-directional magnetic microactuator using electroplated permanent magnetic arrays with vertical anisotropy. *13th IEEE*

International Conference on Micro Electro Mechanical Systems, pages 686–691, 2000.

[10] H. J. Cho and C. H. Ahn. Microscale resin-bonded permanent magnets for magnetic micro-electricalmechanical systems applicaitons. *Journal of Applied Physics*, 93(10):8674–8676, May 2003.

[11] A. E. Curtright and P. J. Bouwman. Power sources for nanotechnology. *International Journal of Nanotechnology*, 1(1/2):226–239, 2004.

[12] M. J. Daneman, N. C. Tien, O. Solgaard, A. P. Pisano, K. Y. Lau, and R. S. Muller. Linear microvibromotors for positioning optical components. *Journal of Microelectromechanical Systems*, 5(3):159–165, September 1996.

[13] P. Dario, R. Valleggi, M. C. Montesi, and M. Cocco. Microactuators for microrobots: A critical survey. *Journal of Micromechanics and Microengineering*, 2(3):141–157, September 1992.

[14] B. R. Donald, C. G. Levey, C. D. McGray, I. Paprotny, and D. Rus. An untethered, electrostatic, globally controllable MEMS micro-robot. *Journal of Microelectromechanical Systems*, 15(1):1–15, February 2006.

[15] B. R. Donald, C. G. Levey, C. D. McGray, D. Rus, and M. Sinclair. Power delivery and locomotion of untethered microactuators. *Journal of Microelectromechanical Systems*, 12(6):947–959, December 2006.

[16] B. M. Dutoit, P.-A. Besse, H. Blanchard, L. Guerin, and R. S. Popovic. High performance micromachined SM_2Co_17 polymer bonded magnets. *Sensors and Actuators A*, 77(3):178–182, November 1999.

[17] O. Ergeneman, G. Dogangil, M. Kummer, J. Abbott, M. Nazeeruddin, and B. Nelson. A magnetically controlled wireless optical oxygen sensor for intereocular measurments. *IEEE Sensors Journal*, 8(1):29–37, January 2008.

[18] O. Felfoul, S. Martel, G. Beaudoni, and J.-B. Mathieu. Micro-devices' susceptibility difference based MRI positioning system, a preliminary investigation.

26th Annual International Conference of the IEEE Engineering in Medicine and Biology Society, 2:1140–1143, September 2004.

[19] S. Floyd, C. Pawashe, and M. Sitti. An untethered magnetically actuated micro-robot capable of motion on arbitrary surfaces. *IEEE International Conference on Robotics and Automation*, pages 419–424, 2008.

[20] G. T. Gillies, R. C. Ritter, W. C. Broaddus, M. S. G. adn M. A Howard III, and R. G. McNeil. Magnetic manipulation instrumentation for medical physics research. *Review of Scientific Instruments*, 65(3):533–562, March 1994.

[21] S. Guan and B. Nelson. Magnetic composite electrodeposition of microarray magnets for MEMS actuators. *17th IEEE International Conference on Micro Electro Mechanical Systems*, 2004.

[22] S. Guan and B. J. Nelson. Magnetic composite electroplating for depositing micromagnets. *Journal of Microelectromechanical Systems*, 15(2):330–337, April 2006.

[23] P. Helin, M. Mita, and H. Fujita. Self aligned vertical mirrors and v-grooves applied to a self-latching matrix switch for optical networks. *13th IEEE International Conference on Micro Electro Mechanical Systems*, pages 467–472, 2000.

[24] S. Hollar, A. Flynn, C. Bellew, and K. S. J. Pister. Solar powered 10 *mg* silicon robot. *16th IEEE International Conference on Micro Electro Mechanical Systems*, pages 706–711, 2003.

[25] J. W. Judy and R. S. Muller. Magnetically actuated addressable microstructures. *Journal of Microelectromechanical Systems*, 6(3):249–256, September 1997.

[26] L. K. Lagorce and M. G. Allen. Magnetic and mechanical properties of micromachined strontium ferrite/polyimid composites. *Journal of Microelectromechanical Systems*, 6(4):307–312, December 1997.

[27] L. K. Lagorce, O. Brand, and M. G. Allen. Magnetic microactuators based on polymer magnets. *Journal of Microelectromechanical Systems*, 8(1):2–9, March 1999.

[28] A. Lee and A. P. Pisano. Polysilicon angular microvibromotors. *Journal of Microelectromechanical Systems*, 1(2):70–76, June 1992.

[29] A. Lee and A. P. Pisano. Repetitive impact testing of micromechanical structures. *Journal of Microelectromechanical Systems*, 39:73–82, 1993.

[30] R. J. Linderman and V. M. Bright. Nanometer precision positioning robots utilizing optimized scratch drive actuators. *Sensors and Actuators A*, 91:292–300, 2001.

[31] Y. T. Liu and T. Higuchi. Precision positioning device utilizing impact force of combined piezo-pneumatic actuator. *Transactions on Mechatronics*, 6(4):467–473, December 2001.

[32] Y. T. Liu and C. W. Wang. A self-moving precision positioning stage utilizing impact force of spring mounted piezoelectric actuator. *Sensors and Actuators A*, 102(1):83–92, December 2002.

[33] M. J. Madou. *Fundamentals of Microfabricaiton, The Science of Miniaturization*. CRC Press, 2nd edition, 2002.

[34] S. Martel, J.-B. Mathieu, O. Felfoul, H. Macicior, J. Beaudoin, G. Soulez, and L. Yahia. Adapting MRI systems to propel and guide microdevices in the human blood circulatory system. *26th Annual International Conference of the IEEE Engineering in Medicine and Biology Society*, 2:1044–1047, September 2004.

[35] T. Matsunaga, K. Kohdoh, M. Kumagae, and H. Kawata. Fabrication of a new electrostatic linear actuator. *Japanese Journal of Applied Physics*, 39(12B):7115–7119, December 2000.

[36] T. Mei, Y.Chen, G. Fu, and D. Kong. Wireless drive and control of a swimming microrobot. *IEEE International Conference on Robotics and Automation*, 2:1130–1136, May 2002.

[37] N. Miki and I. Shimoyama. Dynamics of a microflight mechanism with magnetic rotational wings in an alternating magnetic field. *Journal of Microelectromechanical Systems*, 11(5):584–591, October 2002.

[38] S. C. Montemagno and H. Neves. The art and science of engineering hybrid living/non-living mechanical devices. *15th IEEE International Conference on Micro Electro Mechanical Systems*, pages 1–5, 2002.

[39] NDT Education Resource Center. http://www.ndt-ed.org/EducationResources/CommunityCollege/MagParticle/Graphics/BHCurve.gif.

[40] M. Pai and N. C. Tien. Low voltage electrothermal vibromotor for silicon optical bench applications. *Sensors and Actuators A*, 83(1-3):237–243, May 2000.

[41] J. G. Pepin and H. T. Sawhill. Application of thick film technology to polymer bonded magnets. *Polymer Bonded Magnet Conference*, April 2002.

[42] A. P. Pisano. Resonant-structure micromotors: Historical perspective and analysis. *Sensors and Actuators*, 20(1-2):83–89, November 1989.

[43] M. Ruan, C. J, and C. B. Wheeler. Latching microelectromagnetic relays. *Journal of Microelectromechanical Systems*, 10(4):511–517, December 2001.

[44] K. Saitou, D. A. Wang, and J. J. W. S. Externally resonated linear microvibromotor for microassembly. *Journal of Microelectromechanical Systems*, 9(3):336–346, September 2000.

[45] M. Sendoh, K. Ishiyama, and K. I. Arai. Direction and individual control of magnetic micromachine. *IEEE Transactions on Magnetics*, 38(5):3356–3358, September 2002.

[46] O. J. Sul, M. R. Falvo, R. M. Taylor II, S. Wasburn, and R. Superfine. Thermally actuated untethered impact-driven locomotive microdevices. *Applied Physics Letters*, 89(20), November 2006.

[47] M. Tabib-Azar, B. Supapun, and M. E. Motamedi. A novel, highly scalable and very high-torque micromotor for MEMS and MOEMS applications using the mechanical rectification of oscillatory motion. *Proceedings of SPIE*, 3276:271–279, March 1998.

[48] B. Vikramaditya, B. J. Nelson, G. Yang, and E. Enikov. Microassembly of hybrid magnetic MEMS. *Journal of Micromechatronics*, 1(2):96–116, January 2001.

[49] K. Vollmers and J. P. R. Anderson, B. J. Nelson. High strength rare earth-iron-boron printed magnets used in a long throw high force electromagnetic actuator with microfabricate coils. *16th IEEE International Conference on Micro Electro Mechanical Systems*, 2003.

[50] B. Wagner and W. Benecke. Microfabricated actuator with moving permanent magnet. *IEEE International Conference on Micro Electro Mechanical Systems*, pages 27–32, 1991.

[51] H. H. Yang, N. V. Myung, J. Yee, D.-Y. Park, B.-Y. Yoo, M. Schrwatz, K. Noobe, and J. W. Judy. Ferromagnetic micromechanical magnetometer. *Sensors and Actuators A*, 97-98:88–97, 2002.

[52] T. Yasuda, I. Shimoyama, and H. Miura. Microrobot locomotion in a mechanical vibration field. *Advanced Robotics*, 9(2):165–176, 1995.

[53] K. B. Yesin, K. Vollmers, and B. Nelson. Modeling and control of unthered biomicrorobots in a fluidic environment using electromagnetic fields. *International Journal of Robotics Research*, 25(5-6):527–536, June 2006.

A Appendix A: RoboCup Nanogram

A.1 RoboCup Nanogram 2007

RoboCup is an international robotics competition designed to promote developments in artificial intelligence, robotics and related fields in a standardized environment where international teams of student engineers can tackle difficult robotics problems in a competition-based environment. As a nod to the international aspect of the endeavor and to foster wide-ranging interest and support, the original competitions were based on soccer, where teams of autonomous agents squared off in robotic soccer games. RoboCup started in the early 1990s with the goal of developing a team of fully autonomous humanoid robots capable of successfully competing against the human world champions by 2050. Continual evolution has lead to a variety of competitions, leagues, robot types and sizes, including robotic rescue, simulation leagues, and for the first time in 2007, a nanogram microrobot class.

A.1.1 Additional Fabrication Step Enabling Symmetric designs

As part of the 2007 class and conjunction with the advisory team, one of the student teams proposed a design change that utilized a second sacrificial copper layer between the gold and nickel layers. The additional sacrificial layer enables the nickel bodies to extend over the gold spring and frame without touching it. This eases the robot design constraints and was included as a trial design in the class fabrication run. The second sacrificial layer allowed for the design of symmetric robots, shown in Figure 98. The symmetry of the robots improved robot behavior and handling during driving and object manipulation. Figure 99 is an SEM image of a Magmite fabricated with the extra copper layer. Figure 100 is a picture of the Nanogram 2007 champions

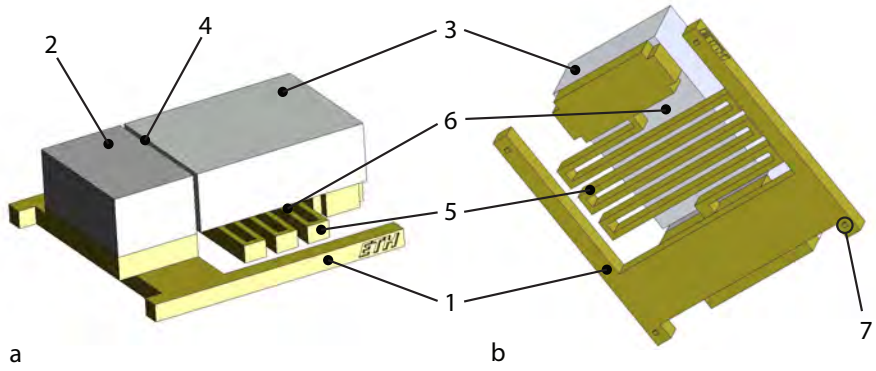

Figure 98: Symmetric Magmite design developed by 2007 RoboCup Nanogram competition winners.

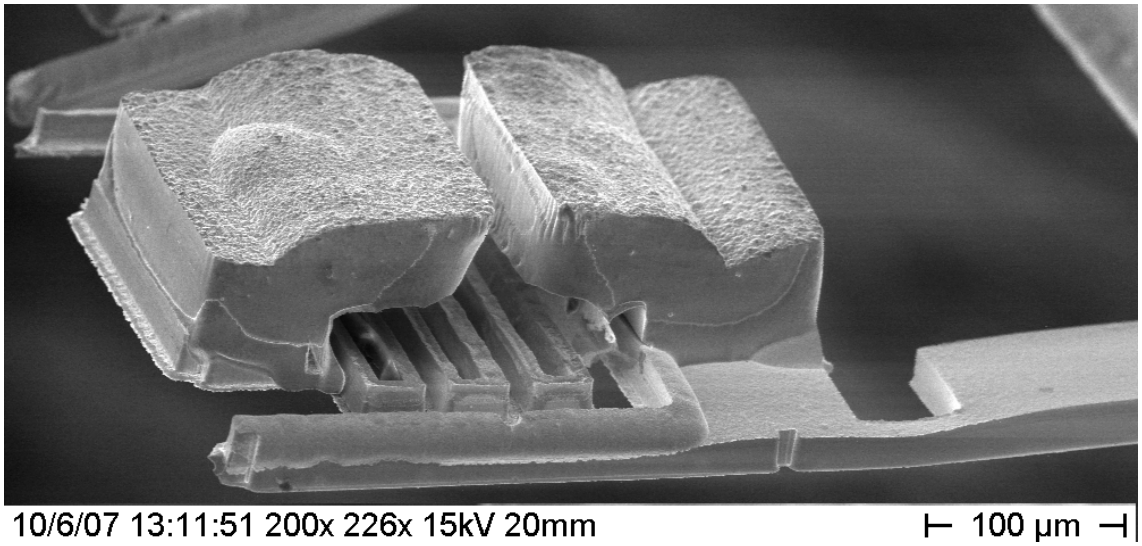

Figure 99: SEM of second generation Magmite with symmetric body configuration enabled by an additional process step.

Figure 100: The 2007 Nanogram Demonstration League winners.

B Appendix B: Magmite Fabrication Instructions

B.1 Magmite Fabrication

1. Clean wafers before starting process (use fresh test-grade dummy wafers, typically in multiples of three)
   (a) Clean with solvents
      i. Soak in acetone for 5 minutes with ultrasonic agitation
      ii. Soak in isopropyl alcohol (IPA) for 5 minutes with ultrasonic agitation
      iii. Rinse in quick dump rinser (QDR) until resistivity reaches 10 $MOhm$
   (b) Clean with piranha
      i. Submerge in hot piranha for 5 minutes (9:1 H_2So_4:H_2O_2)
      ii. Rinse into surface container or sink to remove acid
      iii. Rinse in QDR until resistivity reaches 10 $MOhm$
   (c) Dry wafers after above cleaning process with the spin rinser dryer (SRD)
   (d) Clean/etch wafers for 5 minutes in the plasma asher–maximum of three wafers at a time
2. Spin and pattern AZ 1813 photoresist to pattern the dimples for deep-trench (ICP) etching
   (a) Pre-bake wafer at 80°C on hotplate for 1 minute to dry wafer
   (b) Spin 1813 with program 7, or $\sim$1 μm thick
   (c) Soft bake at 110°C on hotplate for 2 minutes
   (d) Expose with 125 mJ/cm^2
   (e) Develop in 4:1 H_2O:351 developer for $\tilde{3}0$ seconds, relying on the appearance and disappearance of interference patterns in the exposed areas to judge when development is complete; develop 20% past time when last fringe field disappears
   (f) Place wafers in water in QDR immediately after development is finished

(g) Dry wafers in SRD

3. Etch dimple pattern in ICP or develop alternative to ICP etching using a different etch method, such as potassium hydroxide (KOH); etch 1.5 μm dimples in one standard etch cycle (two etch steps and one passivation step in first cycle)

4. Clean wafers after dimple etching; clean extra wafers to use as process dummies to accompany the actual devices wafers through the rest of the process

   (a) Clean with solvents

      i. Soak in acetone for 5 minutes with ultrasonic agitation

      ii. Soak in IPA for 5 minutes with ultrasonic agitation

      iii. Rinse in QDR until resistivity reaches 10 $MOhm$

   (b) Clean with piranha

      i. Submerge in hot piranha for 5 minutes (9:1 H_2So_4:H_2O_2)

      ii. Rinse in surface container or sink to remove acid

      iii. Rinse in QDR until resistivity reaches 10 $MOhm$

   (c) Dry wafers after above cleaning process with the SRD

   (d) Clean/etch wafers for 5 minutes in the plasma asher–maximum of three wafers at a time

5. Deposit seed/adhesion metal layers on the wafers

   (a) Load electron beam (e-beam) evaporator with three wafers and Ti and Cu crucibles

   (b) Pump down to low 10^{-5} $mbar$ to enhance adhesion

   (c) Deposit 50 nm Ti and 500 nm Cu on wafers

6. Spin, pattern and develop 35 μm Futurrex negative resist (NR2 20,000P)

   (a) Pre-bake wafer at 80°C on hotplate for 1 minute to dry wafer

   (b) Spin PR at 3,200 rpm with 3,500 rpm/second acceleration for 10 seconds

(c) Bake at 150°C for 110 seconds

(d) Allow to cool for 5 minutes

(e) Align and expose the first copper layer on wafers with dimples; expose blank dummy wafers first to check process

(f) Expose 2,880 mJ/cm^2

(g) Post exposure bake at 80°C for 4 minutes

(h) Cool for 5 minutes

(i) Develop in RD6 (Futurrex brand developer) until large areas are clear; continue developing for ∼10 seconds; rinse and inspect; continue developing if needed

7. Plate copper standoffs to raise spring and swinging body off the substrate

(a) Perform Hall cell test on copper bath and make additions as needed (2 A for 5 minutes with brass test plate)

(b) Spray wafer with water pistol to dislodge all gas bubbles from crevices and corners

(c) Clean/etch wafer in 1:9 H_2So_4:H_20 to remove Cu oxide

(d) Rinse wafer and place in holder quickly without letting it dry

(e) Check continuity from holder leads to wafer surface; should be below 3 Ohm

(f) Plate wafer at 1 A for 270 seconds (voltage is usually $\sim$ 1 V); use pulse plating with 2 ms period, 1 ms on and 1 ms off (1 ms on/off)

(g) After plating first dummy wafer, strip PR with acetone and measure copper standoff island thickness; if acceptable (6 to 7 μm), continue other wafers

(h) Cover alignment marks on wafers with dimples using small pieces of yellow plating tape to prevent metal deposition over ICP etched alignment marks

8. Strip PR from all plated wafers with RR4 (Futurrex brand resist remover)

(a) Fill wafer container with RR4, place in ultrasonic bath and heat bath to 80°C

(b) Immerse wafers in container and agitate with ultrasound for 5 minutes

(c) Rinse wafers with IPA and place in QDR; rinse to prescribed limits, 10 $MOhm$

(d) Dry in SRD

9. Deposit 25 nm thick Ti layer over wafer with E-beam evaporator; this improves PR adhesion in the next step

   (a) Load wafers and Ti crucible in evaporator

   (b) Deposit 25 nm Ti

10. Spin, pattern and develop a 35 μm PR layer using NR2 20,000P photoresist

    (a) Pre-bake wafers at 80°C for 1 minute

    (b) Spin PR on at 3,200 rpm with 3,500 rpm/second acceleration for 10 seconds

    (c) Bake at 150°C for 110 seconds

    (d) Cool for 5 minutes

    (e) Align and expose the gold layer with 2,880 mJ/cm^2

    (f) Post exposure bake at 80°C for 4 minutes

    (g) Cool for 5 minutes

    (h) Develop with RD6 developer until bodies begin to open up

        i. Check results under microscope

        ii. If most of desired devices are not clear, continue developing for ∼20 to 30 seconds, and recheck

        iii. If most (50 to 70%) of desired devices are clear, stop developing and accept the others as losses; due to the nature of this PR process 5% of the devices will be destroyed because the arms defining the springs are over developed (underetched by the developer), 70 to 80% of the devices appear acceptable, and 15 to 25% of the devices have photoresist left in the springs

(i) Rinse wafers in QDR

(j) Dry wafers in SRD

11. Electroplate the gold layer

(a) Warm gold bath to 50°C and prepare power supply for 84 minutes at 0.03 A ($\sim$0.3 V if all is behaving correctly) with a 2 ms period, 1 ms on/off

(b) Spray wafers with water to dislodge bubbles

(c) Etch Ti from exposed Cu surface with Ti etch

i. Ti etch is made with 5 mL HF, 65 ml ammonium fluoride, water to make 500 mL; mixed, stored and used in plastic (PP or Teflon) containers

ii. Etch Ti until exposed areas are a clear copper color (etched Ti produces mottled look) and continue etching for 30 seconds (usually takes $\sim$4 minutes)

(d) Rinse wafers well

(e) Dry alignment marks with N_2 and cover with small pieces of yellow plating tape

(f) Wet wafer again with spray pistol

(g) Etch/clean wafer with 10% H_2So_4

(h) Rinse and place in Au plating holder

(i) Check continuity

(j) Place holder in plating bath and plate

(k) Strip PR with acetone and measure thickness; if acceptable (20 to 25 μm), continue with other wafers

12. Strip PR from all plated wafers with RR4

(a) Fill wafer container with RR4, place in ultrasonic bath and heat bath to 80°C

(b) Immerse wafers in container and agitate with ultrasound for 5 minutes

(c) Rinse wafers with IPA and place in QDR; rinse to prescribed limits, 10 $MOhm$

(d) Dry in SRD

13. Etch Ti from wafer surface with Ti etch

(a) Etch Ti until exposed areas are a clear copper color (etched Ti produces mottled look) and continue etching for 30 seconds

(b) Rinse wafer well before drying

14. Spin, pattern and develop 100 μm PR layer to define the second electroplated copper sacrificial layer using NR2 20,000P

(a) Pre-bake wafers at 80°C for 1 minute

(b) Spin PR at 1,500 rpm with 2,000 rpm/second acceleration for 10 seconds

(c) Bake at 70°C for 10X minutes

(d) Bake at 150°C for 200 seconds

(e) Cool for 5 minutes

(f) Align and expose the second copper layer with a dose of 10,800 mJ/cm^2

(g) Post exposure bake at 80°C for 9 minutes

(h) Cool for 5 minutes

(i) Develop with RD6 developer

i. This step is generally not developed fully, as some PR can remain between the spring arms; it is generally more important that the PR is not underetched too much or the copper layer may creep too far over the Au areas for the Ni to adhere well

ii. Develop until large areas are clear; rinse and inspect

A. PR between the spring arms fine, and tops of Au springs should be clear

B. PR should not be underetched severely

(j) Rinse wafers in QDR

(k) Dry wafers in SRD

15. Plate copper standoffs to raise the Ni bodies off the surface of the springs (Step added during the 2007 ARM class, see Appendix A)

    (a) Perform Hall cell test on copper bath and make additions as needed (2 A, 5 minutes with brass test plate)

    (b) Cover alignment marks on wafers with dimples using small pieces of yellow plating tape to prevent metal deposition over alignment marks

    (c) Spray wafer with water pistol to dislodge all gas bubbles from crevices and corners

    (d) Clean/etch wafer in 1:9 H_2So_4:H_20 to remove Cu oxide and and possible Au oxide

    (e) Rinse wafer and place in holder quickly without letting it dry

    (f) Check continuity from holder leads to wafer surface, (should be below 3 Ohm)

    (g) Plate wafer at 1 A, for 10 minutes (voltage is usually $\sim$1 V); use pulse plating, 2 ms period, 1/1 on/off

    (h) After plating first dummy wafer, strip PR with acetone and measure copper standoff island thickness; if acceptable (second Cu layer is typically $\sim$8 μm above the Au layer), continue other wafers

16. Strip PR from all plated wafers with RR4

    (a) Fill wafer container with RR4, place in ultrasonic bath and heat bath to 80°C

    (b) Immerse wafers in container and agitate with ultrasound for 5 minutes

    (c) Rinse wafers with IPA and place in QDR; rinse to prescribed limits, 10 $MOhm$

(d) Dry in SRD

17. Deposit 25 nm thick Ti layer over wafer with E-beam evaporator; this improves PR adhesion in the next step

    (a) Load wafers and Ti crucible in evaporator

    (b) Deposit 25 nm Ti

18. Spin, pattern and develop 100 μm PR layer to define Ni bodies using NR2 20,000P

    (a) Pre-bake wafers at 80°C for 1 minute

    (b) Spin PR at 1,500 rpm with 2,000 rpm/second acceleration for 10 seconds

    (c) Bake at 70°C for 10 minutes

    (d) Bake at 150°C for 200 seconds

    (e) Cool for 10 minutes

    (f) Align and expose the Ni layer with 10,800 mJ/cm^2

    (g) Post exposure bake at 80°C for 9 minutes

    (h) Cool for 10 minutes

    (i) Develop with RD6; this PR layer is intentionally underdeveloped to prevent the Ni bodies from growing together

        i. Develop until ∼1/2 the plating thief area around the wafer is clear

        ii. Check results under microscope

            A. The Ni body areas should be open in the middle but with visible resist left in the corners; destructive testing of the bar separating the two bodies (using a razor blade corner) should reveal that the bar is still firmly attached to the substrate between the two bodies

            B. Devices with different width/size bodies on the same wafer will generally not develop at the same time; check the desired devices and develop for them, ignoring the others

    (j) Rinse wafers in QDR

(k) Dry wafers in SRD

19. Plate the Ni bodies

(a) Check check that the bath pH is below 4.0; add Sulfamic acid as needed to reduce

(b) Warm the Ni bath to 50°C

(c) Prepare the power supply to plate at 0.75 A ($\sim$1.7 V) for 140 minutes with 2 ms period, 1 ms on/off

(d) Some of photoresist was not properly removed in the develop step due to the underdevelopment; this resist must be removed in this step OR covered (covering is suggested as the faster, easier solution with less risk to the devices)

i. Solvent removal

A. Fold a small cleanroom towel twice and wet the corner with acetone

B. Carefully place it over the PR deposit to be removed and drag it parallel to the nearest feature wall on the wafer and towards the edge of the wafer

C. Shift folded corner to another "clean" area of the towel and repeat until the Cu layer is clean and unstreaked, using many towels and perhaps small probes or flat screwdrivers to reach the corners; remember that small changes in surface area are offset by the large area of the plating thief

(e) Spray the wafers to remove all bubbles

(f) Etch titanium in exposed areas with Ti etch for 30 seconds longer than needed to produce clear copper color in the exposed areas

(g) Rinse well and dry the front surface

(h) Some of photoresist that was not properly removed in the develop step due to the underdevelopment should have been removed or covered in this step

i. Covering with conductive tape

A. Dry the surface of the wafer well

B. Using the conducting adhesive tape (available as copper shielding tape from electronic component vendors, single-side adhesive, 1 inch wide), cut strips long enough to span the wafer on all four sides of the area filled with devices

C. Wipe the Cu surface of the tape pieces with acetone

D. Peel off the paper backing and adhere the tape to the surface of the wafer, covering the undeveloped PR, restoring the plating thief to slightly larger than its original area when the seams between the four quadrants of the wafer are covered with tape

E. Using a sharp razor blade, trim off the tape hanging over the edge of the wafer

F. Trim the tape so that it does not have double thickness near the edge of the wafer where it is squeezed by the wafer holder; if making some of the pieces shorter, ensure that the ends are trapped under other pieces of tape; all exposed tape ends should be under other tape or squeezed under the wafer holder to prevent stress induced curling during plating

(i) Spray the wafer with water

(j) Clean/etch the wafer with tape in 10% H_2So_4 for 30 seconds

(k) Place the wafer in the Ni holder and check continuity

(l) Electroplate for the allotted time

(m) After plating, check that Ni plating did not grow over the top of the PR in the devices of interest; if so, decrease the plating time

(n) Remove the plating tape and strip the PR with acetone and check the thickness; thickness will vary over the wafer with both radial and asymmetric differences

(o) Adjust plating time for subsequent wafers if needed

(p) Using a razor blade, dig under the corner of the plating thief quadrants to

try to create a crack between the metal and the wafer; if possible, peel the quadrant of nickel off; this eases dicing of the wafer later

20. Strip PR from all plated wafers with RR4; PR can be removed with acetone but this has a tendency to leave PR pieces stuck in spring meanders
    (a) Fill wafer container with RR4, place in ultrasound bath and heat bath to 80°C
    (b) Immerse wafers in container and agitate with ultrasound for 5 minutes
    (c) Rinse wafers with IPA and place in QDR; rinse to prescribed limits, 10 $MOhm$
    (d) Dry in SRD
21. Scribe the wafers before releasing
    (a) Cover the back of the wafer with blue dicing tape
    (b) With the diamond scribe, scratch lines between and around all clumps of devices
    (c) Break off and dispose of the thief areas of the wafer while saving the device areas
22. Etch the sacrificial Cu layers using ammonium peroxidisulfate (ammonia persulfate) and ammonia
    (a) Mix 10 g ammonia persulfate in 100 ml H_20 and add 5 ml ammonia; the ammonia increases the reaction rate and protects the nickel from damage
    (b) Place a section of wafer in a shallow container and cover the mixture
    (c) After 1 to 2 hours, using a microscope–gently probe one end of a group of tethered devices to see if they are released; if not, wait
    (d) Start removing strings of devices with tweezers
        i. Grab the section of silicon with one set of reverse-action tweezers in one hand; be sure to apply sufficient downward force at all times to

prevent the tweezers from popping up and sweeping one tip across the silicon, destroying devices

ii. With a second, fine-tipped set of tweezers, slide a bar of tethered devices over the edge of the silicon where it can easily be grabbed

iii. Rinse well in DI water and place on a towel to dry before placing in storage containers to be used as needed

B.2 Playing Field Fabrication

1. Clean wafers before starting process (use oxide-covered test wafers in multiples of three)

   (a) Clean with solvents

      i. Soak in acetone for 5 minutes with ultrasonic agitation

      ii. Soak in IPA for 5 minutes with ultrasonic agitation

      iii. Rinse in QDR until resistivity reaches 10 $MOhm$

   (b) Clean with piranha

      i. Submerge in hot piranha for 5 minutes (9:1 H_2So_4:H_2O_2)

      ii. Rinse in surface container or sink to remove acid

      iii. Rinse in QDR until resistivity reaches 10 $MOhm$

   (c) Dry wafers with the SRD

   (d) Clean/etch wafers for 5 minutes in the plasma asher, loading a maximum of three wafers at a time

2. Deposit 300 nm of aluminum on the wafers using E-beam evaporation

   (a) Load wafers and aluminum crucible in evaporator and pump down to low 10^{-5} $mbar$

   (b) Deposit aluminum according to directions in evaporator manual

3. Spin and pattern AZ 1813 photoresist to pattern the field electrodes

   (a) Pre-bake wafer at 110°C on hotplate for 1 minute to dry wafer

(b) Spin 1813 with program 7 for res st layer $\sim$1 μm thick

(c) Soft bake at 110°C on hotplate for 2 minutes

(d) Expose with 125 mJ/cm^2

(e) Develop in 4:1 H_2O:351 developer for $\sim$30 seconds, relying on the appearance and disappearance of interference patterns in the exposed areas to judge when development is complete; develop $\sim$20% past the time when last fringe field disappears

(f) Place wafers in water in QDR immediately after development is finished; rinse all when finished

4. Etch aluminum (Al)with hot Al etch

(a) Use standard Al etch (commercial or self-made)

(b) Most Al etches work better at slightly elevated temperatures, warm Al etch in glass container in the heated ultrasonic bath to $\sim$50°C temperature

(c) Submerge wafer in solution,; etch an extra 10% after wafer is clear

(d) Place wafers in QDR after etch and rinse; photoresist can be removed here if desired, but wafers must be cleaned again after laser etching shorts

(e) Dry wafers in SRD

5. Remove shorts with lasermill or probe station

(a) Test continuity between electrodes

(b) Place wafer in laser mill with vacuum hold down

(c) Etch shorts between lines with low-power laser blasts; begin by testing parameters on unused pads on the far side of the wafer

(d) Test continuity; if resistance has increased significantly but continuity remains, small shorts may be burnt out with an electrical current (this will only take care of small shorts, not the large ones that you can see under the microscope)

i. Load wafer in the probe station

ii. Carefully make contact to the two main bonding pads with probes that are connected to a current-limited power supply (supply off); probes must penetrate the photoresist

iii. Turn power supply on with current limited at a low value, increasing both current and voltage limits until the short is burned out

iv. Sharp probes can also be used to physically scratch Al shorts between lines away.

6. Clean wafers

   (a) Clean with solvents

      i. Soak in acetone for 5 minutes with ultrasonic agitation

      ii. Soak in IPA for 5 minutes with ultrasonic agitation

      iii. Rinse in QDR until resistivity reaches 10 $MOhm$

   (b) Dry wafers with SRD

7. Use Plasma Enhanced Chemical Vapor Deposition (PECVD) to deposit 1 μm of silicon dioxide over the wafer (this must be done in the FIRST lab at Hoenggerberg)

8. Spin and pattern AZ 1813 photoresist to pattern the holes in the oxide to allow wirebonding to the aluminum; use the same mask as used to pattern the electrodes, but rotate it 180 degrees in the plane of the mask (keep the chrome side down) so the other half of the mask is over the fields on the wafer

   (a) Pre-bake wafer at 110°C on hotplate for 1 minute to dry wafer

   (b) Spin 1813 with program 7

   (c) Soft bake at 110°C on hotplate for 2 minutes

   (d) Expose with 125 mJ/cm^2

   (e) Develop in 4:1 H_2O:351 developer for ∼30 seconds, relying on the appearance and disappearance of interference patterns in the exposed areas to judge when development is complete; develop ∼20% past time when last fringe field disappears

(f) Place wafers in water in QDR immediately after development is finished; rinse all when finished

9. Etch the exposed oxide from the bonding pads with a plasma etching system

10. Strip the photoresist with RR4 PR stripper

    (a) Fill wafer container with RR4; place in ultrasonic bath and heat bath to 80°C

    (b) Immerse wafers in container and agitate with ultrasound for 5 minutes

    (c) Rinse wafers with IPA and place in QDR; Rinse to prescribed limits, 10 $MOhm$

    (d) Dry in SRD

11. If desired, field walls, mazes or other patterns can be applied to the field now with SU-8

    (a) Dry wafer on 95°C hotplate for 1 minute

    (b) Apply SU-8 2010, spread resist at 700 rpm (accelerate 500 rpm/second) for 1 second, then spin at 2,000 rpm (accelerate 300 rpm/second) for 30 seconds ($\sim$10 μm)

    (c) Bake at 95°C for 3 minutes

    (d) Expose with 600 mJ/cm^2

    (e) Post exposure bake at 95°C for 4 minutes

    (f) Develop with SU-8 developer

        i. Develop with developing solution in developing container

        ii. After developer begins to run off in smooth sheet with no ripples, transfer to rinse container

        iii. Rinse for a few seconds

        iv. Holding wafer over a solvent waste container with a small amount of clean IPA in the bottom, gently shake a drop of developer from the wafer into the IPA; if the drops of developer form a cloudy white

"ribbon" like precipitate in the IPA continue developing and repeat; dissolved SU-8 is not soluble in IPA, but the developer is, this leads to the formation of white precipitates if the developer is saturated with SU-8

v. After drops in IPA remain clear, rinse the wafer with IPA and place it in the QDR

vi. Rinse in QDR and dry in SRD

12. Scribe wafer to break out fields using the wafer scriber or dice wafer with saw

13. Glue fields in packages with super glue (fields can later be removed by soaking overnight in acetone)

14. Wirebond field pads to proper package pins ensuring that the tops of the bonding wires are below the top of the package

15. Using 5 *min* epoxy, carefully encase the wires to protect them